

AD-A161 425 HEAD-SPINE STRUCTURE MODELING: ENHANCEMENTS TO SECONDARY LOADING PATH MOD (U) NORTHWESTERN UNIV EVANSTON IL DEPT OF CIVIL ENGINEERING

HEAD-SPINE STRUCTURE MODELING: ENHANCEMENTS TO
SECONDARY LOADING PATH MOD (U) NORTHWESTERN UNIV
EVANSTON IL DEPT OF CIVIL ENGINEERING
T BELYTSCHKO ET AL JUL 85 AAMRL-TR-85-019 F/G 6.

1/2

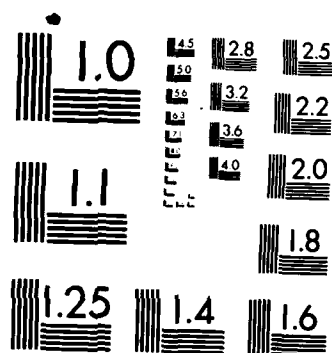
UNCLASSIFIED

T BELVTSCHKO ET AL

JUL 85 AAMRL-TR-85-019

F/G 6/19

NL



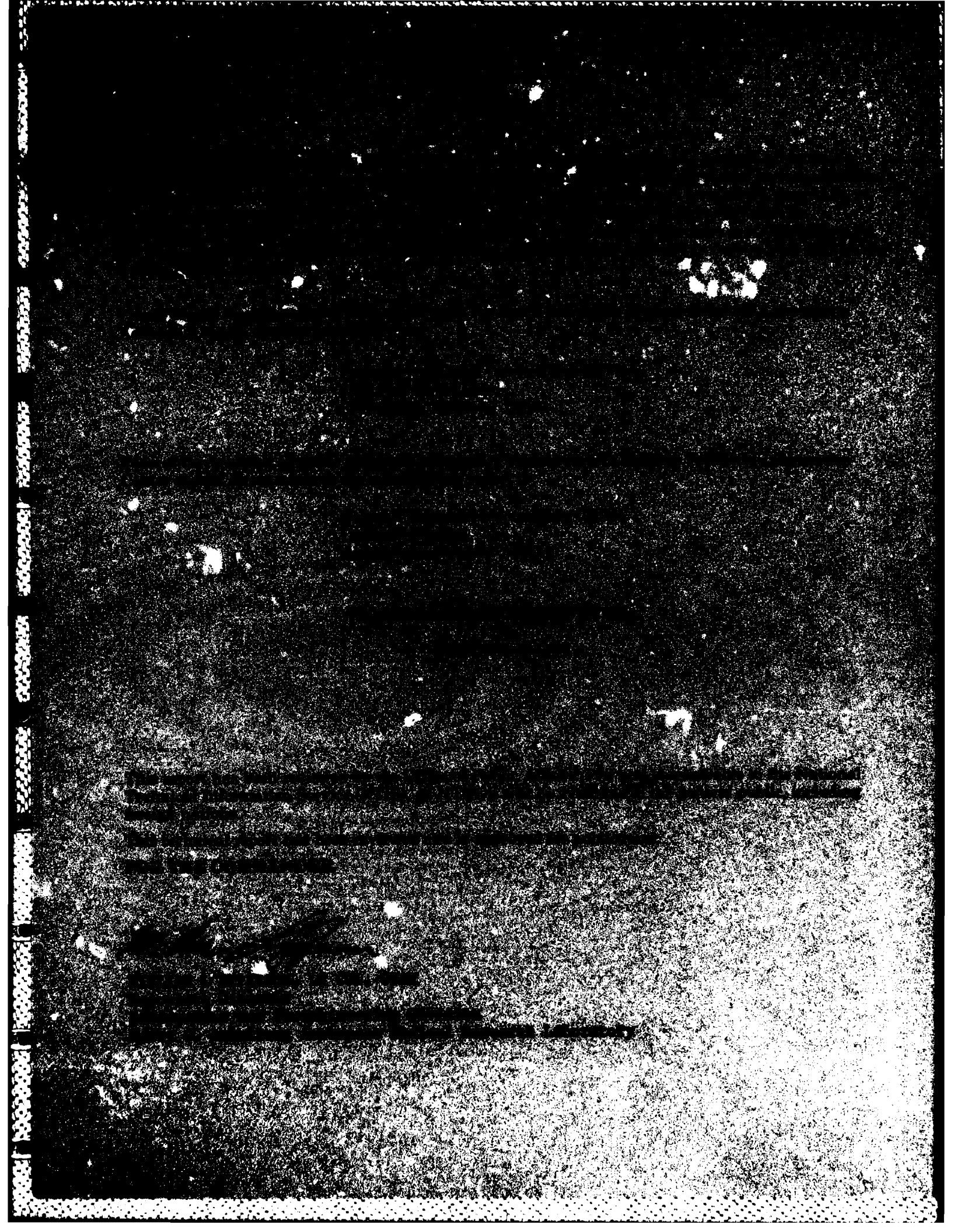
MICROCOPY RESOLUTION TEST CHART
NATIONAL BUREAU OF STANDARDS-1963-A

AD-A161 425

THIS PAGE COPY

DTIC
S ELECTED
SERIALS

85 11 14 200



AD-A161425

REPORT DOCUMENTATION PAGE

1a. REPORT SECURITY CLASSIFICATION UNCLASSIFIED			1b. RESTRICTIVE MARKINGS	
2a. SECURITY CLASSIFICATION AUTHORITY			3. DISTRIBUTION/AVAILABILITY OF REPORT Approved for public release. Distribution Unlimited.	
2b. DECLASSIFICATION/DOWNGRADING SCHEDULE				
4. PERFORMING ORGANIZATION REPORT NUMBER(S) AAMRL-1R-85-019			5. MONITORING ORGANIZATION REPORT NUMBER(S)	
6a. NAME OF PERFORMING ORGANIZATION Northwestern University		6b. OFFICE SYMBOL (If applicable)	7a. NAME OF MONITORING ORGANIZATION AAMRL/BB	
6c. ADDRESS (City, State and ZIP Code) Dept. of Civil Engineering Evanston, Illinois 60201			7b. ADDRESS (City, State and ZIP Code) Wright-Patterson AFB, Ohio 45433-6573	
8a. NAME OF FUNDING/SPONSORING ORGANIZATION U.S. Air Force/AFSC		8b. OFFICE SYMBOL (If applicable) PMRSB	9. PROCUREMENT INSTRUMENT IDENTIFICATION NUMBER F33615-80-C-0523	
8c. ADDRESS (City, State and ZIP Code) Aeronautical Systems Wright-Patterson AFB, Ohio 45433			10. SOURCE OF FUNDING NOS.	
11. TITLE (Include Security Classification) See reverse side			PROGRAM ELEMENT NO. 61102F 62202F	PROJECT NO. 2312 7231
12. PERSONAL AUTHOR(S) T. Belytschko, J. Williams, M. Rencis			TASK NO. V3 23	WORK UNIT NO. 24 03
13a. TYPE OF REPORT FINAL		13b. TIME COVERED FROM 80 May TO 84 May	14. DATE OF REPORT (Yr., Mo., Day) 1985 July	
15. PAGE COUNT 135				
16. SUPPLEMENTARY NOTATION				
17. COSATI CODES			18. SUBJECT TERMS (Continue on reverse if necessary and identify by block number)	
FIELD	GROUP	SUB. GR.	Biomechanics, Structural Dynamics, Mathematical Modeling, Impact, Ejection Injuries, Head-Spine Structure, Cervical Spine, Muscles.	
06	02			
06	07			
19. ABSTRACT (Continue on reverse if necessary and identify by block number)				
<p>SAM (for Structural Analysis of Man) is a three-dimensional discrete element mathematical model developed for the prediction of the dynamic response of the head-spine-torso structure to severe impact environments. Although it is referred to as SAM in this report, it is important to note that this model is also known as the Armstrong Aerospace Medical Research Laboratory's (AAMRL) Head-spine Model (HSM). The model mathematically describes the equations of motion for a system of rigid bodies representing, for example, the head, torso segments and the pelvis, interconnected by deformable elements representing, for example, the intervertebral discs, ligaments and other connective tissues. SAM consists of two distinct components; a general purpose, large displacement, dynamic structural analysis program and a data base containing a number of data sets each of which contains material, geometric and inertial property, connectivity and loading environment data. This arrangement of</p> <p style="text-align: right;">(cont.)</p>				
20. DISTRIBUTION/AVAILABILITY OF ABSTRACT UNCLASSIFIED/UNLIMITED <input checked="" type="checkbox"/> SAME AS RPT <input type="checkbox"/> DTIC USERS <input type="checkbox"/>			21. ABSTRACT SECURITY CLASSIFICATION UNCLASSIFIED	
22a. NAME OF RESPONSIBLE INDIVIDUAL EBERHARDT PRIVITZER			22b. TELEPHONE NUMBER (Include Area Code) (513) 255-3665	22c. OFFICE SYMBOL AAMRL/BBM

11. (continued): Head-Spine Structure Modeling: Enhancement to Secondary Loading Path Model and Validation of Head-Cervical Spine Model

19. (continued):

independent software (except for a few special purpose subroutines) and data base allows for considerable flexibility in the definition and implementation of new features and the construction of data sets corresponding to models of various levels of complexity.

This report describes the following: 1) the development of a model of the diaphragm which, when incorporated into the HSM, will significantly enhance its ability to replicate the effects of the secondary $+G_z$ loading path through the viscera-abdominal wall/diaphragm/rib-cage system; 2) a discussion of spinal injuries associated with pilot ejection and proposed injury criteria for the cervical spine; 3) an axisymmetric finite element analysis of a lumbar vertebral body with comparisons to other models and specific attention to the question of material distribution effects on stresses; and 4) frontal ($-G_x$) and lateral ($+G_y$) impact simulations using the recently developed Head-Cervical Spine Model and comparisons of simulation results with experimental data. This last item is of particular interest because of the good agreement observed between model predictions and measured kinematics for both $-G_x$ and $+G_y$ impact events. Based on these results, the Head-Cervical Spine Model does appear to be a viable analytical tool for application to the prediction of head-cervical spine structure kinematics in frontal and lateral impact environments.

PREFACE

The research reported herein was funded under Air Force Contract F33615-80-C-0523. The Air Force project monitor was Dr Eberhardt Privitzer of the Modeling and Analysis Branch, Biodynamics and Bioengineering Division, Harry G. Armstrong Aerospace Medical Research Laboratory of the Aerospace Medical Division of the Air Force Systems Command, Wright-Patterson Air Force Base, Ohio.

DTIC
ELECTE
NOV 21 1985
S **D**
B

Accession For	
NTIS	CPAS1
DTIC	Y B
Unann	
Jan	
By	
Dis	
Av	
Dis	
A-1	



TABLE OF CONTENTS

Section	Page
I INTRODUCTION	1
II THE DIAPHRAGM - MODELING CONSIDERATIONS	5
Anatomy	5
Mechanical Behavior of the Diaphragm	10
Material Properties of Diaphragm Muscle	14
Reflex Control	19
Modeling the Diaphragm	20
III INJURY MECHANISMS IN PILOT EJECTION	23
Operational Data	23
Proposed Mechanisms of Injury	27
Proposed Injury Criteria for the Neck	34
IV AXISYMMETRIC FINITE ELEMENT ANALYSIS OF A LUMBAR VERTEBRAL BODY	37
Model	40
Stress Nomenclature	42
Comparison of Models C and S	47
Comparison with Earlier Model	50
Comparison with a Simplified Model	54
Comparison of Models S and SM	63
Comparison of Various Finite Element Models	69
V HEAD-NECK SIMULATION RESULTS	75
-G _x Impact Simulation	76
-G _x Impact Simulations with the Head-Neck Model Isolated from the Lower Spine	78

TABLE OF CONTENTS (continued)

Section	Page
V	
HEAD-NECK SIMULATION RESULTS (continued)	
-G _x Impact Simulations with the Head-Neck Model Combined with a Simplified Thoracolumbar Spine Model	87
+G _y Impact Simulation	101
+G _y Impact Simulation with the Head-Neck Model Isolated from the Thoracolumbar Spine	102
+G _y Impact Simulations with the Head-Neck Model Combined with a Simplified Thoracolumbar Spine Model	103
Summary and Conclusions	116
REFERENCES	123

SECTION I

INTRODUCTION

Increasing airspeeds over the past 40 years have made the safe ejection of crewmembers from disabled aircraft an increasingly difficult problem. It is necessary to subject the crewmember to very high acceleration levels, and this requires a better understanding of the factors underlying injury and the development of predictive techniques by which new ejection devices or existing devices can be evaluated. Experimental studies, while irreplaceable, are of limited usefulness because tests near the tolerance limits can only be conducted on cadavers or nonhuman primates. Thus a means of bridging the gap between low amplitude human volunteer tests and high amplitude animal tests is essential.

Computer models are an ideal means for bridging the gap. Since the essential phenomena should appear in both nonhuman primates and humans, a computer model can be validated by severe load experiments on nonhuman primates. Low load experiments on human volunteers and nonhuman primates will indicate how effectively the differences are modeled. The efficacy of the model in its domain of primary interest can be examined by comparing its predictions with injury data for existing ejection devices.

The Air Force Aerospace Medical Research Laboratory (AFAMRL) of Wright Patterson Air Force Base has been engaged in the development of computer techniques for analytically predicting the dynamic response of the human spine over the past 20 years. The methods developed range from lumped parameter, single degree of freedom models to multidegree of freedom models, in which each of the torso segments containing the vertebrae is represented by a rigid

body and the connective tissues are represented by deformable elements. The first model of this type was developed under AMRL sponsorship by Y.K. Liu, (AMRL-TR-73-75). This model is limited to two dimensional motions of the spine in the sagittal plane and was restricted to small displacements of the vertebrae. Furthermore, it was of limited generality, so it could not be used for developing a data base for humans and primates.

Belytschko et al. (1976) have developed a three dimensional discrete element model under AMRL sponsorship, SAM (Structural Analysis of Man). This model imposes almost no restrictions on the magnitudes of the deformations or material nonlinearities; although when excessive deformations occur within a single element, difficulties can develop. An essential feature of the SAM model is its generality with respect to the input data. All of the physical characteristics, geometry, material properties and inertial data bases are distinct entities, and the same model can be used for both humans and primates. Data bases of varying degrees of complexity have been developed for the human body and rudimentary data bases have been developed for the rhesus monkey, baboon and chimpanzee.

This generality has also made it possible to introduce additional anatomical features when they are deemed to be of importance. The major obstacle in adding new features are the conceptional difficulty of formulating the model and obtaining the required data. In this report, these preliminary aspects are considered for the diaphragm. The elements of the diaphragm essential to modeling pilot response are delineated, available data is reviewed, and some suitable models are outlined.

The second aspect of this report concerns an essential link in the application of the SAM model to crewmember safety studies, the interpretation of the output, or in other words, the response of the model, in terms of the

possibility of injury. The output consists of displacements, velocities and accelerations of all anatomical components and forces and moments sustained by these components. In ejection, the primary concern is focused on injury to the spine, and experimental information on vertebral body strength is insufficient to directly relate force and moment levels to injury. Therefore, it becomes necessary to relate the output of the model to quantities such as stress levels in the bone for which more extensive experimental information is available.

At the present time, an injury postprocessor is available for SAM which determines the injury potential of an environment by computing the stresses in the cortical bone of the thoracolumbar vertebral bodies and comparing this to cortical bone strength. This provides rudimentary guidelines to injury potential, but only treats a limited group of injury mechanisms. In this report, a more intensive examination of injury mechanisms has been initiated and the suitability of finite element models for determining injury criteria is investigated.

To conclude the report, some very successful simulations of the response of the head and neck to G_x and G_y environments are described. These have been compared to experimental results. The simulations exhibit all of the salient features of the experimental results and also agree quite closely as to magnitudes of velocities and accelerations. This excellent agreement in kinematical quantities provides indirect substantiation to the predicted forces, which are more relevant to injury, and indicates substantial potential for this model.

SECTION II

THE DIAPHRAGM - MODELING CONSIDERATIONS

2.1 Anatomy

The diaphragm is a dome-shaped sheet of musculo-fibrous tissue separating the abdominal and thoracic cavities. The usual configuration of the diaphragm is concave down as shown in Figure 1. The muscle fibers in the diaphragm project radially from an aponeurotic (sheet-like) central tendon. This central tendon lies at a slightly lower level than the peaks of the lateral muscular parts. The central tendon consisting of collagenous connective tissue, is trilobular in shape and is located immediately below the pericardium (Figure 2). The muscular portion of the diaphragm is divided into individual muscle digits or slips on the left and right sides. Each side of the diaphragm arises as one sternal slip, six costal slips and one lumbar slip. Accordingly, the origin of the diaphragm is grouped into three parts: (Figure 3)

1. The sternal part consists of two muscle bands and arises from the dorsal side of the xiphoid process.
2. The costal part arises from the cartilagenous and bony segments of the lower six ribs on each side. These muscle slips interdigitate with the transversus abdominis muscle near their points of attachment to the ribs. (Figure 4).
3. The lumbar part consists of three points of attachment on each side:
 - a. The medial arcuate ligament is a tendon which attaches medially to the vertebral bodies of L1 and L2 and laterally to transverse processes of L1 and L2.

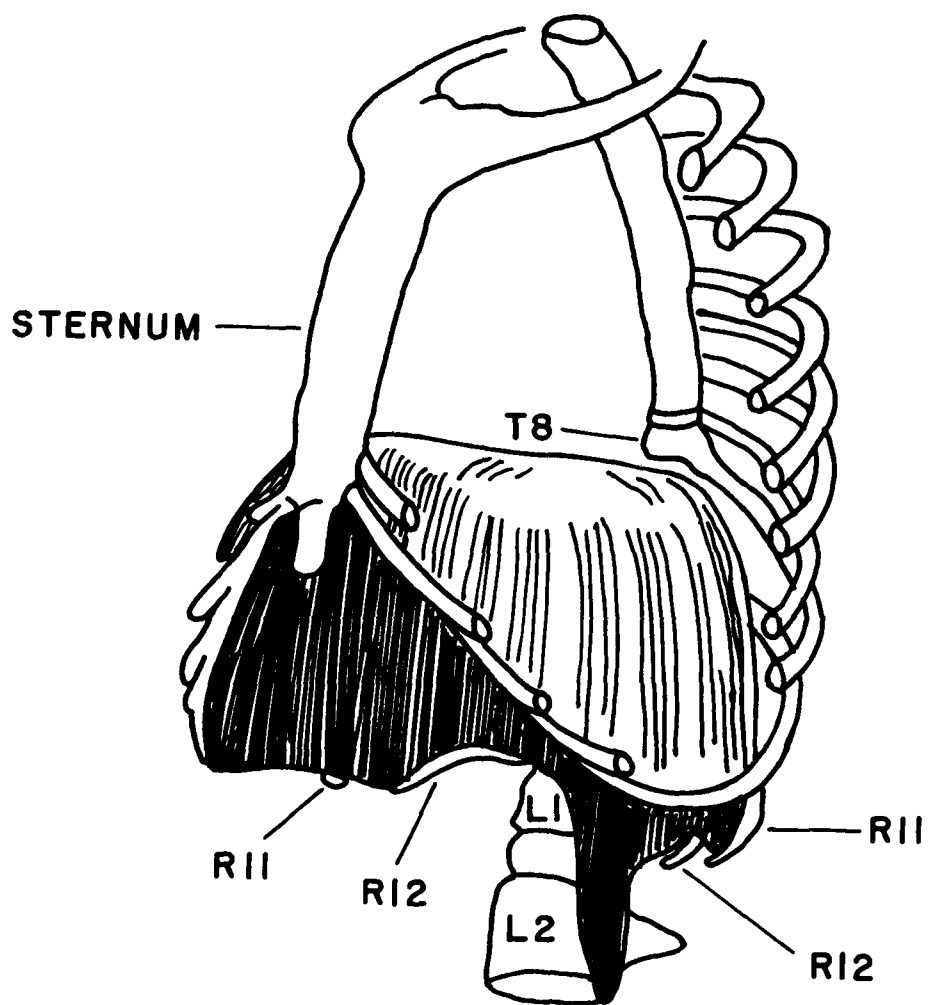


Figure 1. Configuration of Diaphragm after Forceful Expiration.

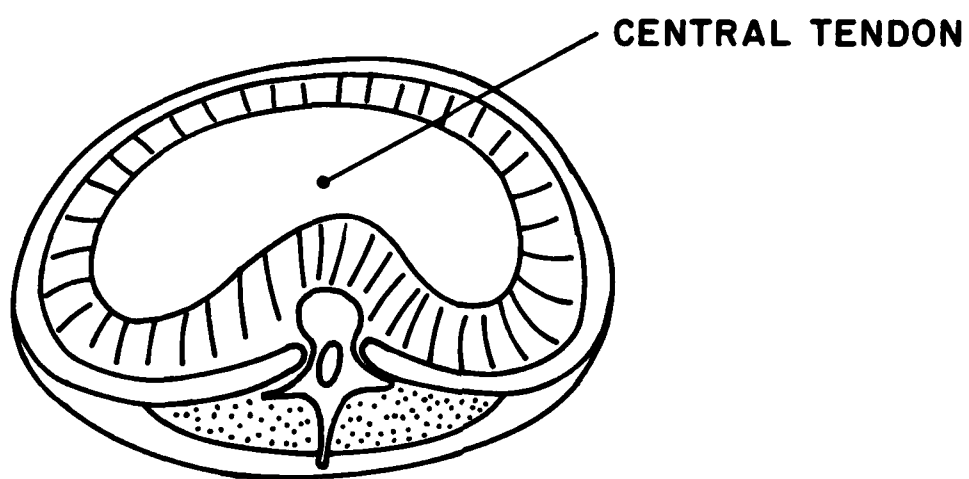


Figure 2. Diaphragm Viewed from Above.

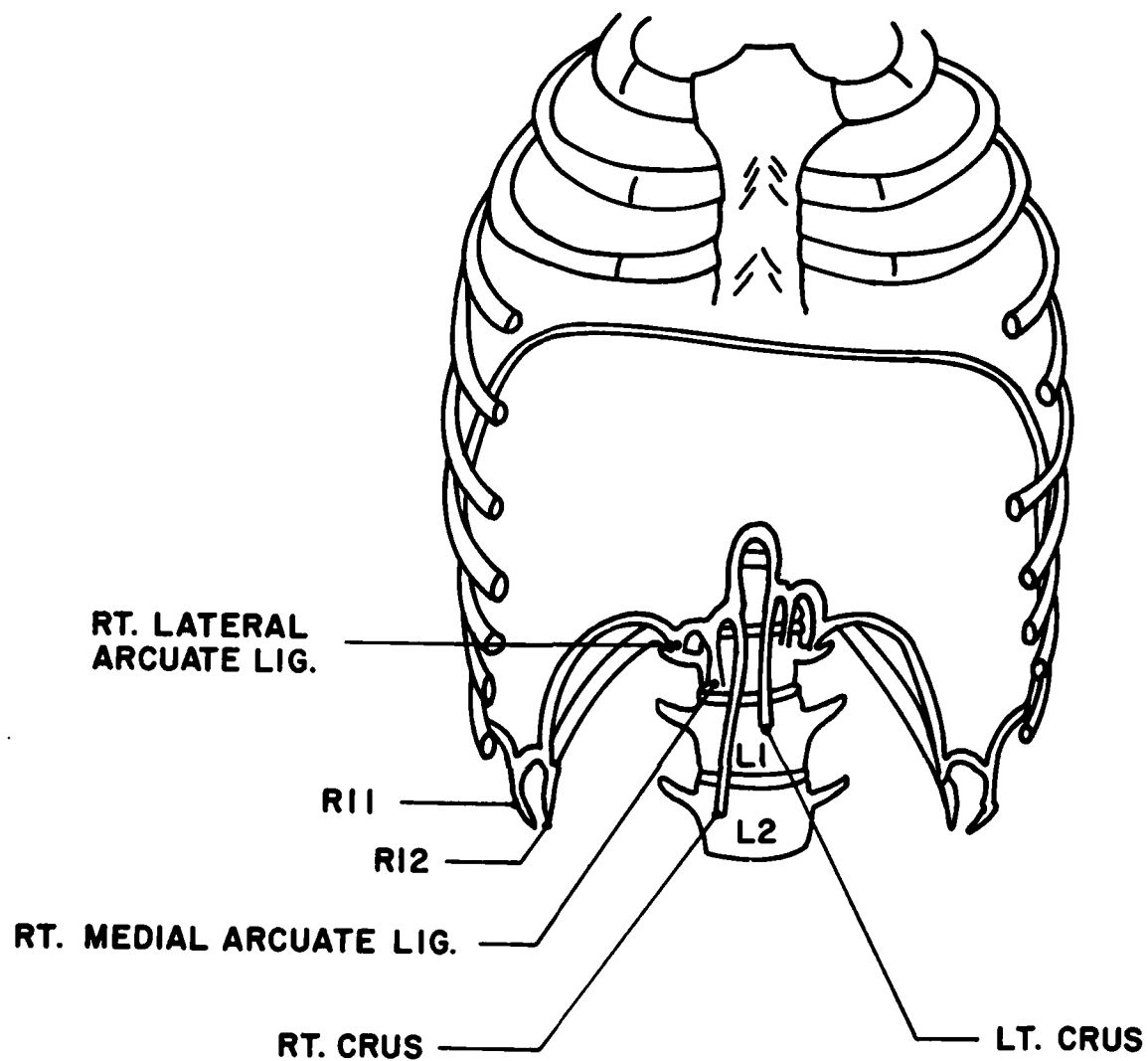


Figure 3. Anterior View of Diaphragm with Anterior Portions of Diaphragm and Rib Cage Cut Away to Show Origins of Diaphragm.

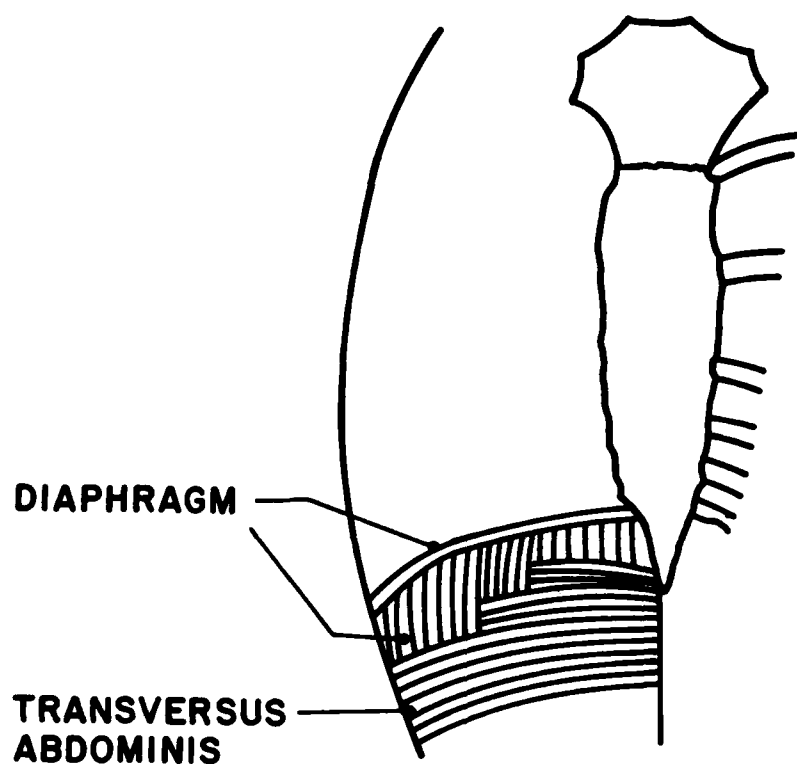


Figure 4. Interdigitation of Diaphragm with Transversus Abdominis.

- b. The lateral arcuate ligament is a tendon which attaches medially to the transverse process of L1 and laterally to the tip of rib 12.
- c. Crura are leg-like tendons of which there is one on each side. The right crus is broader and longer than the left and arises from the bodies and intervening disc of L1 and L2. The reason for the lack of symmetry is probably because the right side of the diaphragm, which covers the liver, needs to over-come a greater resistance than the left side, which lies over the stomach (Warwick et al., 1973).

The level of the diaphragm varies continuously. During quiet respiration the dome of the diaphragm descends to about the level of T11 and the total excursion of the diaphragm is about 1.5 cm. During deep respiration the dome of the diaphragm descends to the level of T11 as well, but the total excursion can amount to as much as 10cm. (Campbell et al., 1970). After a forced expiration the dome is level with T8 (Figure 1).

The average thickness is about 5 mm for the canine diaphragm (Kim et al., 1976).

2.2 Mechanical Behavior of the Diaphragm

The mechanics of the diaphragm has been investigated mainly in relation to respiration. The basic action of the diaphragm during breathing is as follows: In normal inspiration, the lowest ribs are held stationary by accessory muscles while the diaphragm contracts, pulling the central tendon downwards and forwards, with little change in the curvature of the diaphragm. The diaphragm pushes down on the abdominal contents and the

abdominal wall displaces outward until its limit of extensibility is reached. In the traditional view the diaphragm then uses the viscera as a fulcrum to elevate the lower ribs and thereby increases the dimensions of the rib cage (Derenne et al., 1978a). In normal expiration elastic recoil of the lungs and the tone of the abdominal muscles force the diaphragm upward. Although the diaphragm continues to contract well into the expiratory stage it does so with ever decreasing intensity (Basmajian, 1967). In forceful expiration active contraction of the abdominal muscles against the viscera can exert a powerful upward force on the diaphragm. Additional muscles are also used in respiration to raise and lower the rib cage but only the diaphragm is of interest here.

The actual mechanism linking diaphragm and rib cage motion is not well understood and is still being investigated (Derenne et al., 1978). One hypothesis that has been put forward recently is the Goldman and Mead hypothesis (Goldman and Mead, 1973). They hypothesized that rather than using the viscera as a fulcrum, the diaphragm can elevate and expand the relaxed rib cage only to the extent that the abdominal pressure increases. This is still a hypothesis and is known to be invalid in the supine position and during Mueller maneuvers (Macklem et al., 1979). It is conceivable that contraction of the abdominal muscles could under certain conditions play a role in inspiration. Contraction of the abdominal muscles results in inward movement of the abdomen and a rise in abdominal pressure. As to whether or not this elevates the rib cage in the way that contraction of the diaphragm does is unknown (Derenne, 1978a).

Anatomically the diaphragm is divided into eight left and eight right muscular slips. It has now been shown that the diaphragm consists functionally of two muscles that act differently on the rib cage (De Troyer et

al., 1981). In experiments performed in dogs the costal and crural parts of the diaphragms were stimulated separately. Stimulation of the costal part of the diaphragm increased the lower rib cage diameter. Stimulation of the crural part, on the other hand, decreased the dimensions of the lower rib cage so long as the abdominal pressure was not allowed to increase. Although in the living intact dog the expiratory effect of the crural part is balanced by a rise in abdominal pressure, this study showed that the diaphragm consists of muscles which are functionally different from each other.

Goldman et al. (1978) studied the relationship between the pressure across the diaphragm (P_{di}), which is the difference between abdominal pressure (P_{ab}) and pleural pressure (P_{pl}), and neural excitation of the diaphragm, as assessed by EMG (E_{di}). The relationship between E_{di} and P_{di} depends on two steps: The first relates neural excitation (E_{di}) to muscle force as determined by the force-length characteristics of the muscle. The second step involves the relation between muscle force and P_{di} which is dependent on diaphragm curvature. Grassino et al. (1978) attempted to determine which of these steps in going from E_{di} to P_{di} is more important. The subjects of this study performed "static" inspiratory efforts, i.e. efforts against a closed airway at given abdominothoracic configurations. Although the investigators were unable to show which step is more important, they did show that abdominothoracic configurations rather than lung volume, determine the relationship between P_{di} and E_{di} . At constant E_{di} , the P_{di} developed was four to eight times more sensitive to changes in abdominal dimensions than rib cage dimensions.

Kim et al. (1976) studied the mechanics of the diaphragm in anaesthetized dogs. Both P_{di} and the diaphragmatic tension were measured simultaneously at different lung volumes during constant tetanic stimulation of the diaphragm.

It was shown that Pdi is linearly dependent on diaphragmatic tension at different lung volumes. Direct observation of the diaphragm from below as it contracted did not reveal any significant change in the diaphragmatic shape or contour. Roentgenographic observations suggest that these findings are true for man as well and that the action of the diaphragm resembles that of a piston (Kim et al., 1976). In these experiments the abdomen of the animals were open at atmospheric pressure. Pdi was therefore equal to esophageal pressure. Calculations were made of the diaphragmatic radius of curvature using Laplace's law and assuming spherical geometry. It was shown that the calculated radius of curvature remained at about 3 to 4 cm for lung volumes ranging from 400 ml below to 600 ml above functional reserve capacity. At lung volumes of 600ml and above the radius of curvature, the diaphragmatic muscle decreased instead of increasing as would have been predicted. Therefore, Kim et al. concluded that the length-tension behavior of the diaphragm muscle is far more important than the geometric properties given by Laplace's law in determining the diaphragmatic action.

Gates et al. (1980) measured the radii of curvature of the passive dog diaphragm muscle directly using a laser-camera system. Two local radii of curvature were measured, one in the fiber direction of the diaphragm muscle and one in the cross fiber direction. The measurements were made in vivo with the thoracic cavity open to atmospheric pressure. Pdi was therefore equal to the intra-abdominal pressure. The contractile response of the diaphragm was prevented by a crurariform drug. It was shown that the radius of curvature in the crossfiber direction remained at 5 cm with changes in the abdominal pressure ranging from 6×10^3 to 14×10^3 N/m². The radius in the fiber direction decreased from 7 cm at a Pdi of 6×10^3 N/m² to 4 cm at a Pdi of 10×10^3 N/m². It is then increased gradually to 5 cm at a Pdi of 14×10^3 N/m².

2.3 Material Properties of Diaphragm Muscle

Gates et al. (1980) determined that the passive diaphragm muscle in situ behaves as an anisotropic linearly elastic material for loads in the physiological range. Mohan and Melvin (1980) tested dumb-bell specimens obtained from human autopsies. Their results showed that the viscoelasticity of the passive response was negligible for strain rates between 0.05 to 100 S⁻¹. However, their stiffness measurements showed much variation which may be due to the effects of rigor mortis or to the unphysiological state of muscle tissue that has been cut and isolated from its blood supply. This causes stiffening and shortening along the cut edges of the specimen and can cause the specimen to bear load unevenly (Gates et al., 1980). Kim et al. (1976) cleverly circumvented these problems by using a diaphragm strip preparation with intact nerve and blood supply to study the force-length behavior. These are the only published accounts of the passive stress-strain relationship of the diaphragm muscle. The contractile properties have been reported on most recently by Glebovskii (1961), Sant'Ambrogio et al. (1970), Vachon et al. (1975), Kim et al. (1976), Edwards (1979), and Faulkner et al. (1979).

Gates et al. (1980) developed a ring transducer to measure the orthogonal stresses and strains in the in situ dog diaphragm and proposed a model of the diaphragm. Strains in both fiber and cross-fiber directions varied linearly with Pab. The stresses were determined by assuming for the diaphragm, in addition to an axis of revolution in the horizontal plane, an axis of revolution in the cranio-caudal direction. Then, equilibrium of a wedge shaped element of the diaphragm wall yields

$$\sigma_x = p R_x \left(1 - \frac{R_x}{2R_z} \right) / t$$

$$\sigma_z = p R_x / 2t$$

$$\sigma_y = -p/2$$

where p is the pressure across the diaphragm (P_{di}), x refers to cross-fiber direction and z to fiber direction (See Figure 5); R_x and R_z are the curvatures in the x and z directions and t is the thickness. It was further shown, using stress-strain equations for the case where the cross-fiber plane is a plane of symmetry and assuming the incompressibility condition $\epsilon_{ii} = 0$, that

$$\epsilon_z = \frac{p}{4E'} \left(\frac{R_x^2}{tR_z} + 1 \right)$$

$$\epsilon_x = \frac{p}{E} \left(1 - \frac{E}{4E'} \right) \frac{R_x}{t} - \frac{R_x^2}{2tR_z} + \left(1/2 - \frac{E}{4E'} \right)$$

where E is Young's modulus in the fiber direction and E' the modulus in the cross fiber direction. Using this model and the experimental stress-strain data, Gates et al. calculated $E' = 0.5 \times 10^6 \text{ N/m}^2$, $E = 0.79 \times 10^6 \text{ N/m}^2$.

Kim et al. determined the passive and active force-length relationships for their canine diaphragm strip preparations as shown in Figure 6. They defined the in situ resting length as the length at which passive tension first appeared. Normally the negative pressure in the lungs stretches the diaphragm to about 16% beyond its resting in situ length (Kim et al., 1976).

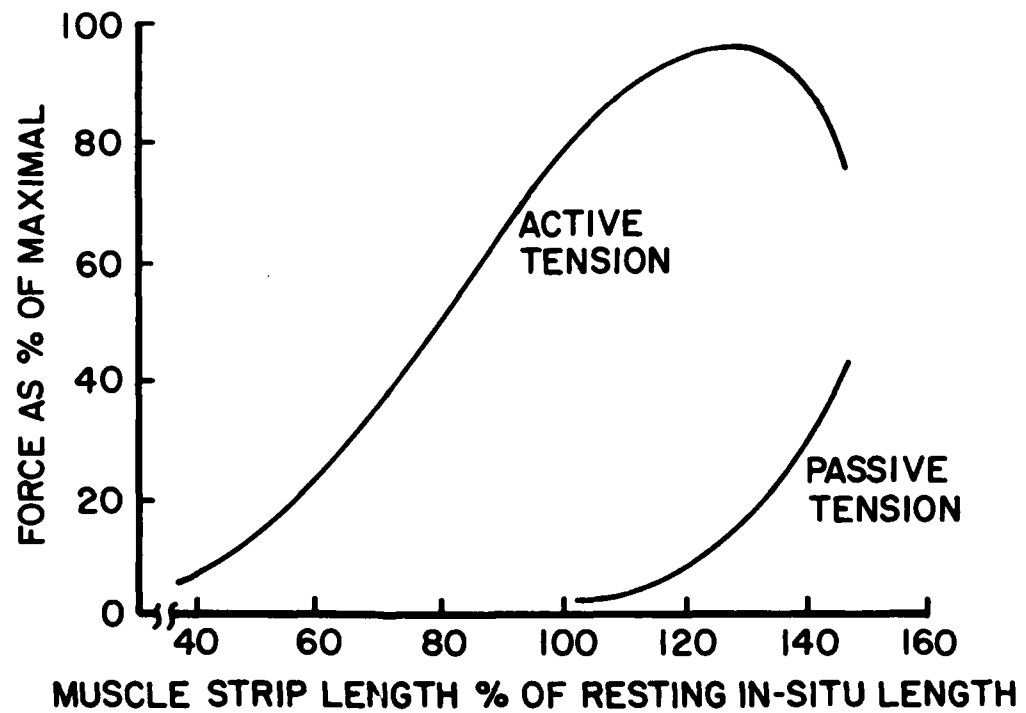
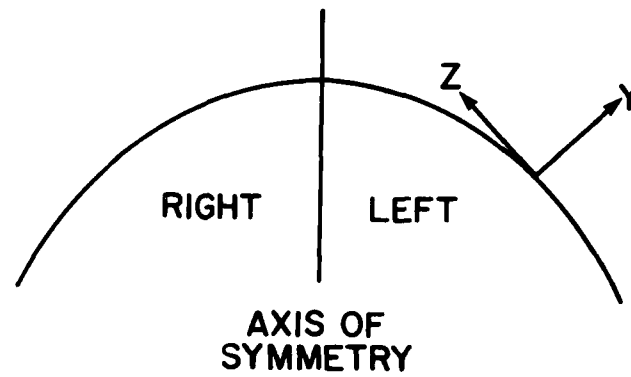


Figure 6. Active and Passive Force-Length Relationship for the Canine Diaphragm Muscle.

They found the diaphragm to have a much broader effective length range than other skeletal muscles. Maximal active tension was obtained at 10 to 30% (average 25%) beyond the resting length in situ. This is in contrast to other skeletal muscles where the maximal active tension is obtained at the in situ resting length. (Ralston et al., 1947; 1949). It was further found that tension was still being generated at lengths as short as 42% of the in situ resting length. Active tension drops to zero at 50 to 60% of the in situ resting length for other skeletal muscles (Garamvolgyi, 1971). Heart muscle stands at the other extreme compared to skeletal muscle with maximal active tension being developed at 50 to 60% beyond the length at which passive tension first appears. Kim et al. (1976) therefore suggested that the diaphragm is mechanically in between cardiac and skeletal muscle.

The tension developed by a muscle depends on the frequency at which it is being stimulated. At low frequencies the force that is developed oscillates in magnitude. As the frequency of stimulation increases tetanus develops, that is, the response smoothens and reaches a plateau. Further increases in frequency of stimulation have little effect. Edwards (1979) found the in vitro frequency-force characteristics of the human diaphragm to be similar to those of the in vivo sternomastoid and quadriceps muscles. Figure 7 shows the force-frequency response. The frequency at which complete tetanus occurs is seen to be about 40 Hz for the human diaphragm. For the cat diaphragm it is 20 Hz (Glebovskii, 1961) and for the dog 30 Hz (Vachon et al., 1975).

The maximal isometric tetanus tension developed per cm^2 of muscle fiber cross section is about 2 kg for muscles of many mammals (Close et al., 1972). Diaphragms of rats and cats develop tensions of 2 kg/cm^2 , but human diaphragm samples develop only 0.4 kg/cm^2 (Faulkner et al., 1979). The lower tension developed in human specimens may be due to trauma incurred during

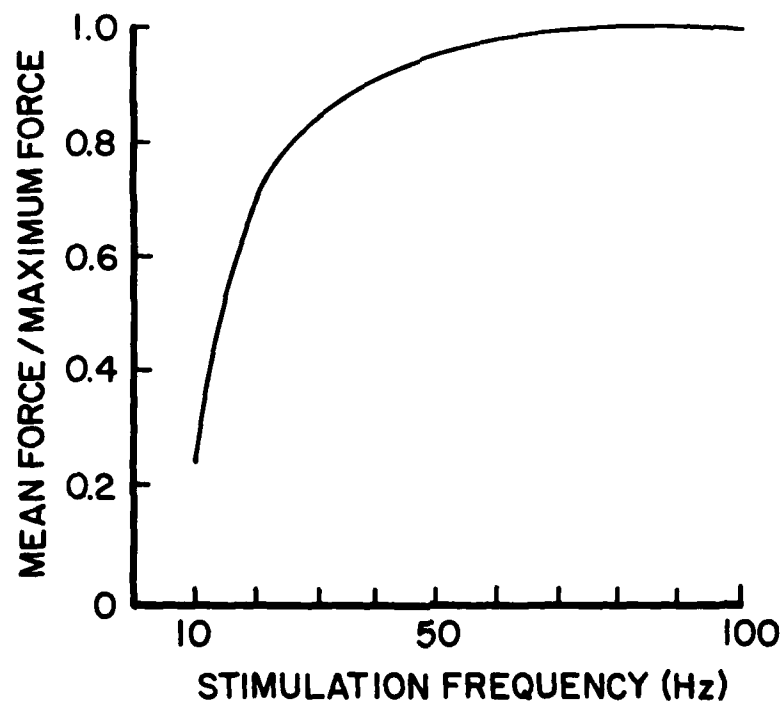


Figure 7. Frequency-Force Characteristics of diaphragm muscle. (From Edwards Am. Rev. Respir. Dis. 119, (2 Pt. 2) P. 82, Fig. 1)

surgical removal. In the dog diaphragm muscle preparations of Kim et al. (1976), the blood supply was kept intact and the specimens averaged an active force of 1.25kg per cm².

The maximum velocity of shortening under no load in tetanus experiments for muscle fibers from the human diaphragm is 3 fiber lengths per sec (Faulkner et al., 1979) whereas for fibers from the rat diaphragm it is 10 fiber lengths per sec (Ritchie, 1954). For both species this maximal velocity of shortening is midway between that of a slow twitch muscle such as the soleus and a fast twitch muscle such as the extensor digitorum longum (Faulkner et al., 1979).

2.4 Reflex Control

The diaphragm is poor in muscle spindles but rich in Golgi tendon organs (Derenne, 1978b). The muscle spindle detects length changes of the muscle and the Golgi tendon organ detects tension in tendons. These receptors send signals to the spinal cord to control reflex contractions of the muscle. Sudden stretching of a muscle excites the spindles and causes a muscle reflex contraction called a spindle reflex or a stretch reflex. The Golgi tendon organ has exactly the opposite effect. Tension in the muscle is transmitted to the tendon and excites the tendon organ. Signals from the tendon organ to the spinal cord then cause inhibition of muscular contraction. If the tension becomes too great inhibition from the tendon organ causes a decrease in the tension by a feedback loop. If the tension is too low impulses from the tendon organ decrease or stop so that muscular tension again increases.

No stretch reflex has been demonstrated for the diaphragm (Jung-Cailliot et al., 1978; Corda et al., 1963). However, there is evidence to suggest that

a reciprocal relationship exists between diaphragmatic excitation and length (Bruce, 1979). Maximal voluntary diaphragmatic EMG has been found to decrease as the diaphragm lengthens. The reason for this is thought to be inhibition of diaphragmatic excitation resulting from Golgi tendon organ activation (Libet et al., 1959). Similarly, decreased inhibition from the tendon organ has been suggested as an explanation for how the diaphragm compensates for loss in contractile force when in a disadvantageous position in the length-tension curve (Bruce, 1979).

2.5 Modeling the Diaphragm

Since our primary purpose for modeling the diaphragm is to investigate the mechanism of transmitting loads during impact acceleration, details pertaining mainly to respiration can be neglected. For purposes of modeling the dynamic response, we can assume that at the onset of impact the diaphragm is just starting to contract, i.e. inspiration is about to begin. It then takes the diaphragm another 100 msec before developing peak contraction (Sant'Ambrogio, 1970; Vachon et al., 1975; Faulkner et al., 1979). Furthermore, it has been shown that the diaphragm does not stop contracting at the end of inspiration, but is active during as much as two-thirds of expiration (Petit et al., 1960). We can therefore assume that the impact event will be over before contraction of the diaphragm ceases. On the other hand it may be instructive to also examine the case where the diaphragm is fully contracted at the start of impact acceleration.

On the basis of the anatomy and physiology as it has been described, a simple model can be proposed. In this model the diaphragm muscle is represented by 16 muscle elements, one for each of the muscle slips as they

are known to exist. The central tendon consists of collagenous tissue and its overall stiffness might be estimated from the known properties of collagen. The central tendon could, for simplicity, be treated as a rigid plate to which the muscle elements are attached. This may be sufficient since the action of the diaphragm is said to resemble that of a piston; the muscular portion of the tendon pulls the central tendon down with little change in curvature. If the viscera are modeled by hydrodynamic elements, the interaction between the viscera and the diaphragm could take place through intermediate sliding nodes on each muscle element (Figure 8).

The number of intermediate sliding nodes needed for each muscle slip must be sufficient to obtain a realistic curvature of the diaphragm. While two or three stacks of hydrodynamic elements within the diaphragm areas may be sufficient to model the load transfer from the viscera through the diaphragm to the ribs and spine, it is not clear whether its sufficient to maintain a realistic shape for the model of the diaphragm. The advantage of using muscle elements with intermediate sliding nodes is that this feature has already been developed in the model (Williams et al., 1983). The only work which needs to be done is to choose the proper muscle constants so that the unique properties of the diaphragm muscle's contractile behavior are adequately modeled. Furthermore, this may not be absolutely necessary to replicate the shape of the diaphragm as long as the line of action of the diaphragm muscle is adequately represented.

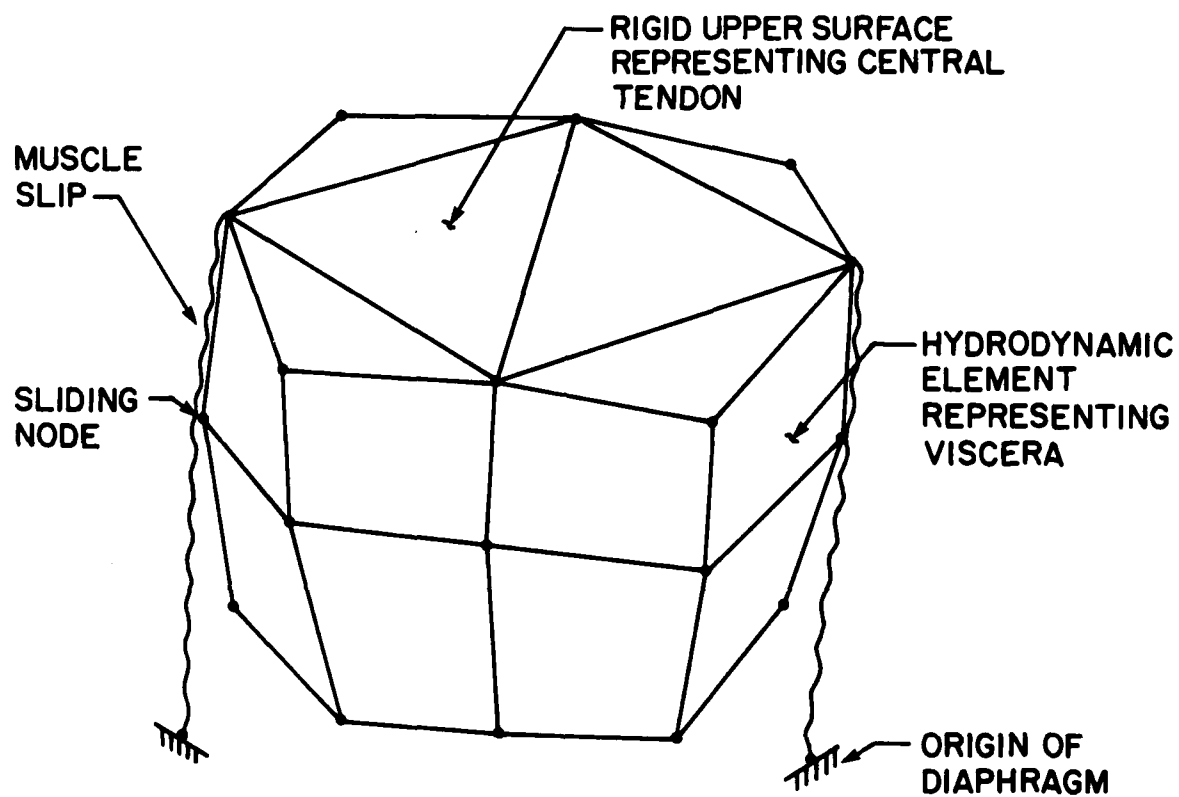


Figure 8. Model of diaphragm muscle showing two of twelve muscle slips.

SECTION III

INJURY MECHANISMS IN PILOT EJECTION

3.1 Operational Data

From the published accounts of human ejection it is apparent that spinal injury occurs mostly through compression fractures of the vertebral bodies. The most common type of compression fracture experienced during ejection is the anterior wedge fracture. This typical injury occurs in the region of T12-L1. Other modes of fracture include lateral wedge fracture, cleavage fracture, fractures due to muscle spasm, and fractures of the processes. All of these types of trauma are considered to be acceptable from the survivability standpoint. Unacceptable types of injury are dislocations and fractures involving the articular facet joints and the posterior wall of the centrum (Kazarian, 1975).

The available literature on human ejections does not always include details on the specific locations of the spinal injuries that occurred. It is recognized, however, that the most frequently injured area is the thoraco-lumbar region (Kazarian, 1975 and Rotondo, 1975). To get an idea of the magnitude of the problem, consider Table 1.

Although most of the fractures occur in the thoraco-lumbar transition region there are also fractures in the upper thoracic, even cervical, and in the lower lumbar region. The most frequently observed X-ray profile is an anterior wedge-like fracture (Rotondo, 1975). The Swedish study (Hirsch and Nachemson, 1961) reported that a fourth of all injuries merely consisted of a central depression of the upper end-plate. The USAF data is somewhat misleading in that 928 USAF ejections were made in 1960 through 1964, and of

TABLE 1

PILOT EJECTION DATA

Study	Time Period	Number of Ejections	Number of Pilots Surviving Ejection	Number of Pilots with Fractures*	Number of Fractures
Swedish Royal Air Force (Hirsch et al., 1961)	1957-1960	---	55	14	32
USAF (Chubb et al., 1965)	1960-1964	928	729	28	---
U.S. Navy and Air Force (Moffatt and Howard, 1968)	1959-1967	---	1000	170	---
Italian Air Force (Rotondo, 1975)	20 years	100	89	15	23
British Air Force (Crooks, 1970)	1957-1959	---	70	13, 43**	---
British - Fryer's data	1949-1960	---	200	41+(28)***	82
French Army (Delahaye et al., 1964)	1951-1963	204	149	13****	---

*Attributed to the ejection process itself, not to landing.

**13 fractures were recorded upon examination after ejection.

43 fractures were recorded upon examination 10 years after ejection.

***28 cases of "minor" injury, see text.

****Only those vertebral fractures leading to disability are included.

these only 729 ejections were included in the study. Not included were missing persons, multiple extreme injuries, and downward and rotational ejections. None of the other studies in Table 1 included missing persons or non-surviving cases, either. However, by not including multiple extreme injuries the rate of spinal injury due to ejection is made to appear less serious in the USAF than it may in fact be. For example, Jones et al., (1964) documented in the 1958-63 incidence of spinal fracture from the Marin-Baker seat utilized by the British, U.S. and Swedish Air Force. Frequency of fracture, according to him, was comparable for the British and U.S., being about 21%. The British study by Fryer (1961), quoted by Henzel et al., (1968), recorded incidents of "minor" injury which he defined as painful spinal symptoms or signs in the presence of "normal" X-rays. It is debatable how many of these were due to undetected end-plate fractures or other undetectable fractures. The study of Crooks (1970) in which 70 subjects were examined 8 to 10 years or more post ejection presents some interesting findings. Forty-three subjects had radiological evidence of crush fracture of the vertebral bodies. However, at the time of the ejection only 13 fractures were recorded. According to Crooks this discrepancy may be accounted for by either (1) a failure to detect the fracture by X-ray, or no X-ray given (only 47 subjects were X-rayed) or (2) subsequent collapse of the vertebrae damaged during the ejection. Interestingly, fifty-eight subjects were free of symptoms at the time of the study, eleven had minor disability, and six patients shown to have crush fractures denied ever having symptoms in their back. Delayed disability following ejection is thus not of clinical importance for at least ten years post-ejection. It is not known, though, if these initially undetected fractures will result in difficulties at some later date. Another finding in this study (Crooks, 1970), is the high incidence

(70%) of radiological changes of cervical spondylosis immobility, which is much higher than in civilians at age forty where the incidence is 25%.

Although many of these sequelae may have little clinical significance, they indicate that the forces sustained approached the limits of tolerance. They also indicate possible damage to the cervical area where the incidence of fracture is lower than in the thoraco-lumbar. Recent interest in the use of helmet-mounted devices makes the cervical spine an area of potential injury and it is significant to note that limited injury to this area of the spine has been found even without helmet-mounted devices.

The types of spinal injuries have been classified into three major groups (Kazarian, 1975):

- (1) compression fractures of the vertebral body
- (2) fracture dislocations
- (3) radiologically concealed fractures

The first group includes over 78% of all operational spinal injuries (Kazarian, 1975). The second group then accounts for some of the remaining operational injuries, although the actual percentage has not been specified. In fact, many of these cases may not even be included in the published statistics since there may be few survivors with injuries in this category. The third group of course has an unknown rate of incidence although one might infer from Crook's study (1970) that it could include more than 40% of all ejectees. Roentgenograms cannot be depended upon to show even gross lesions involving the centrum, pedicles, articular processes or end-plates (Kazarian, 1975).

3.2 Proposed Mechanisms of Injury

The four major mechanisms resulting in spinal injuries are vertical compression, flexion, extension and rotation (Roaf, 1960).

Vertical Compression

Biomechanical investigations of spinal injuries have concentrated on the compression induced injury. Roaf (1960) studied the interaction of the vertebrae and the intervertebral discs under vertical compression. He found that while there is a very slight bulge of the annulus, there is no alteration in the shape of the nucleus pulposus, and the major distortion is a bulge of the vertebral end-plate. Direct measurements of vertebral end-plate deformation were made by means of suspended extensometers, without reference to points outside the motion segment, by Rolander and Blair (1975). At small loads they found that only the disc was deformed, but at larger loads the vertebra deflected at a greater rate than the disc. Bulging of the end-plates causes blood to be squeezed out of the cancellous bone of the vertebral body into the perivertebral sinuses. This was considered by Roaf to be an important shock-absorbing mechanism in the spine. Upon further loading the end-plate bulges more and finally cracks. Although Roaf made no quantitative studies, he claimed, on the basis of radiographic studies of dye-injected nuclei pulposi, that prior to end-plate fracture there is no distortion of the normal nucleus pulposus. As quoted in the paper by Menzel et al. (1968), Perey (1957) of Sweden found that end-plate fractures occur at an appreciably lower level of loading than is required to reach the proportional limit of the vertebral body and by the time 16 percent compression of a vertebral body has occurred, one or both end-plates have usually exceeded their breaking point.

As Henzel et al. (1968) point out end-plate and vertebral body damage are far more likely to occur during spinal axial loading than is intervertebral disc disruption. This is substantiated by the infrequent reports of disc damage as a result of ejection.

Kazarian and Graves (1977) tested the compressive strength and failure behavior of the vertebral centrum at different loading rates. They stated that the mechanical properties of the vertebral centrum depend to a great extent on the viscosity of the marrow, the number and sizes of the orifices which perforate the cortex of the centrum, as well as the rigidity of the bone itself. They observed slow percolation of viscous marrow which exuded from the large number of orifices in the cortex at low displacement rates (0.21 in/min). This outflow of blood was not observed at high displacement rates (2100 in/min) until after fracture of the cortex occurred. They reasoned that whenever the vertebral centrum is axially compressed, its contents will be pressurized and that the observed increase in vertebral strength at higher strain rate is due to hydraulic strengthening. These conclusions and findings are contradictory to those of Swanson and Freeman (1966) and Pugh et al. (1973) who did their studies on the femur. They discounted any theory attributing the mechanical response of trabecular bone in the femur to the fluid present around the trabeculae. In the study by Swanson and Freeman a viscous fluid was injected into a dried and defatted femur. No exudation was observed during testing implying perhaps that the cortex of the femur has less orifices than the cortex of the centrum. Pugh et al. (1973) used 3/8 inch diameter plugs of 5 mm length taken from the cancellous portion of the femur and compared the behavior of fresh wet specimens and defatted bone specimens. Their conclusion that the fluid in the intertrabecular spaces has no effect on the dynamic mechanical behavior is questionable since they apparently did not

contain their specimens while testing. There can be no pressure build-up of surrounding fluid in such a test. Nevertheless, it may be that anatomical differences between the femur and the vertebral body, such as the extent of perforation of the cortical shell by blood vessels, can account for these contradictory opinions on hydraulic strengthening. Another factor to be considered is that neither Swanson and Freeman nor Pugh et al. tested their material into the failure range. Nevertheless, the evidence seems to indicate that in the vertebral body there exists some sort of hydraulic shock absorbing mechanics (Henzel, 1968 and Roaf, 1960) and strengthening mechanics (Kazarian, 1977).

Compression forces are responsible for a number of non-fatal fractures in egress injury. These fractures have been classified by Kazarian (1975) as: (1) fractures of the vertebral body margins, (2) anterior wedge fractures, (3) lateral wedge fractures, and (4) cleavage fractures of the centrum. The anterior and lateral wedge fractures occur when flexion forces are combined with compressive forces. The anterior wedge fracture is the most common non fatal egress injury. It is considered to be clinically benign and complete recovery is possible. Pain and discomfort, however, may be significant and may cause two or more months of disability. This injury is characterized by collapse of the anterior part of the vertebral body. It is typically found in the regions C5-T1 and T11-L2. The lateral wedge fracture is more dangerous as damage to the spinal cord may result. Cleavage fracture of the centrum is a Y-shaped fracture as viewed from the front of the vertebral body. It is probably due to an increase in hydrodynamic pressure created within the vertebral body during ejection. The end result is an explosion of the centrum.

Flexion

When forces that produce flexion of the spine are combined with other forces acting in an axial direction on the vertebral body, then the above described anterior wedge compression fracture may result. As established by King and Vulcan (1971) the spine is subjected to this type of loading during ejection. The bending effects are due to the sagittal plane curvatures of the spine and the eccentricity of the torso with respect to the spine are enhanced by the forward rotation of the head and torso (Prasad and King, 1974). It has been demonstrated that the articular facets tend to unload during ejection and go into tension, causing the lumbar vertebral bodies to sustain a greater compressive load (Prasad and King, 1974). This occurs when the head and torso undergo maximum forward flexion.

Rotation

The intervertebral discs, joints and ligaments are very resistant to compression, distraction, flexion and extension, but very vulnerable, especially in the cervical region, to rotation and horizontal shearing forces (Roaf, 1960). According to Roaf, the clinical appearance of a cervical dislocation or fracture-dislocation, usually attributed to hyperflexion, is really the result of rotation. Experimentally, Roaf was unable to rupture the spinal ligaments by either hyperflexion or hyperextension without first fracturing the bone. But, horizontal shear, and especially moments easily produced ligamentous rupture and dislocation. He found that if moments are applied while the spine is held in slight flexion then the posterior ligaments, joint capsules and posterior longitudinal ligaments tear in that order and a dislocation results. Roaf's rule is that, in general, moments produce dislocations, and compressive forces produce fractures.

Dislocations and fracture-dislocations are the most serious injuries of the spinal column. They fall into the unacceptable group of injuries whereas compression fractures fall into the acceptable group from the standpoint of surviving ejection. They have been classified as stable, if there is no facet overriding and the spinal column remains intact, and unstable if the posterior longitudinal ligament is torn and the articular processes are fractured (Kazarian, 1975). In the stable dislocation the displacement is essentially in angulation. In the unstable dislocation or fracture-dislocation usually one or more of the vertebral bodies are crushed and the upper vertebra is partially dislocated forward and sideward on the lower. Usually, extensive soft tissue lesions of the muscles and ligaments occur.

Extension and lateral flexion

Extension injuries are not considered in the present study, but according to Roaf (1960) they too are really rotation injuries. In both extension and lateral flexion crush fractures occur before rupture of the ligaments takes place (Roaf, 1960). Lateral flexion accompanied with axial compression can result in lateral wedge fractures described above.

Cervical Spine Injuries

Cervical spine injuries are classified according to the suspected mechanisms of injury which have already been described. The upper region, comprising the atlanto-occipital and the atlanto-axial joints, is subject to quite different injuries from the lower cervical region (C3-C7). Thus they are described separately:

Upper cervical spine

Dislocations in this region are fatal. Fractures of the atlas are caused by axial compression. Fractures of the odontoid process are usually connected with an anterior or posterior dislocation of the atlas. Anterior displacement of the atlas is thought to be associated with hyperflexion injuries whereas posterior displacement is caused by hyperextension injuries. Injury to the axis most often occurs through the narrow section of the arch with separation of the body of the axis from the C3 vertebra.

Lower cervical spine

Injuries to this region can be classified as either flexion or extension injuries. Since the present study concerns only flexion and hyperflexion there will be no description of extension-related injuries. Flexion injuries result when the head and neck are forced forward on the trunk beyond the normal limits. Braakman and Penning (1971) have classified flexion injuries into distractive hyperflexion and compressive hyperflexion.

Distractive Hyperflexion

Distractive hyperflexion occurs during deceleration where the flexion forces tend to separate the vertebral segments. Three types of injuries result.

Hyperflexion sprain

This is defined as a temporary and partial luxation of the intervertebral joints following traumatic hyperflexion under moderate forces, with rupture of the posterior ligaments and joint capsules but with the skeletal system still

preserved. This type of injury is relatively rare because major forces are usually required to rupture the posterior ligaments. These major forces usually result in the interlocking of the facets. Only rarely will the hyperflexion movement stop prior to interlocking (Braakman and Penning, 1968).

Unilateral facet dislocation

This occurs when there are rotation forces as well as distractive ones. Tearing of the interspinous ligaments and the capsule of one facet joint occurs, allowing the facets to dislocate.

Bilateral facet dislocation

This takes place when the flexion and distractive forces combined with rotation forces continue acting beyond the unilateral facet dislocation stage. Disruption occurs in the second facet as well, resulting in a complete dislocation.

Compressive hyperflexion

When the forces that cause flexion and rotation of the head and neck are combined with axial compression forces, various types of fracture can result.

Wedge compression fractures

This type of fracture has already been described. It occurs under mild compressive forces. It can occur with disruption of the posterior elements if the flexion force is strong enough.

Tear-drop fracture

If major compressive forces are combined with flexion, such as would take place if the flexed head struck an object like the canopy of the aircraft, a

fracture of the vertebral body occurs. This fracture derives its name from the large triangularly shaped fragment which is broken off from the anterior-inferior part of the vertebral body. A second major fragment of the inferior part of the body also usually occurs and this may be driven posteriorly into the spinal canal.

3.3 Proposed Injury Criteria for the Neck

A proposed injury criterion in extension and flexion of the neck is the equivalent moment at the occipital condyles. This equivalent moment consists of the moments produced by neck forces and chin-chest contact forces (Mertz and Patrick, 1971). The forces acting on the head are: the force of gravity, an axial force produced by the neck structure directed along the axis of the vertebral column parallel to the odontoid process, a shear force which produces a distributed bending moment along the cervical spine, and a chin-chest contact force. Mertz and Patrick conducted tests on a 50th percentile male volunteer for horizontal deceleration at various G-levels, including a maximum of 9.6G. These tests were conducted to determine the effects produced by varying the mass, center of gravity, and mass moment of inertia of the head by the addition of a helmet. The center of mass was varied from above the head's center of mass to below. In static tests on the volunteer, maximum torque levels of 3.54×10^8 dyne-cm in flexion and 2.38×10^8 dyne-cm in extension were obtained. There is no contribution from the chin-chest contact in the static tests. In dynamic tests maximum value of 4.76×10^8 dyne-cm was reached in extension. In hyperflexion the chin-chest reaction resulted in a maximum equivalent moment about the condyles of 8.84×10^8 dyne-cm sustained without injury. This exposure produced a pain extending from the back of the

neck to the middle of the back and resulted in a stiff-neck which lasted for several days. According to Mertz and Patrick (1971) the maximum voluntary static neck reaction is about 1.13×10^8 dynes in tension and 1.11×10^8 dynes in compression. For shear, the neck can withstand about 8.45×10^7 dynes. These static strength values apply to low G conditions where the viscous resisting forces produced by the muscles are not a large part of the resisting torque. In high G-situations, the viscous contribution of the muscle reaction is comparable to the static strength, resulting in a higher resisting moment than predicted by a static strength analysis. In other words, the static strength values quoted are a lower bound in the high acceleration environment (Mertz and Patrick, 1971). In cadaver tests, also in the horizontal direction, maximum torque levels of 1.77×10^9 dyne-cm and 1.9×10^9 dyne-cm were achieved without any apparent damage as determined by X-ray analysis. A maximum anterior-posterior force 2.1×10^8 dynes was developed at the occipital condyles of one cadaver without producing any apparent neck trauma. However, these values for the Mertz and Patrick cadaver studies should be viewed with caution. Not all fractures are visible on X-rays and it may not be possible to rule out ligamentous damage on the basis of X-ray examination alone.

A limited amount of strength data for individual components of the neck can be found in the literature. Sonoda (1962) reported strength tests on human vertebral discs and vertebral bodies from all major regions of the spine in compression, tension and torsion. Messerer (1880) reported a series of compression tests on human vertebral bodies from all levels of spines of cadavers ranging in age from 25 to 80 years. For the cervical region the maximum compressive breaking load of the vertebral bodies is 2.8×10^8 dynes to 4.2×10^8 dynes for the 20 to 40 year old (Messerer, 1880 and Sonoda,

1962). For the cervical disc the compressive breaking load is reported as 3.2×10^8 dynes for the 40-59 year old (Sonoda, 1962). The tensile breaking load of the cervical discs and vertebral bodies is about the same: 10^8 dynes (Sonoda, 1962); the torsional breaking moments are about 6×10^7 dyne-cm (Sonoda, 1962). The tensile strength of the ligaments in the neck is about 10-20 MPa ($1 \times 10^8 - 2 \times 10^8$ dynes/cm²) as determined for the ligamentum flavum (Tkaczuk, 1968) and longitudinal ligaments (Nachemson and Evans, 1967). In terms of maximum tensile breaking load, the transverse ligament of the atlas appears to be the strongest with a breaking load of 10^8 dynes (Fielding et al., 1974) followed by the anterior longitudinal ligament with a breaking load of 3.4×10^7 dynes and the posterior longitudinal ligament with a breaking load of 1.8×10^7 dynes (Tkaczuk, 1968). The ultimate tensile strength of human muscle has been estimated to lie between 2×10^6 and 6×10^6 dynes/cm² for stretching of the passive muscle (Katake, 1961). The estimated strength of active contracting muscle ranges from 4×10^6 to 10×10^6 dynes/cm² (Fick, 1910; Haxton, 1944; Morris, 1948).

SECTION IV
AXISYMMETRIC FINITE ELEMENT ANALYSIS
OF A LUMBAR VERTEBRAL BODY

The vertebral column, shown in Fig. 9 is composed of two essential parts:

- (1) vertebral bodies and intervertebral discs, which are weight bearing;
- (2) vertebral arches, which are protective.

In this analysis only the lumbar vertebrae (located in the lower back region) are considered, as shown in Fig. 10. The lumbar vertebral bodies are the largest and most massive in the vertebral column because the body weight borne by the spine increases towards the bottom of the column. The major components of a vertebra are the vertebral body and the neural arch. The arch is composed of two pedicles, two laminae, and has four articular processes, two transverse processes, and one spinous process.

Each vertebral body is a short, cylindrical block of bone flattened at the back and possessing a slight waist. At the macroscopic level, there are two main forms of bone tissue, called cortical (or compact) and trabecular (or cancellous) bone. The interior of the body is composed of trabecular bone which has a very spongy appearance and contains a substantial amount of fluid. The trabecular bone is enclosed circumferentially by a thin hard layer of dense cortical bone. The upper and lower surfaces of the body are composed of a thin, slightly porous, cortical bone, and are called end plates.

Extending from the back of the vertebral body is the vertebral arch, which is composed of two parts: 1) A very short rounded bar backwards from the body which is the pedicle. 2) An oblong plate with sloping surface known as the lamina. At the angular junction of the pedicle and lamina on each side there are three processes, one upward (superior), one downward (inferior), and

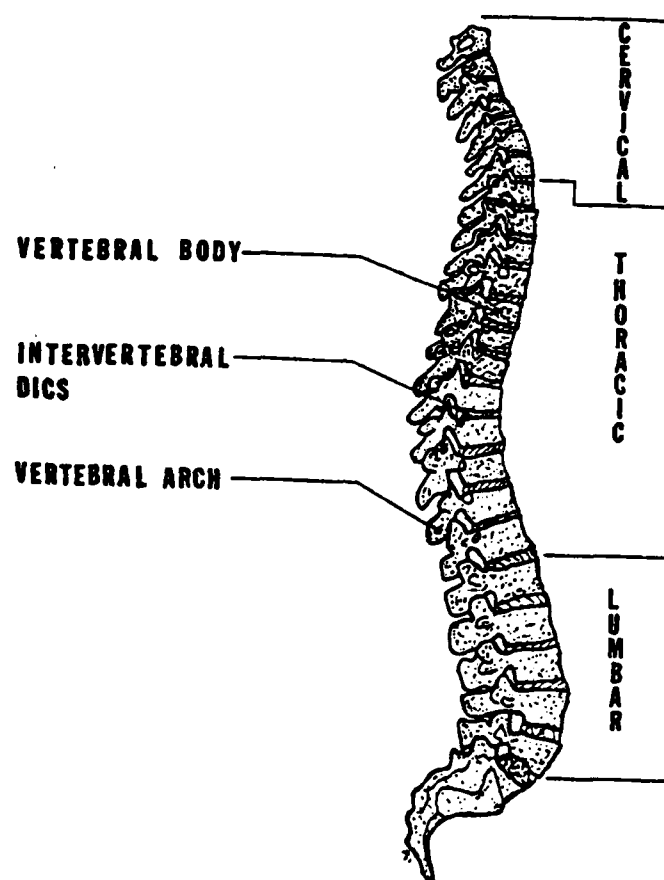


Figure 9. Vertebral column scheme illustrating different regions.

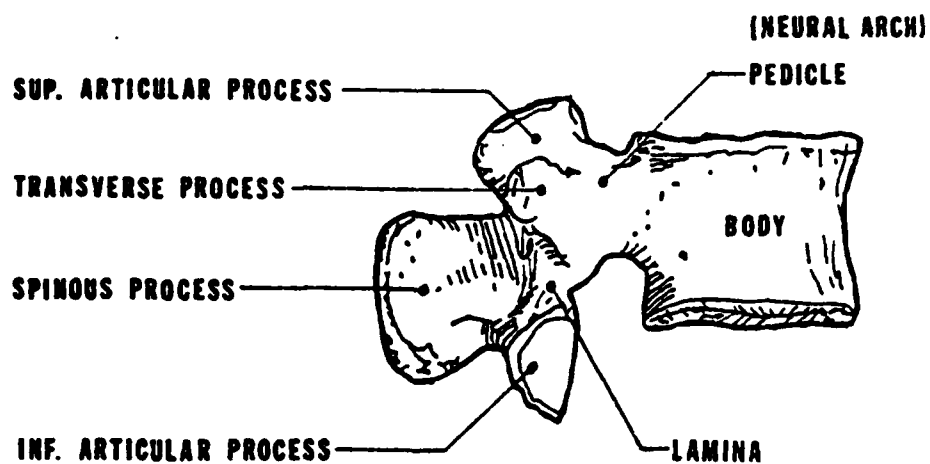
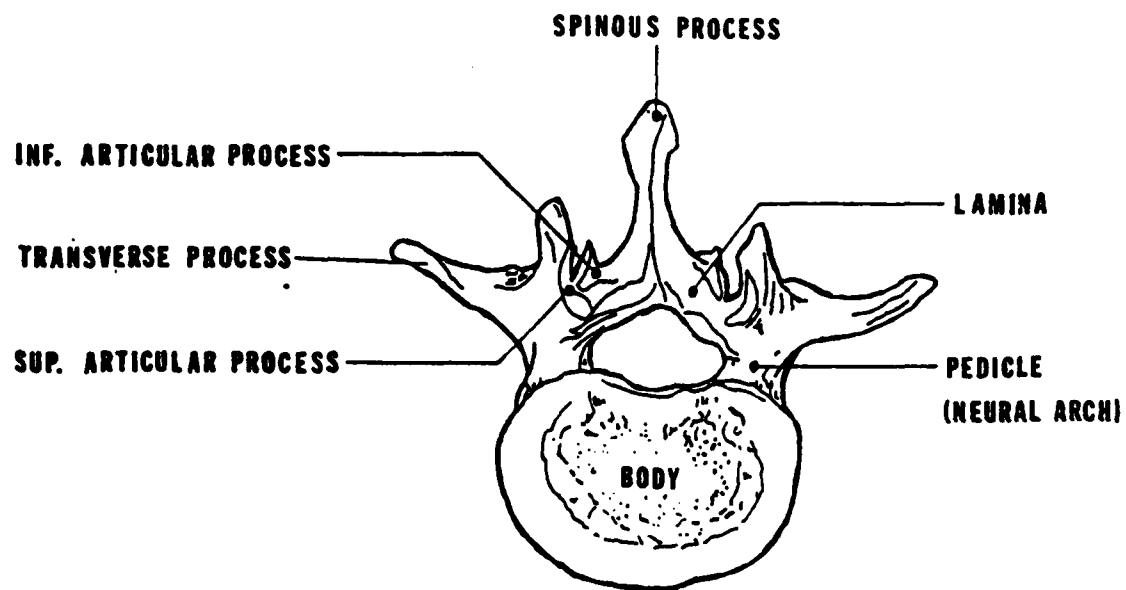


Figure 10. Human lumbar vertebra.

one lateralwards (transverse). The primary function of the superior and inferior process is to prevent movement between vertebrae, whereas the transverse process is for the attachment of muscles.

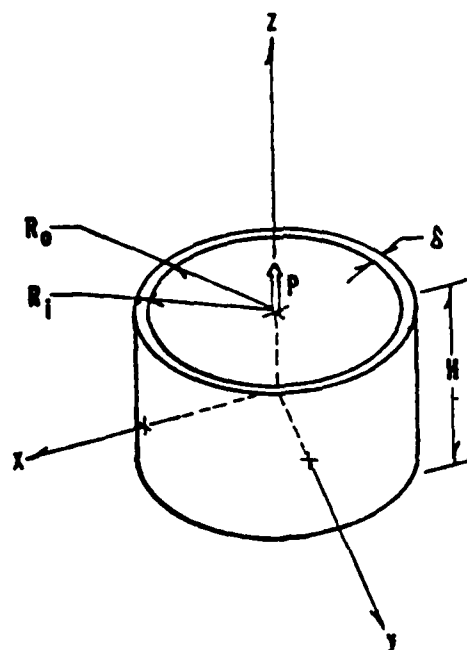
Each vertebral body is attached to those above and below it by the intervertebral discs and ligaments. The disc is composed of an inner nucleus pulposus surrounded by the annulus fibrosus. The nucleus pulposus is gelatinous and can be assumed to be in a hydrostatic state of stress.

Bone is an extremely complex material: it is an anisotropic, inhomogeneous, nonlinear, viscoelastic substance, and its properties are difficult to measure. However, much can be learned with linear elastic analysis. Many researchers have assumed the material to be transversely isotropic, but in this analysis only isotropic materials are considered.

Based on the measurements reported by Evans (1970), the elastic modulus of the cortical and trabecular bone will be taken to be 2.18×10^6 psi and 1.07×10^4 psi, respectively. Evans (1975), studied bone and found that it is weaker in tension than in compression, but this is neglected here. Poisson's ratio for both materials is taken as 0.25.

4.1 Model

The models in this section were developed to determine the stress distribution in the lumbar vertebral body. They will be used to evaluate whether the high bending moments predicted by the three-dimensional analysis of Plesha et al. (1980), is realistic and whether a gradient in the modulus reduces the bending stress. The author's model will then be exploited to assess the accuracy of Belytschko's simple model for the Air Force postprocessor, which is illustrated in Fig. 11. The models assume small



$$\begin{aligned} R_o &= 0.799 \text{ in.} & R_i &= 0.787 \text{ in.} \\ \delta &= 0.012 \text{ in.} & H &= 1.04 \text{ in.} \end{aligned}$$

Figure 11. Idealized vertebral model with dimensions.

deformation and linear material behavior.

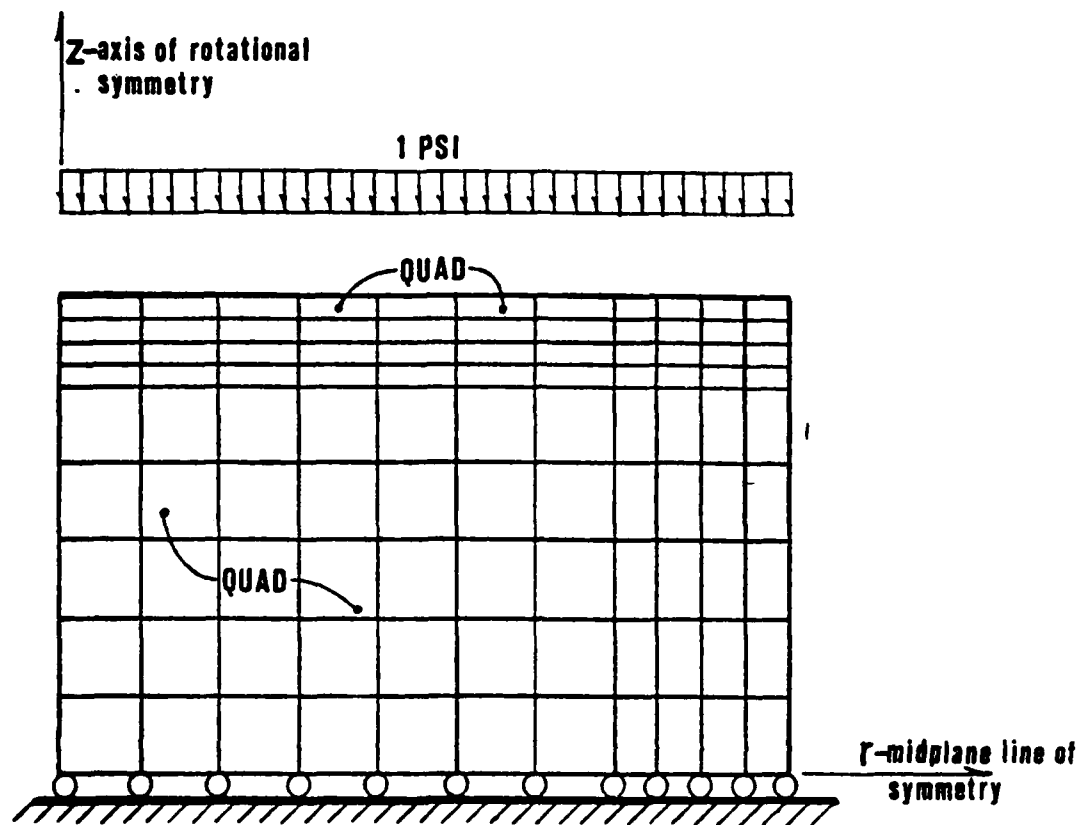
The two finite element models used to represent the lumbar vertebral body are: 1) Model C, in which both the trabecular and cortical bones are represented by axisymmetric quadrilateral, continuum elements. 2) Model S, in which axisymmetric quadrilaterals are used to model the trabecular bone and axisymmetric shell elements are employed to represent the cortical bone, as shown in Fig. 12. All projections from the vertebral body are neglected.

Both finite element models are similar to Belytschko's idealized model, but unlike the latter, fewer simplifying assumptions are needed for the analysis. As reported by Kulak et al. (1974), a uniform thickness of 0.012 in. was used for the cortical shell. Since the end plates are thinner than the cortical bone that encloses the trabecular bone circumferentially, its thickness is assumed to be 0.006 in. (see Fig. 12b).

4.2 Stress Nomenclature

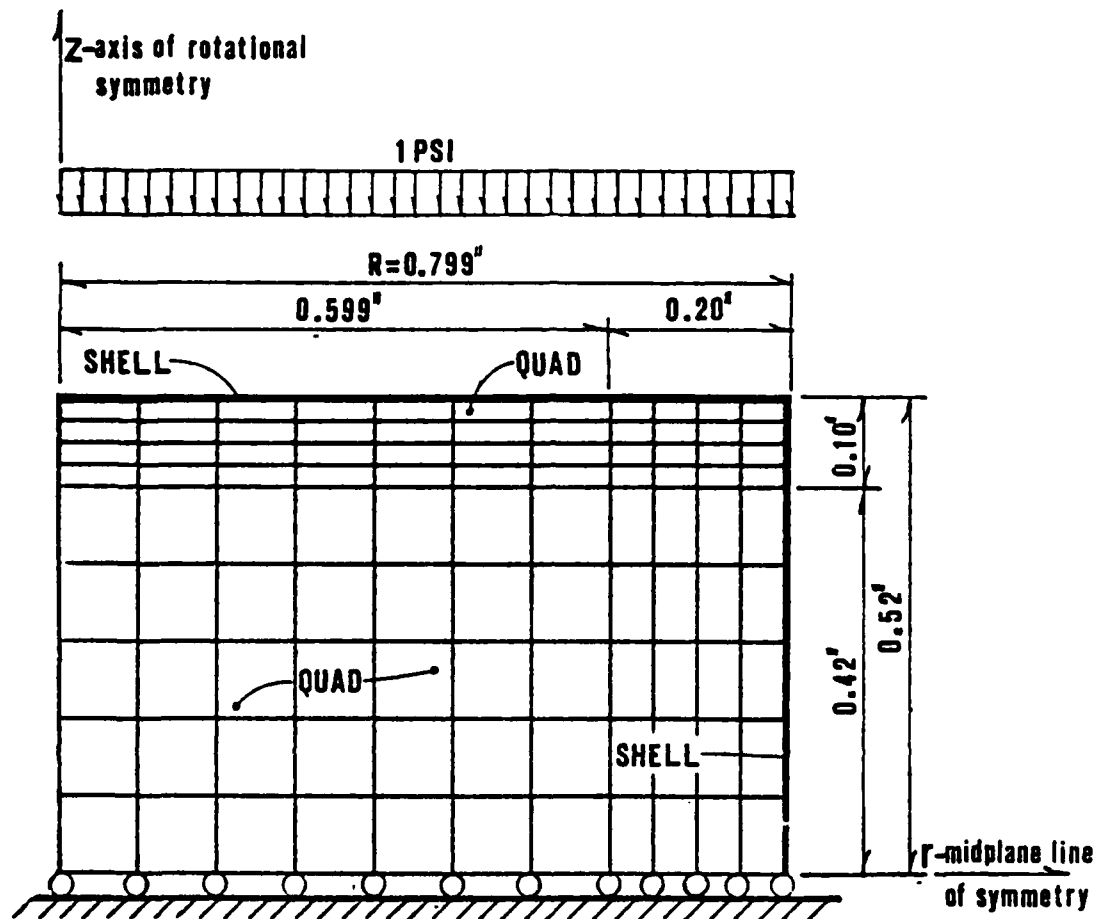
The stresses of interest are the membrane and bending stresses in the cortical shell, as shown in Fig. 14. The membrane stress is the average stress across the thickness. It consists of three types: axial, hoop, and shear stress. The bending stress corresponds to the part which varies linearly across the thickness. The total stress at any point is the sum of membrane and bending components.

A program written by the author was used for the analysis. This computer code employs axisymmetric shell and quadrilateral elements. The code is limited to linear, elastic analysis of isotropic bodies. The justification for not using a dynamic analysis is that the spinal column rarely experiences frequencies greater than 25 Hertz, which is far below the lowest natural frequency of a vertebra (Plesha et al., 1980).



Note: Dimensions same as in Fig. 12b, excluding shell elements.

Figure 12a. Finite element models, Model C.



Note: Shell thickness: end plates = .006 in.
 cylindrically = .012 in.

Figure 12b. Finite element models, Model S.

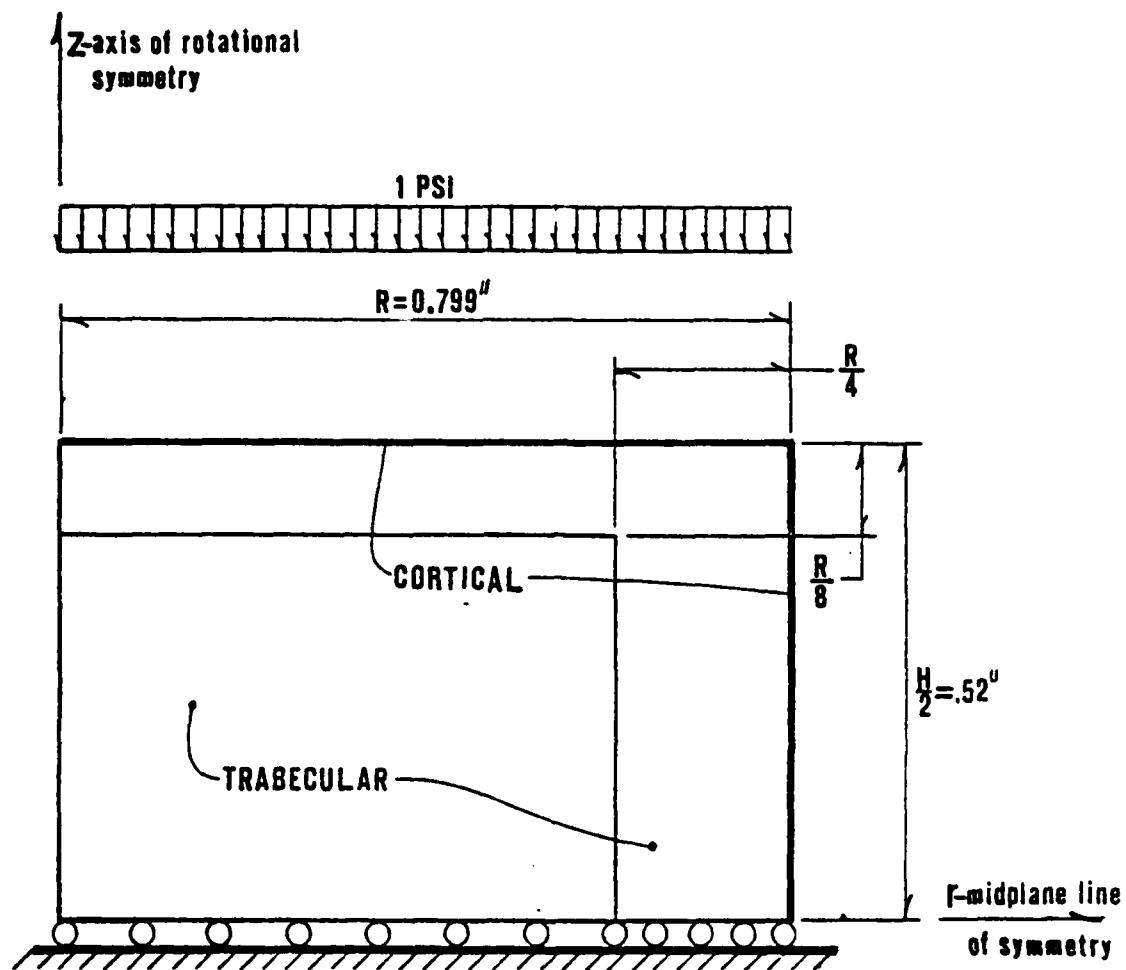
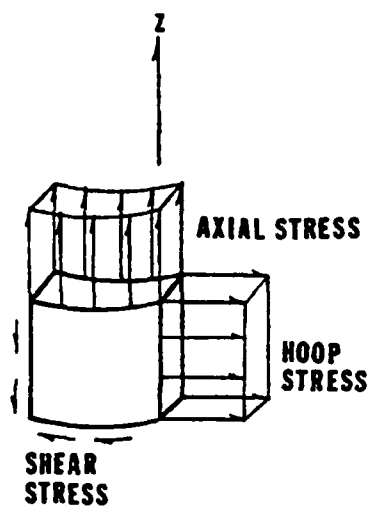
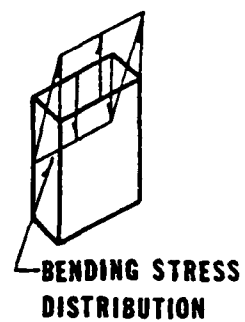


Figure 13. Modification of the idealized vertebral body.



a) Membrane



b) Bending

Figure 14. Stress Nomenclature.

4.3 Comparison of Models C and S

Models S and C, as mentioned previously, differ only in that shell and continuum elements are used for the cortical bone, respectively. Both Models C and S yield approximately the same results. The deflection along the outside edge of the end plate for both models was found to be very small, with the deflection near the center about two orders of magnitude larger. This increase in the deflection at the center is due to the softness of the trabecular bone as compared to the surrounding cortical bone.

The deflection at the center for Model S was found to be 1% smaller than Model C, which is insignificant. The axial forces cause concave bending of the end plates and convex bending of the sides, as illustrated in Fig. 15. This figure was obtained by magnifying the displacements, since actual displacements would not be visible.

In Fig. 16, the axial and radial stresses for Model C are shown; both models exhibit approximately the same stress distribution. A majority of the axial stress is sustained by the cortical bone, with the maximum stress at $z = H/4$ and near the outer circumference. Near the end-plates of both models, a majority of the load is carried by the trabecular bone. Towards the center of the vertebral body, the stresses transferred from the trabecular to the more rigid cortical bone. Thus, the axial stresses decrease in the trabecular region and increase in the cortical region towards the body's midplane.

Yokoo (1952) and Rockoff et al. (1969) reported that under vertical compressive loads, the cortex generally carries 45 - 75% of the applied load. Also Rockoff et al. (1969) reported that when the ash content of the vertebrae is less than 59%, a maximum of 40% of the applied load is carried by

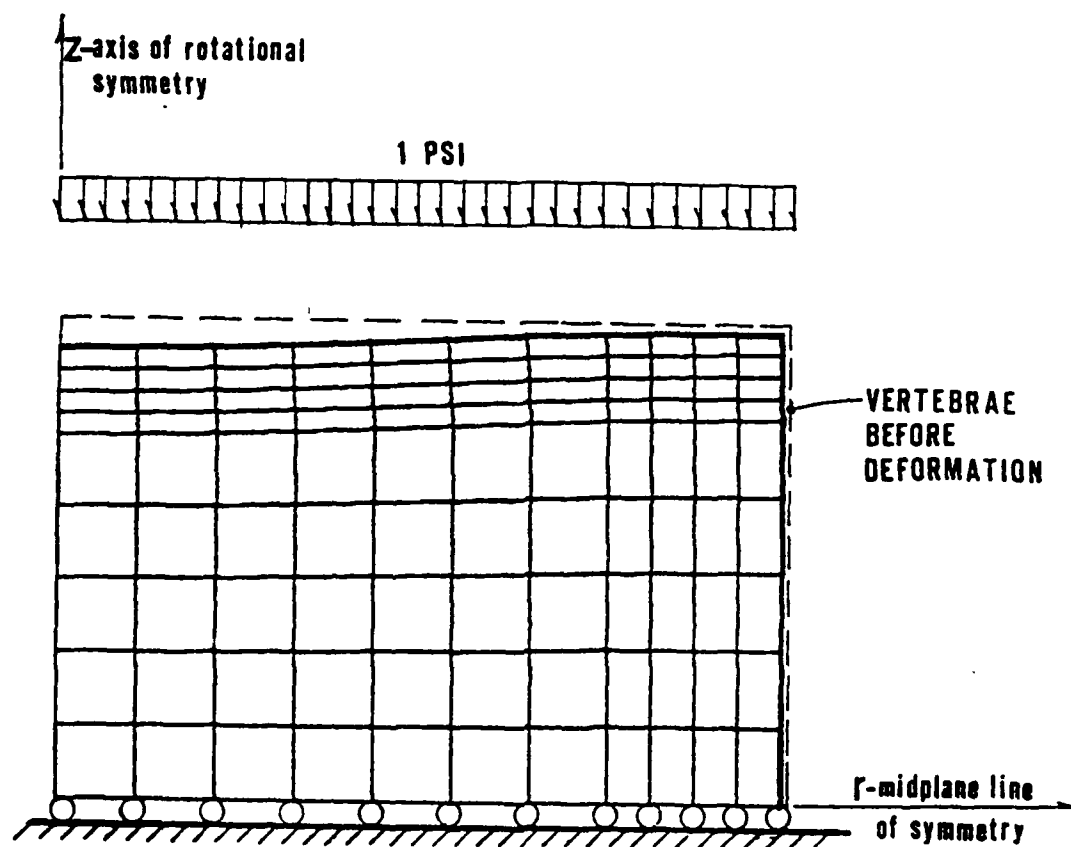


Figure 15. Deformation of lumbar vertebra subjected to axial load.

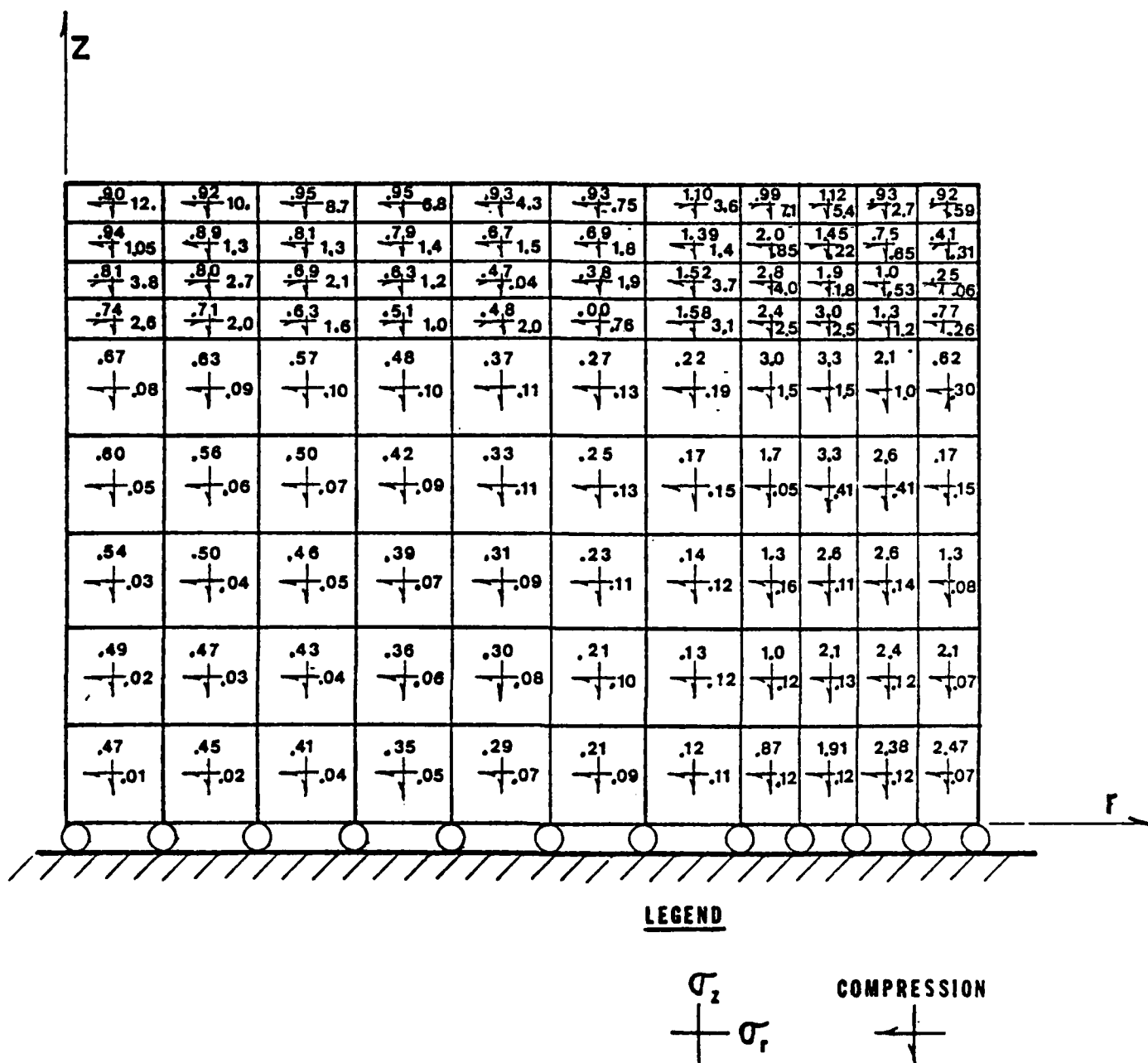


Figure 16. Trabecular bone axial and radial stress distribution of Model C (fig. 12a) under a load of 1 psi. Stresses are in units of psi.

the cortex. In this model the cortical region transmitted 7% of the applied load, which is substantially lower than the experimental results.

The radial and hoop stresses are illustrated in Figs. 16 and 17, respectively. The outermost elements of this model experience very large radial and hoop stresses. These high stresses are due to the fact that the elastic modulus of the cortical bone is up to 200 times larger than that of the trabecular bone. Even though the trabecular bone experiences higher strain than the cortical bone, the higher elastic modulus of the cortical elements yields larger stresses.

For Model S, axisymmetric shell elements were placed on the exterior of the vertebral body to determine the accuracy of these representations which include incompatible displacements. Along the outermost cylindrical part of the cortical bone, the bending stresses were very small, as illustrated in Fig. 18. In the end plates, bending stresses were in the range of 0 to 2 psi. Since there are no abrupt changes in curvature, the bending stresses are low. Since the bending stresses in the end plate and side are very small, a membrane representation of the cortical bone should yield appropriate results.

Membrane stresses in the shell elements of Model S were found to be comparable to those of the outermost elements of Model C. These stresses are illustrated in Fig. 19.

4.4 Comparison with Earlier Model

Since Plesha et al. (1980) used a cortical bone thickness of 0.012 in. and elastic modulus of 2.18×10^6 psi, the only appropriate way to compare the

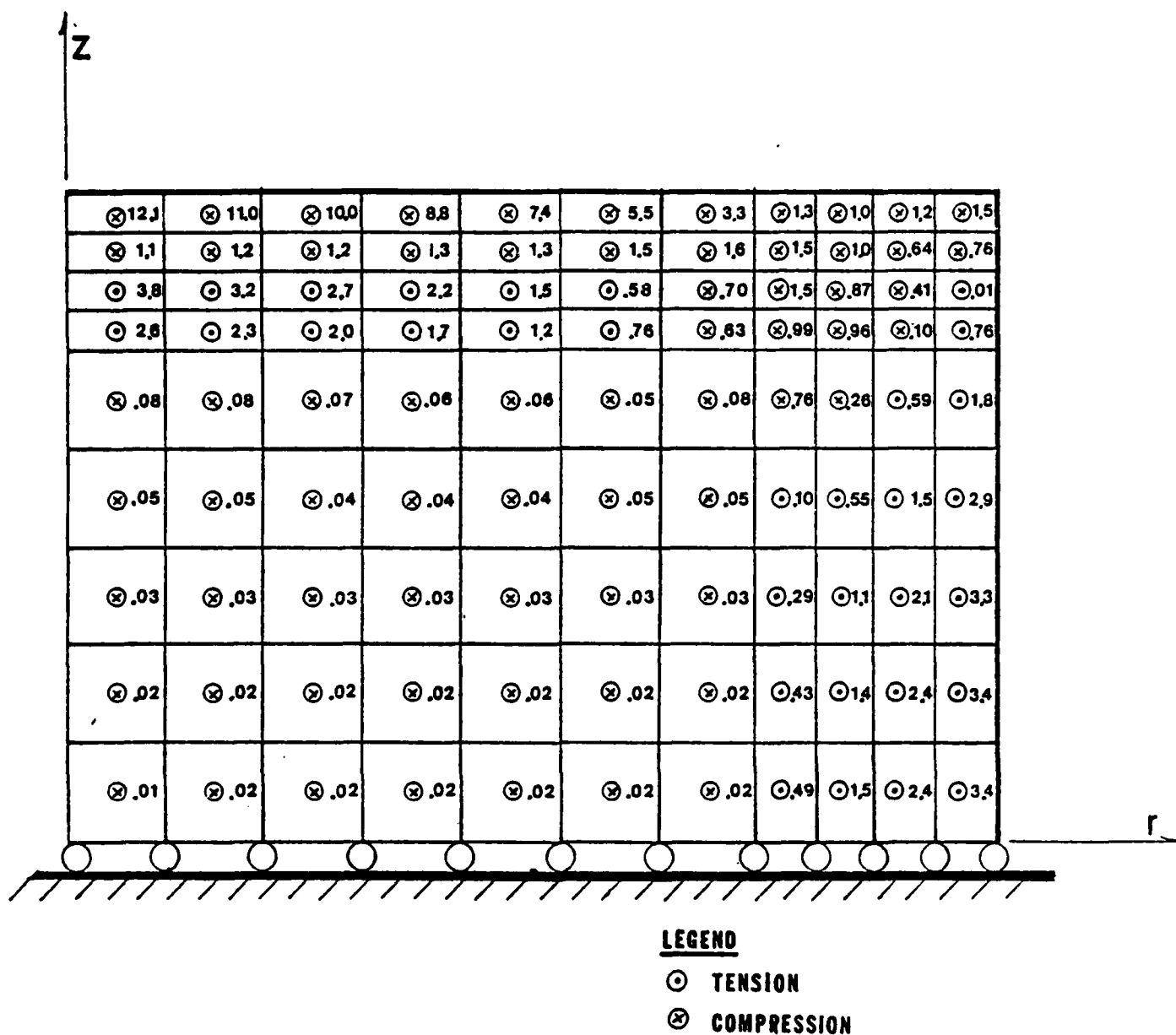


Figure 17. Hoop stress distribution in Model C (fig. 12a) under a load of 1 psi. Stresses are in units of psi.

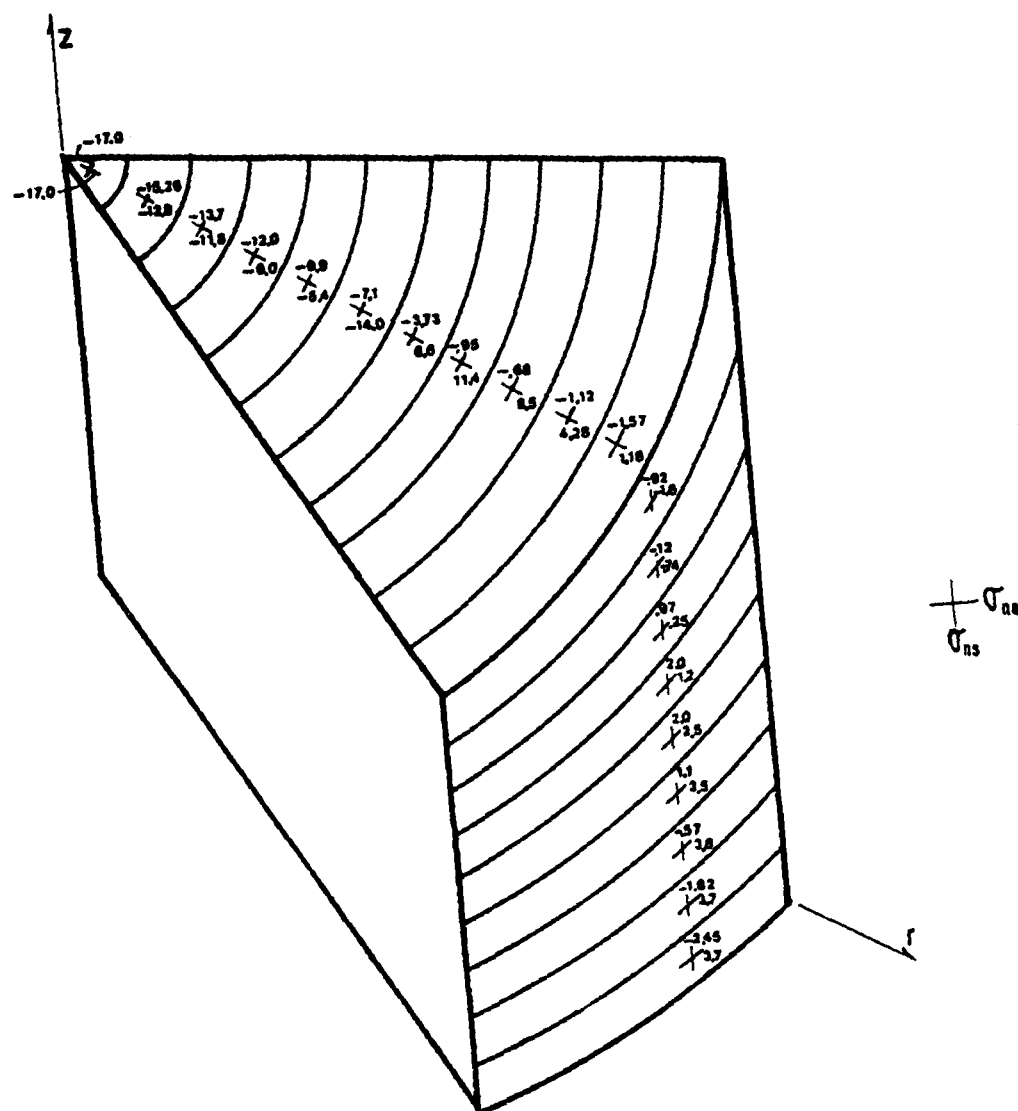


Figure 19. Cortical bone membrane stress distribution for Model S under a load of 1 psi. Stresses are in units of psi. Positive and negative values indicate tension and compression respectively on exterior surface of elements.

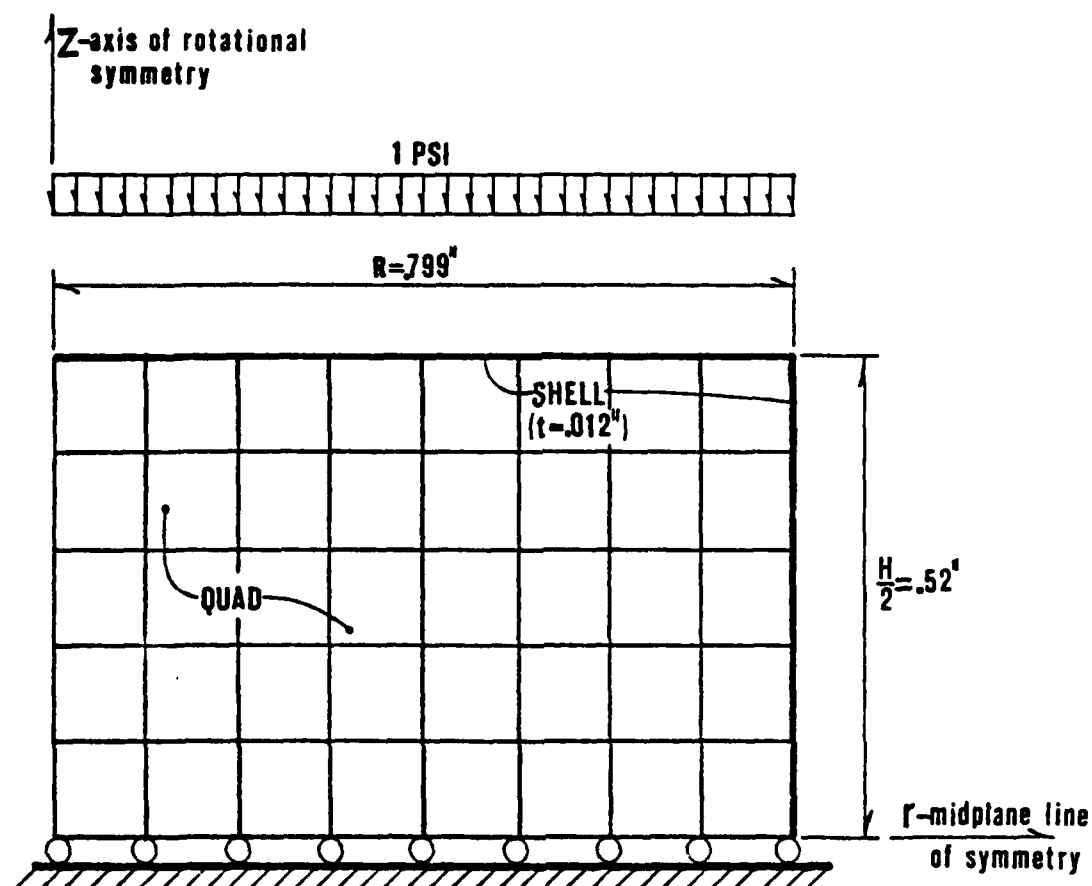
axisymmetric models with the three dimensional model is to duplicate the dimensions and material properties of Plesha's model. Model SC, which is illustrated in Fig. 20, is identical to Model S except that the material properties are discontinuous at the trabecular bone - cortical bone interface. It will be used for this comparison. It should be noted that Plesha's model represents the lumbar vertebrae as shown in Figs. 21 and 22.

The main discrepancy between the two models seems to lie in the bending stresses along the corner of the sides and end plates. Plesha reported very high bending stresses, as shown in Fig. 23. The results for Model SC are shown in Fig. 24.

In the circumferential direction, the bending stresses for Model SC should be smaller than Plesha's since the strain only depends on the displacement in the radial direction. In the vertical direction there is a significant difference in bending stresses. The reason for these high bending stresses in Plesha's model could be due to the coarseness of the finite element mesh. The model represents the smooth surface by a series of piecewise linear surfaces. Therefore, at the element interfaces, spurious moments known as "discontinuity" moments may have appeared (Ashwell et al., 1976).

4.5 Comparison with a Simplified Model

Model SC, with a cortical bone thickness of 0.012 in. will be compared to the predictions of the simplified model in Fig. 11. The cortical bone stress given by Belytschko et al. (1976) for the simplified model is



Element	Elastic Modulus
Shell	2.18×10^6 psi
Quad.	1.07×10^4 psi

Figure 20. Cortical bone membrane stress distribution for Model S under a load of 1 psi. Stresses are in units of psi. Positive and negative values indicate tension and compression respectively on exterior surface of elements.

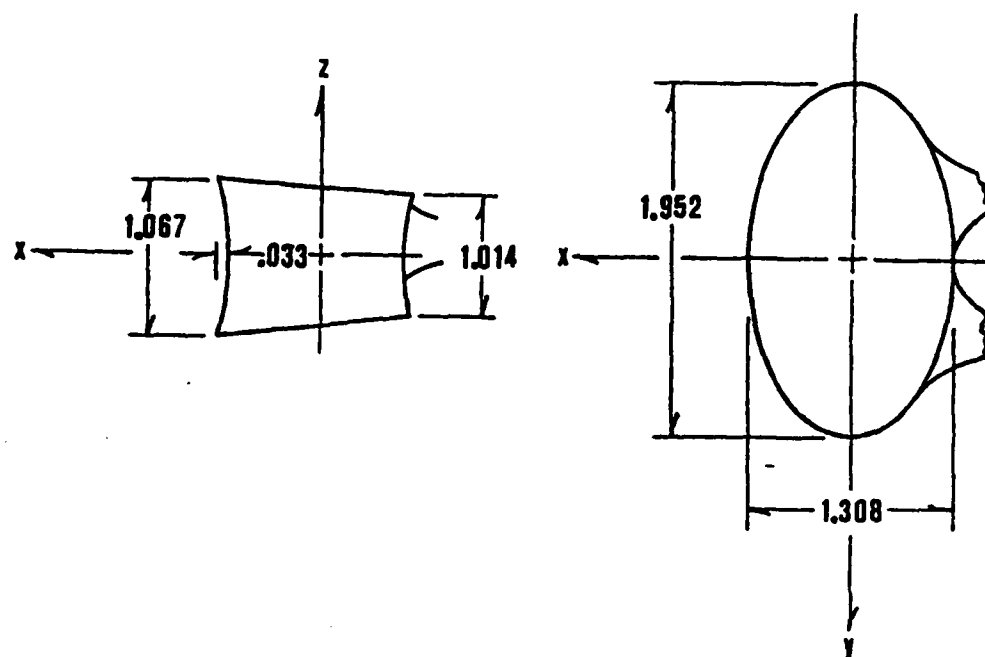


Figure 21. Side and top view of the lumbar vertebrae with dimensions.

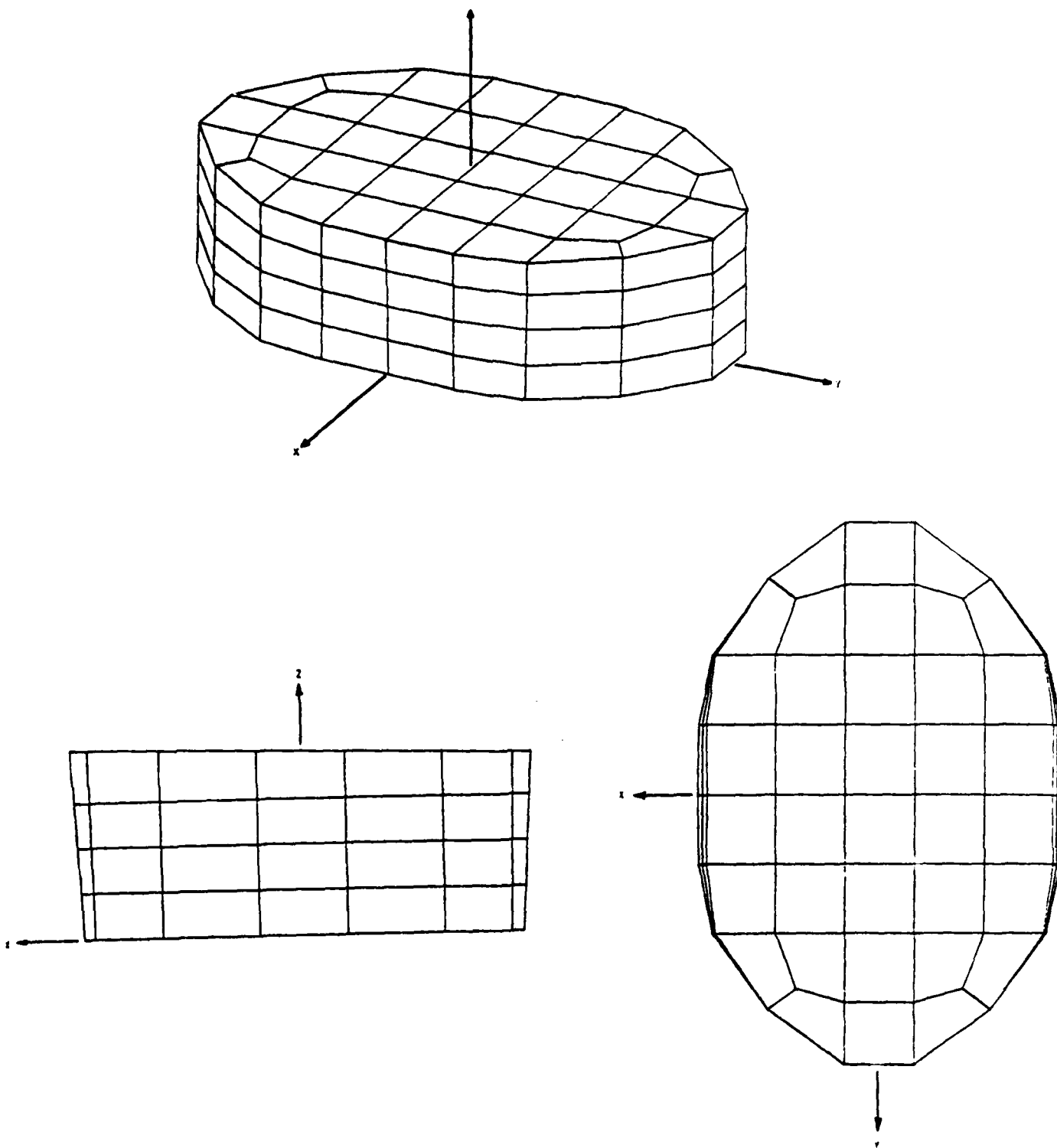


Figure 22. Plesha's three-dimensional vertebral model. Dimensions for the first lumbar vertebra illustrated in figure 21 are used.

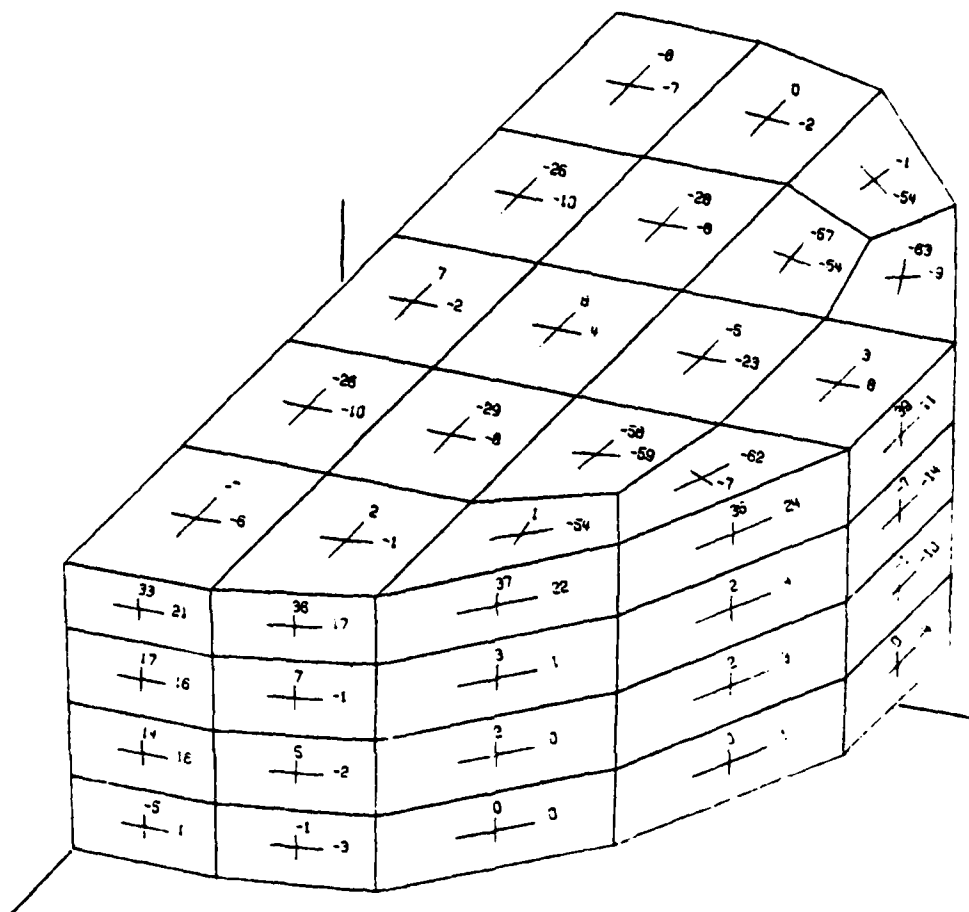


Figure 23. Plesha's model for cortical bone bending stress distribution under a load of 1 psi. Stresses are in units of psi. positive and negative values indicate tension and compression respectively on exterior surface of elements.

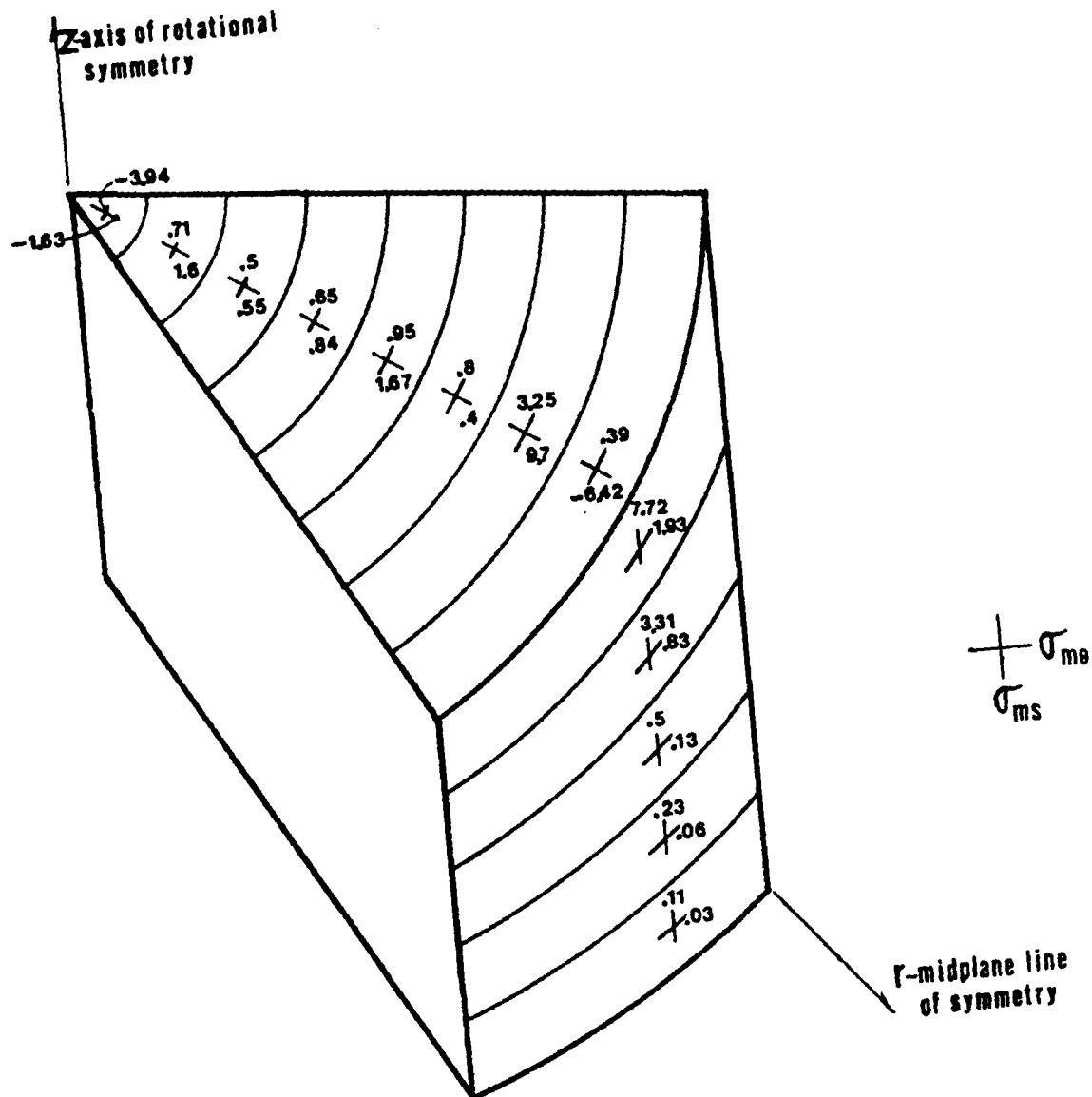
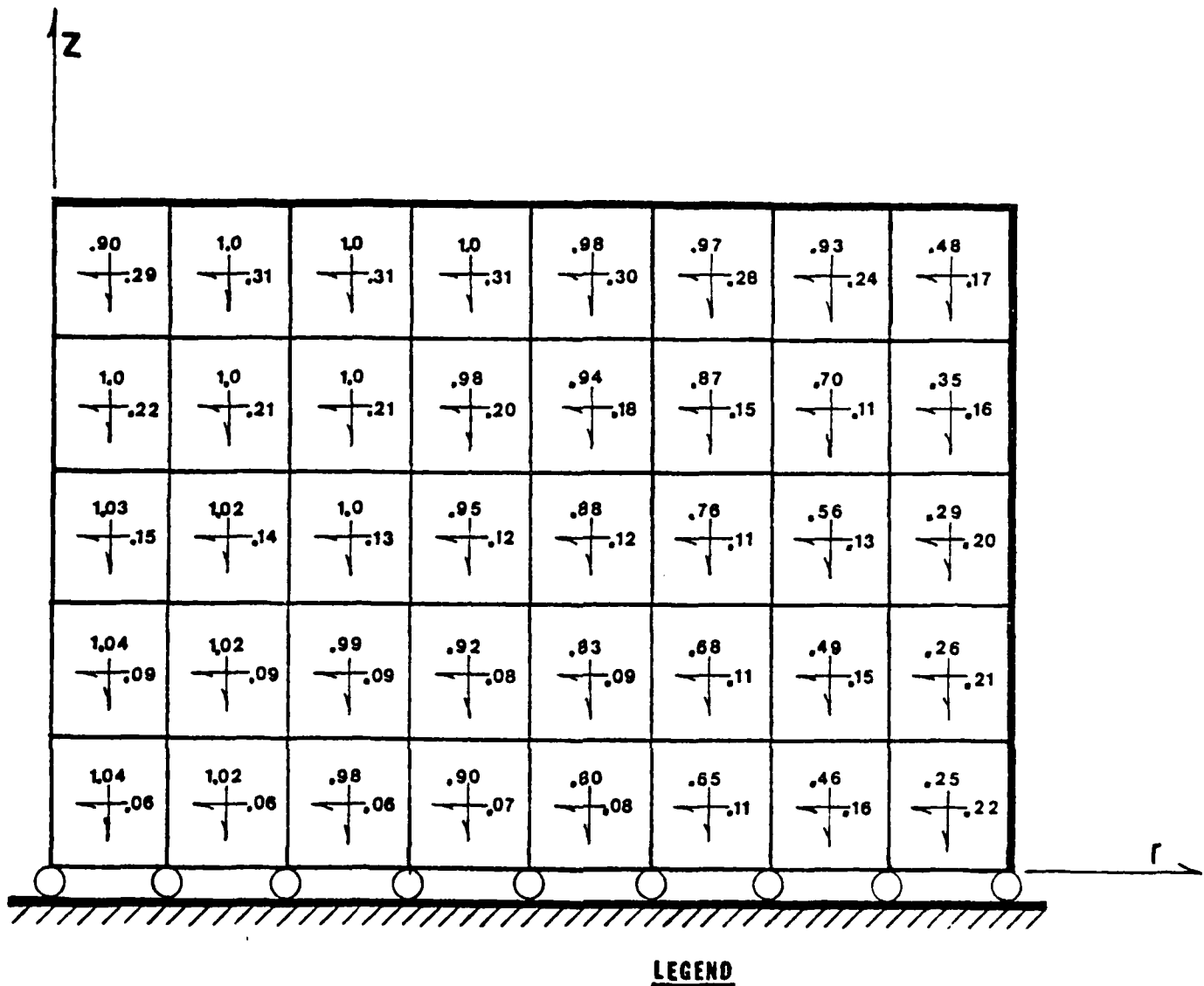


Figure 24. Cortical bone bending stress distribution for Model SC under a load of 1 psi. Stresses are in units of psi. Positive and negative values indicate tension and compression respectively on exterior surface of elements.

$$\sigma = \frac{E_o P}{\pi[E_i R_i^2 + E_o(R_o^2 - R_i^2)]} \quad (4.1)$$

where E_i and E_o are Young's moduli for the trabecular (inner) and cortical (outer) bone, respectively, and R_i and R_o are the radii as shown in Fig. 11. For $P = 2.005$ lbs., Eq. (4.1) yields a maximum stress of 28.9 psi.

The membrane stresses for the finite element analysis are illustrated in Figs. 25 and 26. The maximum axial stress predicted by Model SC was found to be less than half that predicted by Eq. (4.1). This discrepancy is due to the assumption in Eq. (4.1) that the strain in the trabecular core is the same as the strain in the cortical shell (i.e. that the end plate does not deform to a concave surface but remains flat). Also, Model SC takes into account the end plates, while the idealized model neglects their effects. In the finite element model, the strains in the trabecular bone were found to be significantly greater than those in the cortical shell, especially near the center. But since the ratio of the elastic modulus for the cortical shell compared to that of the trabecular bone is 200 to 1, the cortical shell experiences higher stresses. This is shown in Fig. 26. This can be elucidated by considering the load distribution between the trabecular and cortical bone. Equation (4.1) predicts that the cortical and trabecular bone transmit 86% and 14% of the applied load, respectively. Model SC predicts 41% and 59%, respectively. It is the uniform strain assumption inherent in Eq. (4.1) that causes it to predict higher stresses for the cortical bone. It should be noted that bending stresses are neglected in Eq. (4.1). However the bending stresses are small, so even when the bending stress is combined with the membrane stress, the values are only half of that given by Eq. (4.1).



LEGEND



Figure 25. Trabecular bone membrane stress distribution for Model SC under a load of 1 psi. Stresses are in units of psi.

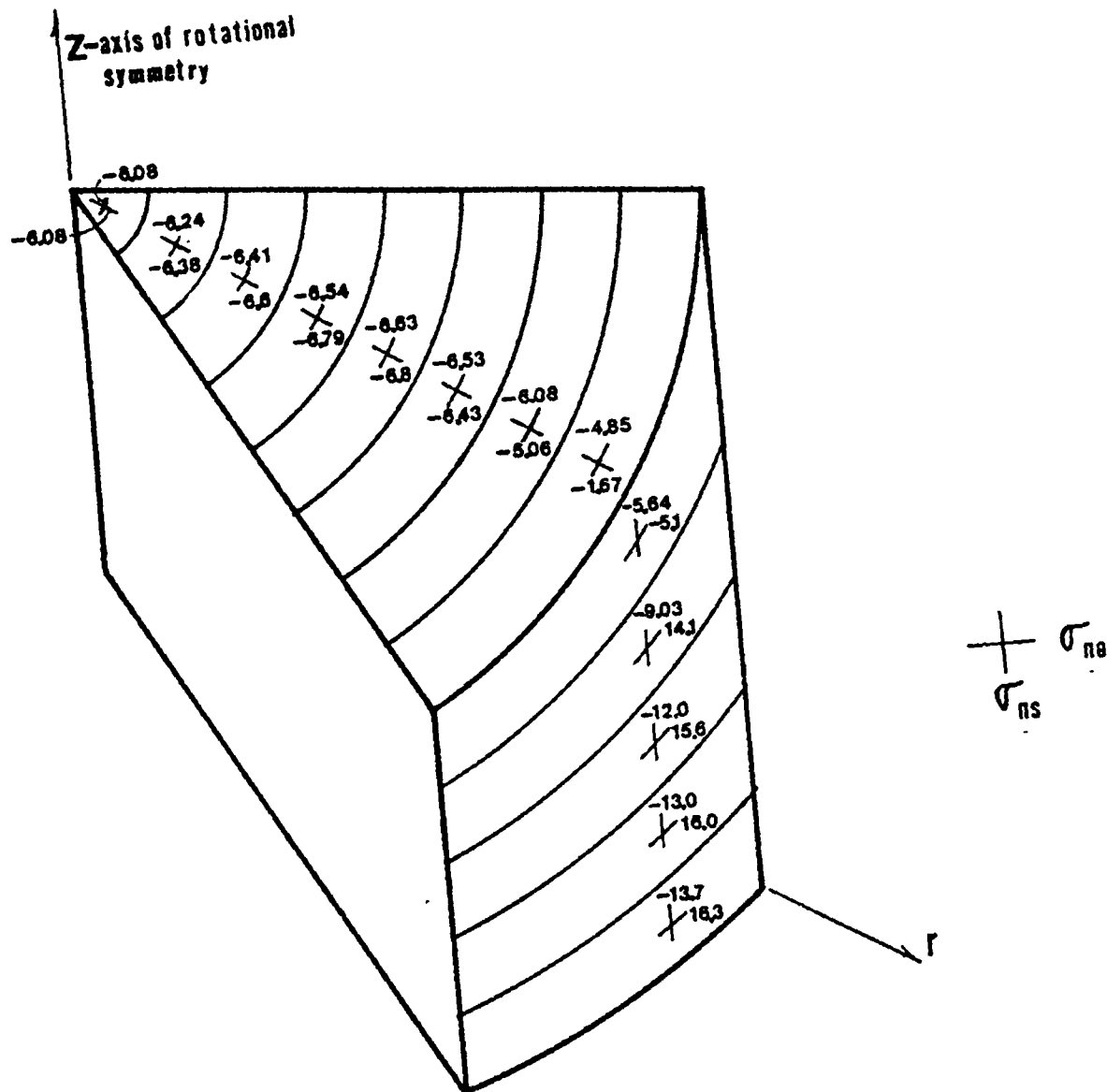


Figure 26. Cortical bone membrane stress distribution for Model SC under a load of 1 psi. Stresses are in units of psi. Positive and negative values indicate tension and compression respectively on exterior surface of elements.

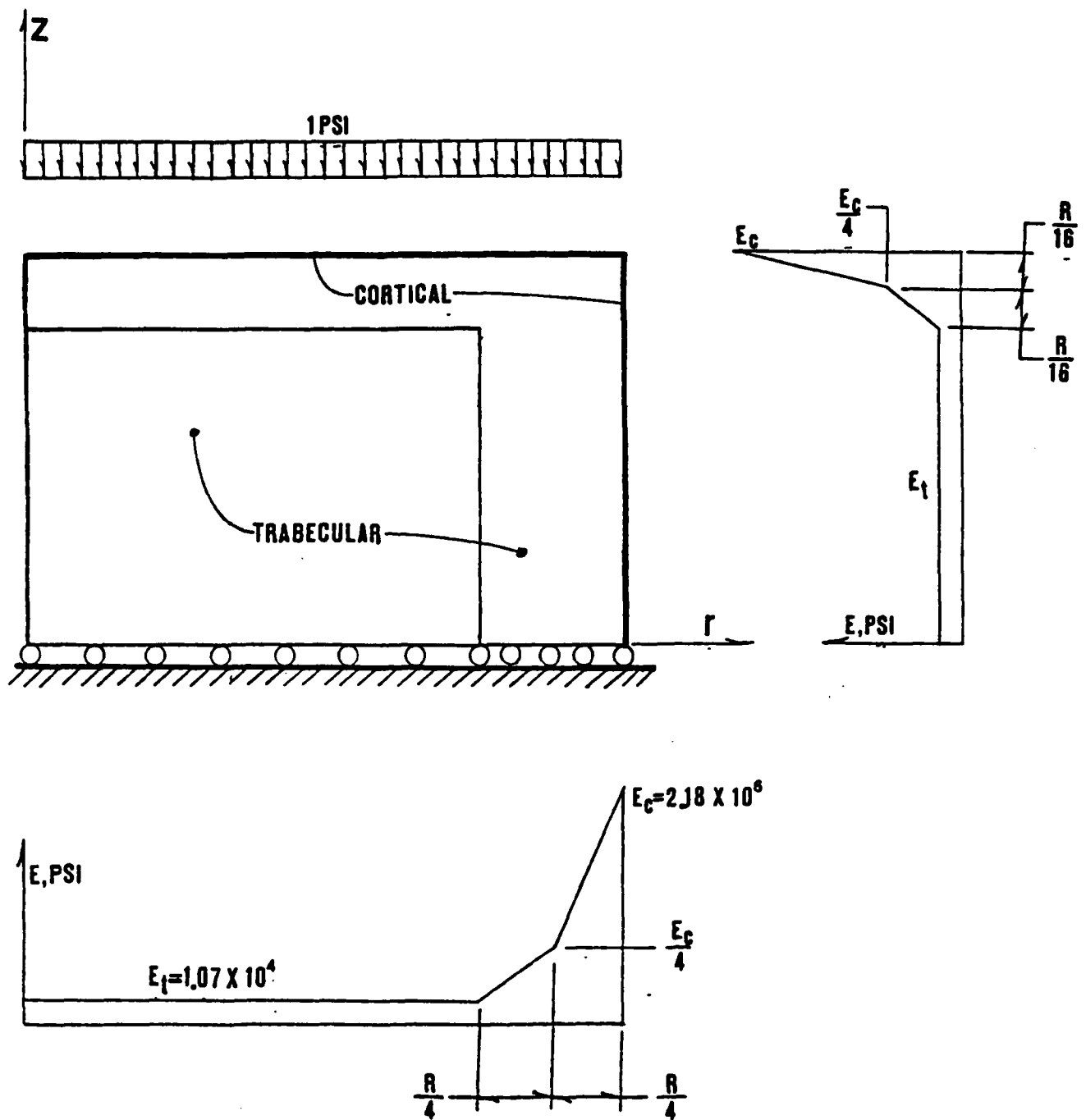
4.6 Comparison of Models S and SM

Since Model S underpredicted experimental results for the load carried by the cortical bone, the gradient of the elastic modulus was modified as shown in Fig. 27. Hence, the trabecular bone is substantially more flexible but a smooth transition of elastic modulus between cortical and trabecular bone is maintained. This model is called Model SM; it uses shell elements for the cortical bone. It was found that for this elastic modulus gradient, compared to Model S, the membrane stresses for the cortical and adjacent trabecular bone elements were reduced. The stresses of the inner trabecular elements increased as shown in Figs. 28 and 29, which give the stresses. This is expected since the deformations in this region of the mesh increased.

The maximum axial stress for Model SM was found to be 12% smaller than Model S. The axial stress distribution is shown in Fig. 28. For Model SM, the cortical bone transmitted 24% of the axial load while Model S predicted 7%. Hence, the load carried by the cortical shell of Model SM is in better agreement with the experimental results.

For Model SM, the maximum hoop and radial stresses were found to be 6% smaller than Model S. The radial and hoop stress profile are shown in Figs. 28 -30.

The bending stresses in the cortical shell were still found to be insignificant, as illustrated in Fig. 31. Therefore, the decrease in the trabecular bone stiffness, which results from increasing the magnitude of the gradient, does not introduce significant bending stresses but does increase the fraction of load carried by the cortical bone.



Note: Dimensions similar to Fig. 12b.

Figure 27. Variation of elastic modulus through Model SM.

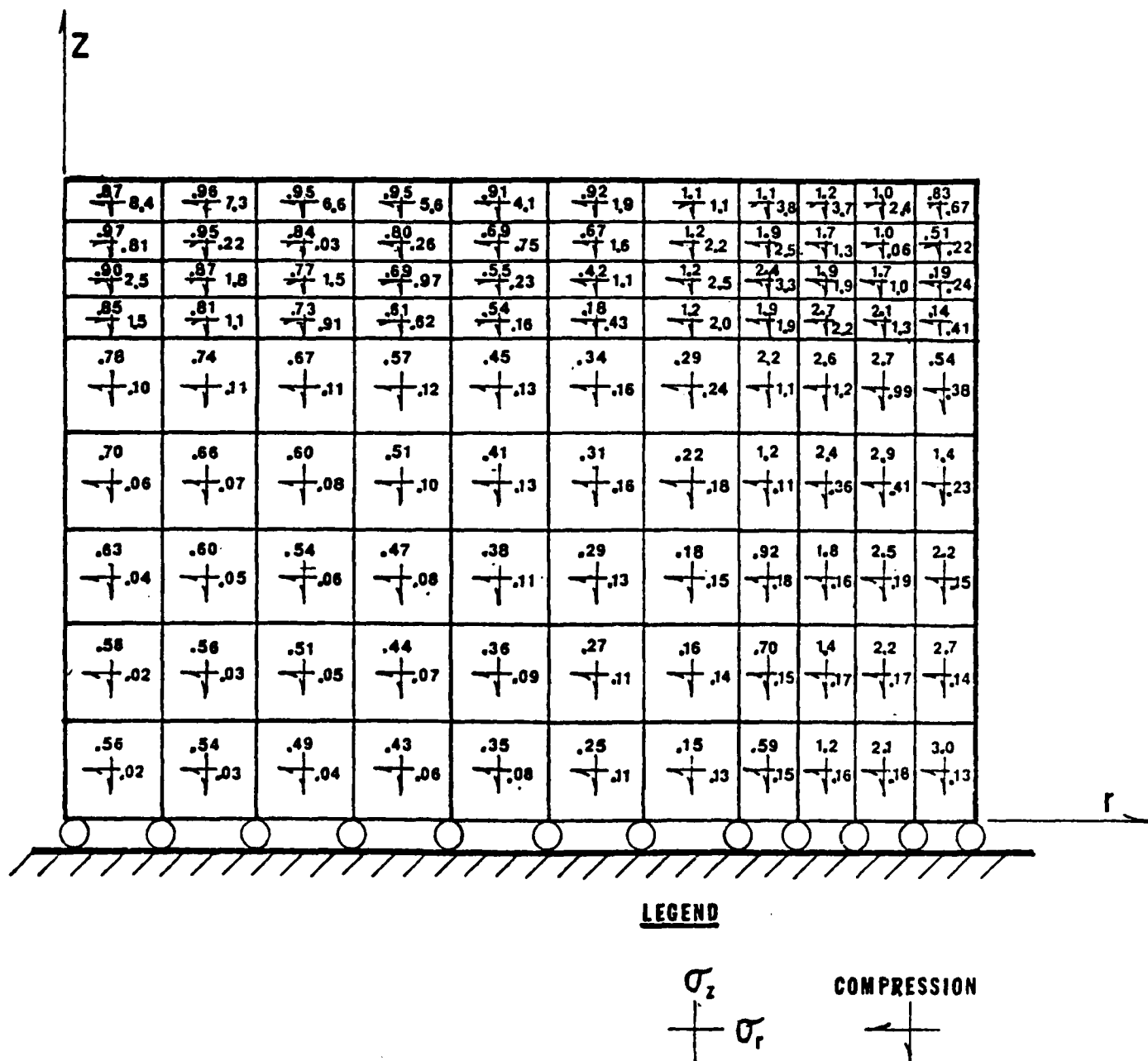


Figure 28. Trabecular bone axial and radial stress distribution of Model SM under a load of 1 psi. Stresses are in units of psi.

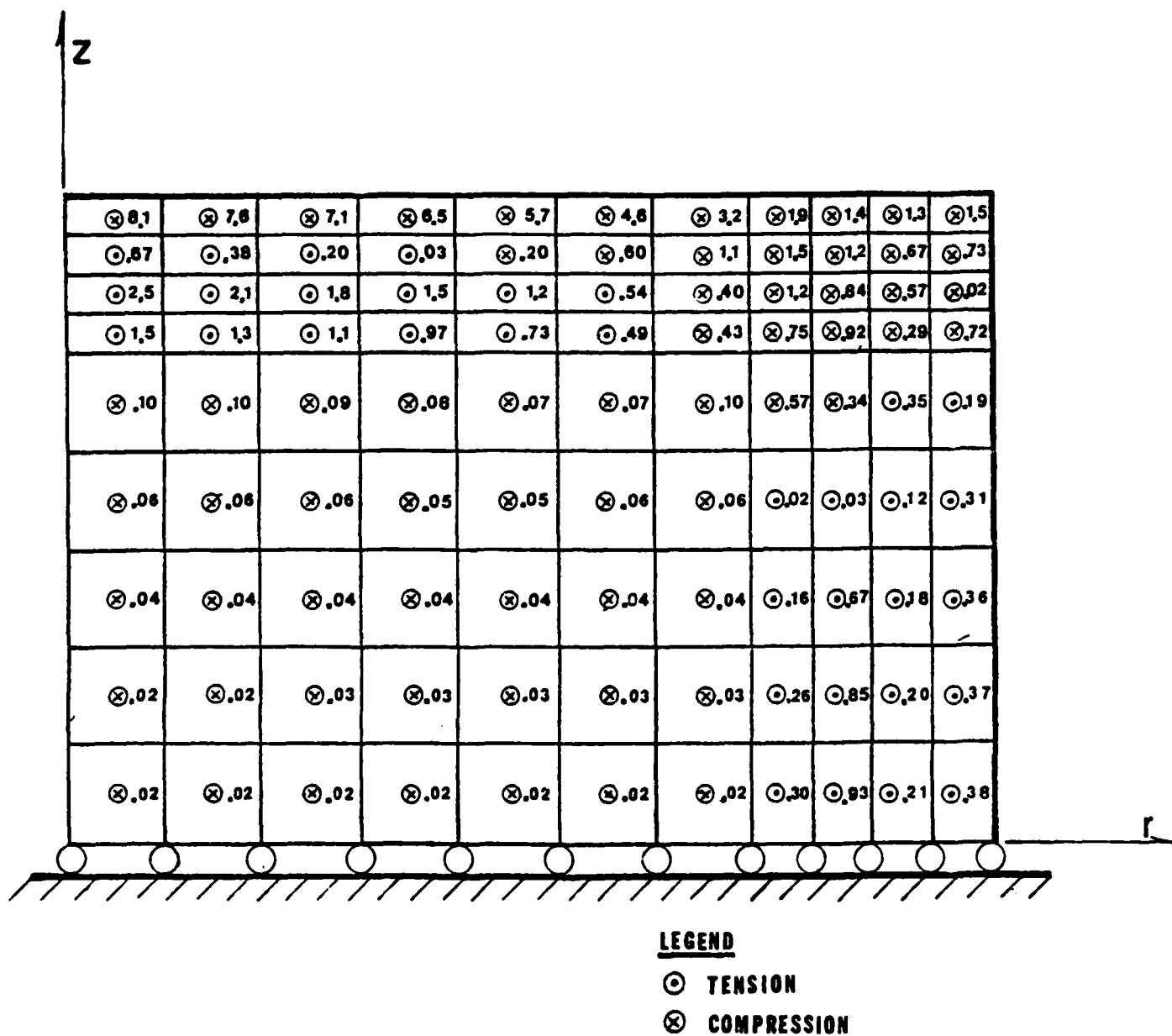


Figure 29. Trabecular bone hoop stress distribution of Model SM under a load of 1 psi. Stresses are in units of psi.

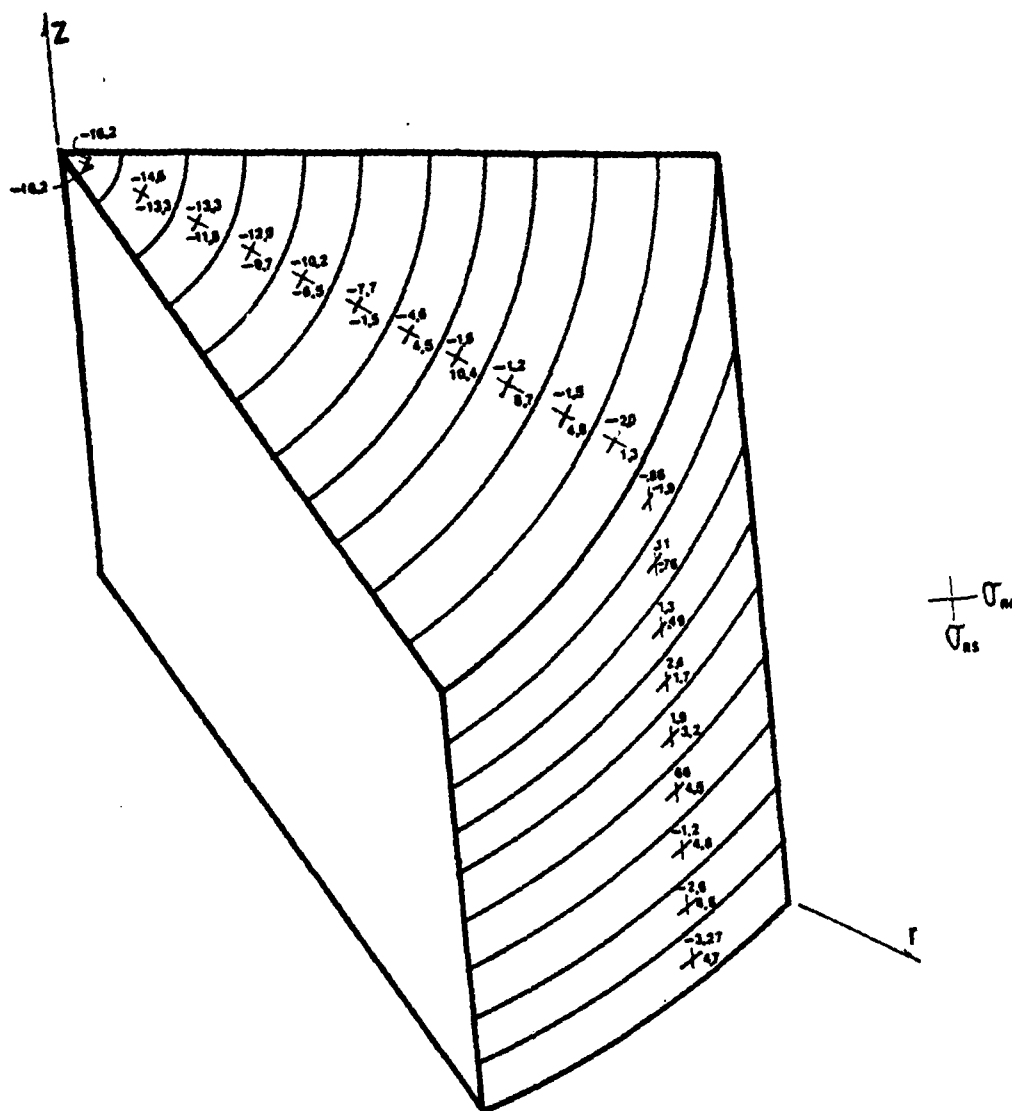


Figure 30. Cortical bone membrane stress distribution for Model SM under a load of 1 psi. Stresses are in units of psi. Positive and negative values indicate tension and compression respectively on exterior surface of elements.

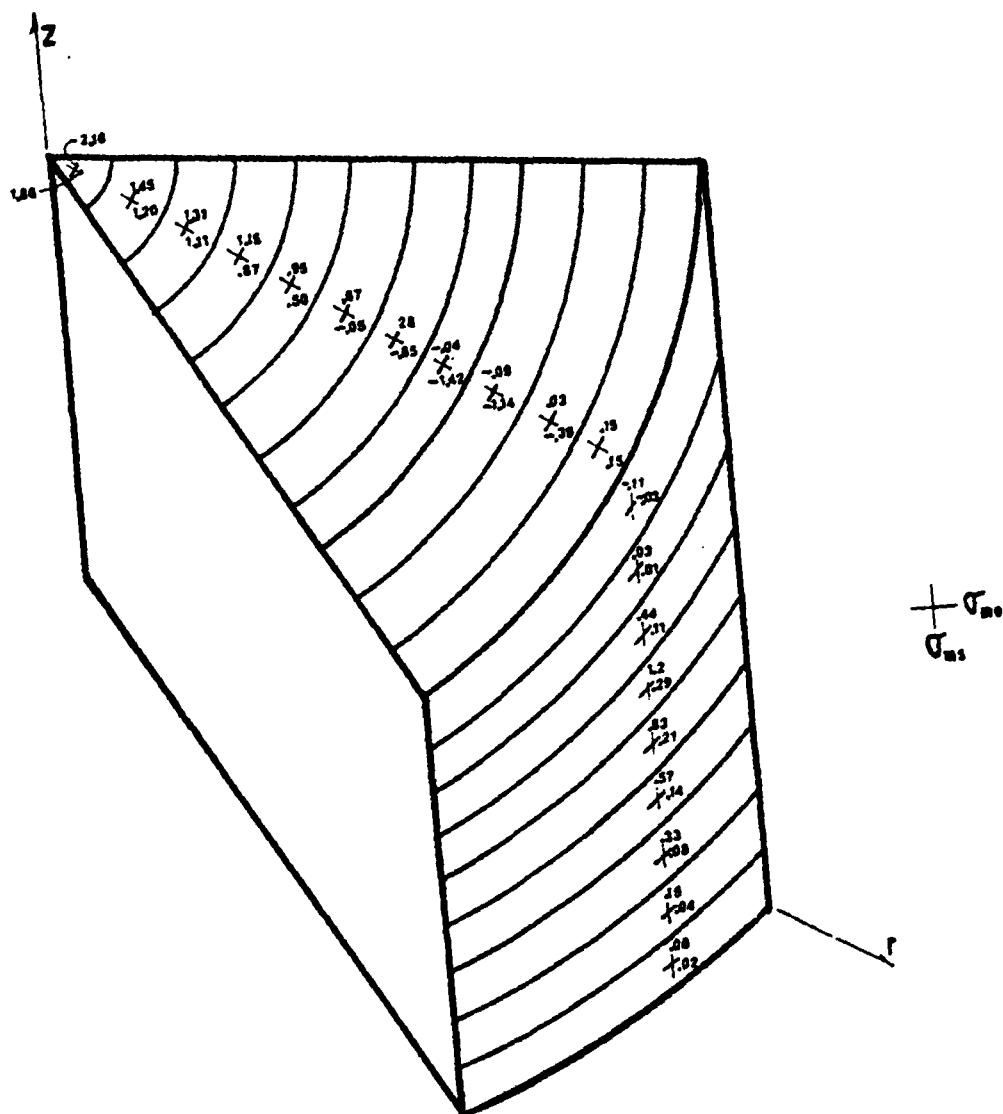


Figure 31. Cortical bone bending stress distribution for Model SM under a load of 1 psi. Stresses are in units of psi. Positive and negative values indicate tension and compression respectively on exterior surface of elements.

4.7 Comparison of Various Finite Element Models

To study the accuracy of the shell representation, a finite element model using four layers of axisymmetric quadrilaterals (Model QC) instead of axisymmetric shell elements (Model SC) for the cortical bone, was considered. The membrane stresses for Model QC were found to be comparable to Model SC as illustrated in Figs. 32 and 33. The deflection near the center of Model QC was found to be more than 6% larger than Model SC. The larger displacement is due to the fact that when four layers of quadrilaterals are used to represent the cortical shell, they possess less bending stiffness than the shell elements.

The maximum axial stress which occurs in the cortical bone, predicted by Models SC and QC was found to be more than four times larger than Models C and S. This is due to the fact that the cortical region for Models SC and QC is more flexible than Models C and S. The axial stress distribution at the midplane for all of these models and the idealized model is illustrated in Fig. 34.

More important, Model SC develops bending stresses six times larger than Model S. This is due to the discontinuity in the elastic modulus at the interface between the cortical and trabecular bone in Model SC, where Model S assumes a gradient in the elastic modulus.

Finite element analyses of a lumbar vertebra were performed to gain a better understanding of the stress distribution due to axial compression. The finite element model assumed isotropic, linearly elastic material behavior. Analyses were conducted in which the cortical bone was represented by (1) a shell elements and (2) four layers of quadrilateral elements. In addition, in the latter a gradient was introduced in the trabecular bone modulus to

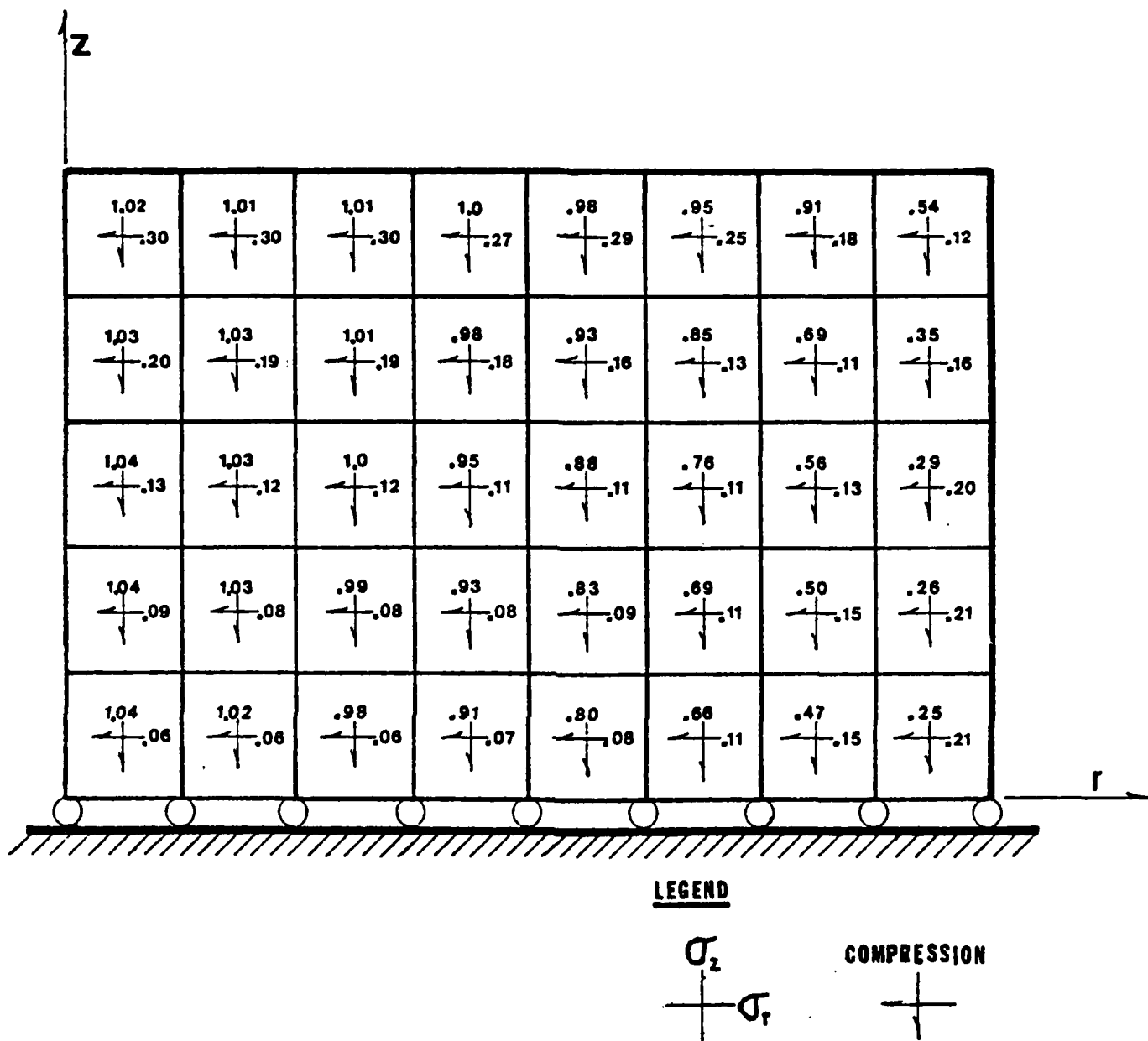


Figure 32. Trabecular membrane stress distribution for Model QC under a load of 1 psi. Stresses are in units of psi.

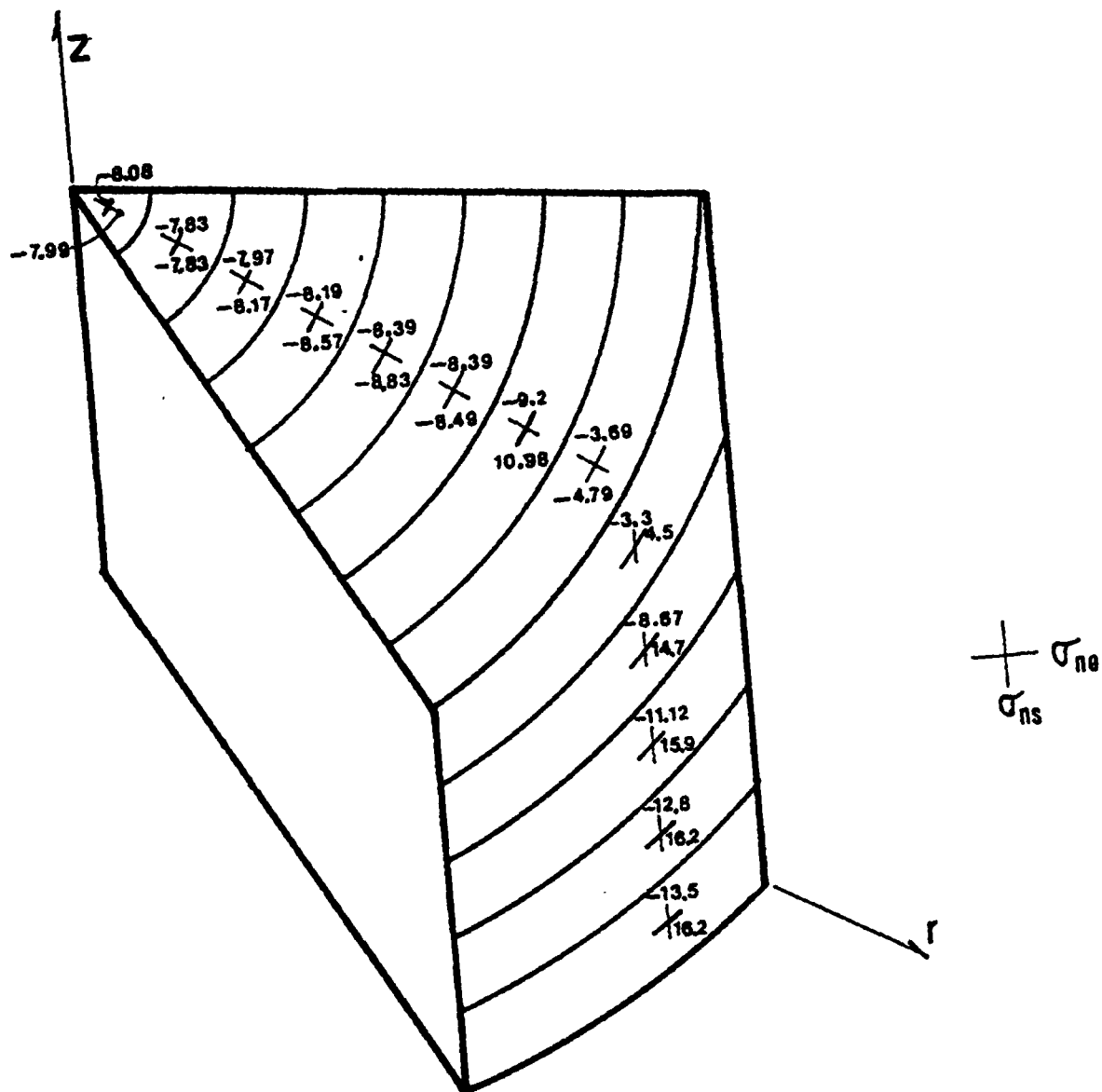


Figure 33. Cortical membrane stress distribution for Model QC under a load of 1 psi. Stresses are in units of psi. Positive and negative values indicate tension and compression respectively on exterior surface of elements.

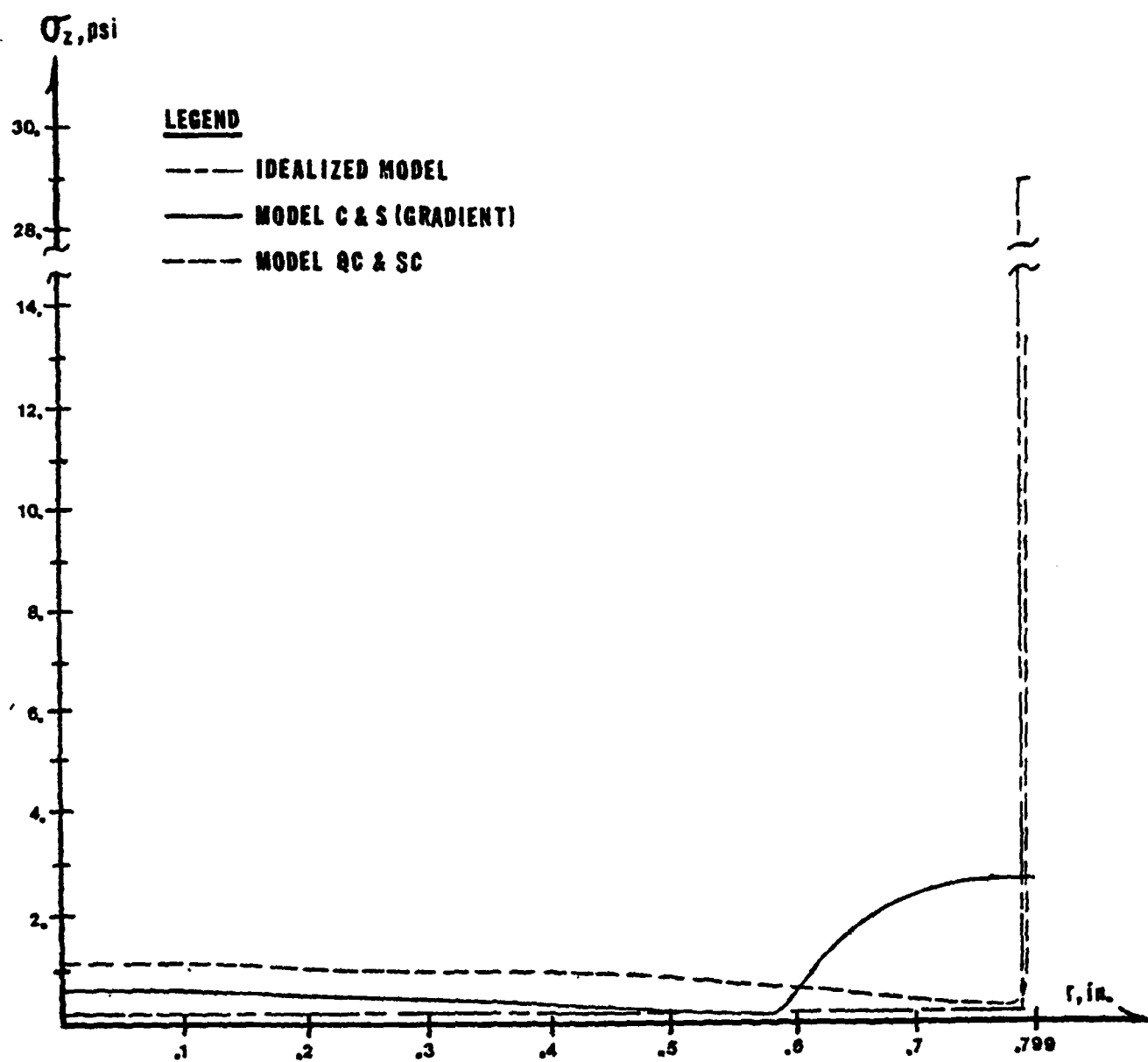


Figure 34. Axial stress distribution at the midplane of various models.

determine its effect on bending stresses in the cortical bone. These analyses resulted in substantially smaller bending stresses than those predicted by the Plesha and Belytschko (1980) model. The high bending stresses in the Plesha and Belytschko model were, most likely, an anomaly resulting from the use of the flat shell elements to approximate the actual curved surface.

SECTION V

HEAD-NECK SIMULATION RESULTS

The objectives of the simulation studies reported here are:

- a) to validate the neck model by comparing the results to experimental data for $-G_x$ and $+G_y$ impact acceleration;
- b) to study the effects of the stretch reflex response on the motion of the head and neck and on the stress levels in the neck.

To accomplish the first objective, several simulations of $-G_x$ and $+G_y$ impact acceleration were made. The predicted kinematic responses are compared to the experimental results of Ewing and Thomas (1972), who conducted vehicular acceleration tests on fully instrumented volunteers for $-G_x$ impact acceleration; and Ewing et al. (1978) who did similar tests for the $+G_y$ impact response. The purpose of both of these experimental studies was to measure not only the dynamic response of the head and neck but also the complete input acceleration to the head and neck at the first thoracic vertebra. It is necessary to measure the input acceleration to the neck directly because the true input to the neck can be quite different from the sled acceleration due to the restraints used, the coupling of the man to the vehicle and the dynamic response of the subject below the neck.

The second objective is to examine the main difference between the behavior of the neck model with passive muscles and with contracting muscles. Since living subjects automatically resist motion of the head and neck during impact after about 40 to 100 msec, the response is different from that of cadavers or dummies which cannot resist motion by contracting muscles. The living subject is modeled by using muscles which start contracting 40 to 100

msec after impact, whereas the cadaver or dummy is modeled by using muscles which remain passive throughout each simulation run. A comparison of these results may be of interest to experimentalists concerned with the validity of using crash dummies or cadavers as substitutes for living subjects.

The results of the $-G_x$ impact simulations are reported first, followed by the results of the $+G_y$ impact simulations.

5.1 $-G_x$ Impact Simulation

In the tests conducted by Ewing and Thomas (1972) seated subjects were exposed to $-G_x$ impact accelerations ranging from 3G to 10G in magnitude. Displacements were obtained by double integration with respect to time of the accelerations measured at the head and T1 by accelerometers; these were rigidly mounted on the man in completely reproducible locations, with relationships to the bony anatomy measured by X-ray anthropometry. A second and independent method of measuring the displacements was used simultaneously as a check on the transducer-derived data. This was accomplished by using sled-mounted, high-speed, high precision 16 mm cine cameras. The displacements of T1 were subtracted from those of the head displacements which were thus reported with respect to T1.

The acceleration device imparted the experimental pulse at the acceleration end so that the subject was at rest at the start of the experiment. The restraint system consisted of a steel seat with a modified A-1 aircraft lap belt and shoulder harness with an inverted V and a chest safety strap. No chin-chest impact was reported for any of the $-G_x$ tests conducted by Ewing and Thomas, and the head and neck were unrestrained in all experiments.

In order to isolate possible deficiencies in the modeling of the head-neck system it was decided to run a series of simulations with the neck and head alone by using T1 as the base of the model. Possible inadequacies in the lower spine model and in the restraint system employed were then prevented from biasing the head and neck results. The functions of the musculature in resisting head and neck motion are also more easily studied using the isolated head-neck system. After satisfactory head and neck results were obtained and confidence in the model was established, simulations were done using whole-body modeling by including a simplified representation of the lower spine.

Although Ewing and Thomas (1972) measured the accelerations at T1 they did not report T1 acceleration in their monograph but instead provided data only on T1 angular displacement. For this reason the acceleration at T1 was assumed to be equivalent to the sled acceleration and this was used as the driving function for the isolated neck model with T1 as the base. This assumption was then checked by running $-G_x$ simulations with the lower spine included. In the whole body simulations the driving functions at the base of the model (pelvis) was equal to the experimental sled acceleration profile.

The test used for comparison with our $-G_x$ simulation is one in which a maximum sled acceleration of -7.4 G was attained. The sled acceleration in this test increases linearly from zero to its maximum at 14.2 msec, followed by a linear decay to zero at 340 msec. This triangular sled acceleration profile was prescribed in the program by using the following displacement function at the base of the model:

$$u_x(t) = \begin{cases} -85680.75 t^3, & 0 < t < 0.0142 \text{ sec} \\ 11203.19 \left[\frac{t^3}{3} - 0.34 t^2 + 0.004828t - 2.2853 \times 10^{-5} \right], & 0.0142 < t < 0.034 \text{ sec} \end{cases}$$

The simulations were run for 200 msec with a time step of 10^{-4} seconds, requiring 2000 time steps.

In all of the $-G_x$ simulations described next the facets were represented by the structural arrangement of springs described in Williams (1981). When the facet elements were later developed during $+G_y$ impact modeling, one of the $-G_x$ simulations was repeated using the facet elements instead of the arrangements of springs. No significant difference was observed in the results. All experimental angular results were reported with respect to the head anatomical coordinate system as defined by Ewing and Thomas (1972); the origin of the head anatomical coordinate system is 1.33 cm behind and 2.09 cm below the average head center of gravity. The calculated angular variables in the simulations are reported with respect to the body coordinate system $(\bar{x}, \bar{y}, \bar{z})$ of the head; the origin of the model's body coordinate system is at the head center of gravity. In both coordinate systems the \bar{x} -axis goes through the front of the head and the \bar{y} -axis through the left ear.

5.2 $-G_x$ Simulations with the Head-Neck Model Isolated from the Lower Spine

In all the simulations with the isolated neck model T1 is constrained from rotation and from lateral and vertical translation. The X-displacement function describing the sled motion is prescribed at T1. Three series of tests were made with the isolated head-neck model. In the first, the muscles

were excluded; in the second, the muscles were passive throughout the simulation; and in the third, the extensor muscles of the head and neck started to contract at 60 msec and continued to contract until the end of the simulation at 200 msec.

Ligamentous head-neck model

Preliminary tests were performed without the muscle elements in the early stages of constructing the head-neck model. Figure 35 shows the deformed spine plot for the ligamentous neck. This model included representations of the discs, ligaments and facets. A major difficulty in these early tests was that sharp angulations would develop in the spine at about 150 msec because of large rotations of the beam elements representing the intervertebral discs. The solution to this problem was not immediately apparent since it was, at first, mistakenly assumed that the problem might be corrected by incorporating the musculature to reduce the excessive rotations of the beam elements. The problem was finally prevented by increasing the bending stiffnesses of the discs in the sagittal plane, so that they equalled the bending stiffnesses in the frontal plane. This was justified by the experimental data of Markolf (1972) on disc stiffnesses which indicated that the bending stiffnesses in both planes are almost equal. In the earlier model bending stiffnesses in the sagittal plane were 25% to 50% of the bending stiffnesses in the frontal plane, as estimated from strength of materials formulas and disc geometry.

Figures 36 and 37 show the computed head global Z-displacement and angular displacement, respectively, in comparison with the experimentally measured values. The predicted displacements are up to twice the experimental values, which is not surprising since the musculature was not included.

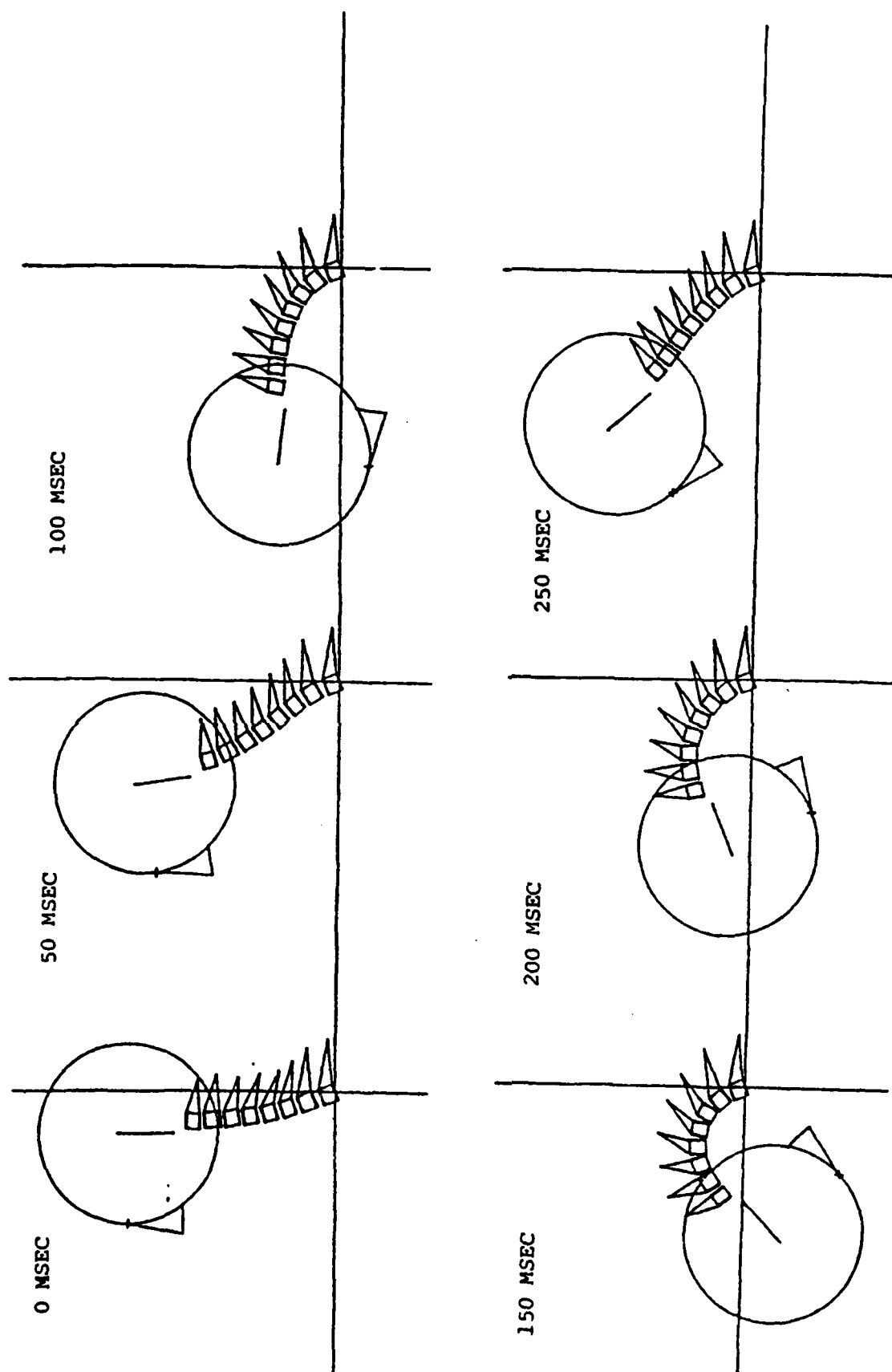


Figure 35. Response of isolated ligamentous head-neck model to $-G_x$ impact acceleration.

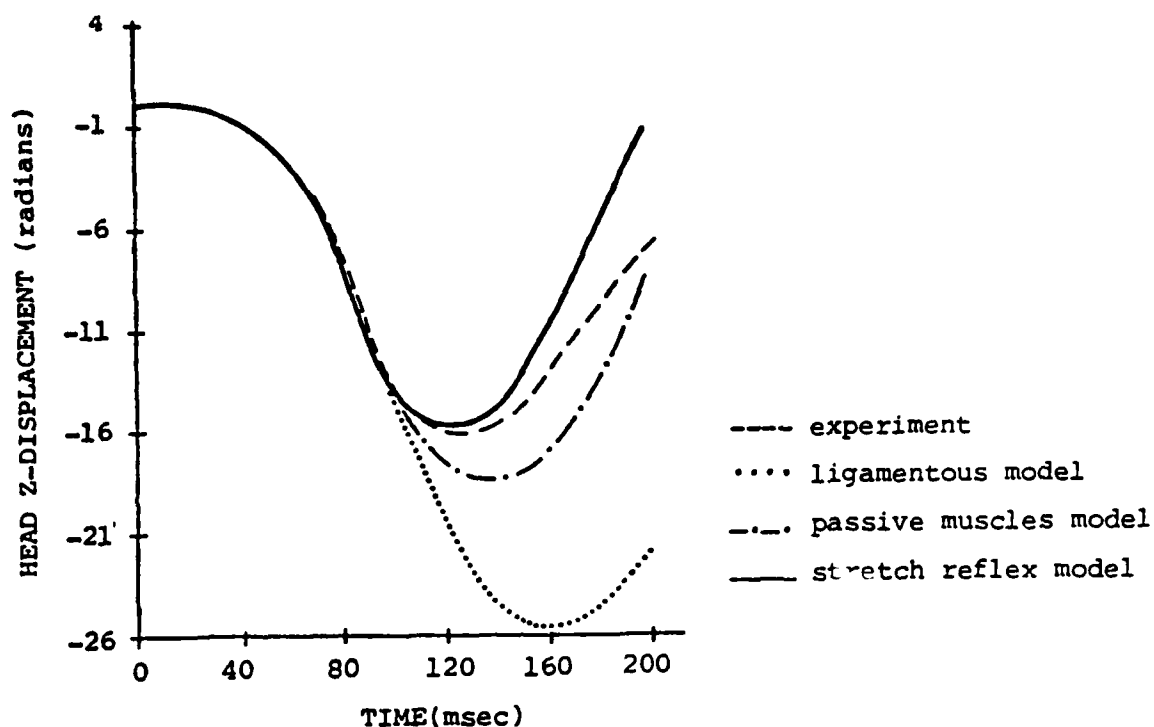


Figure 36. Head Z displacement with respect to T1 during $-G_x$ impact acceleration.

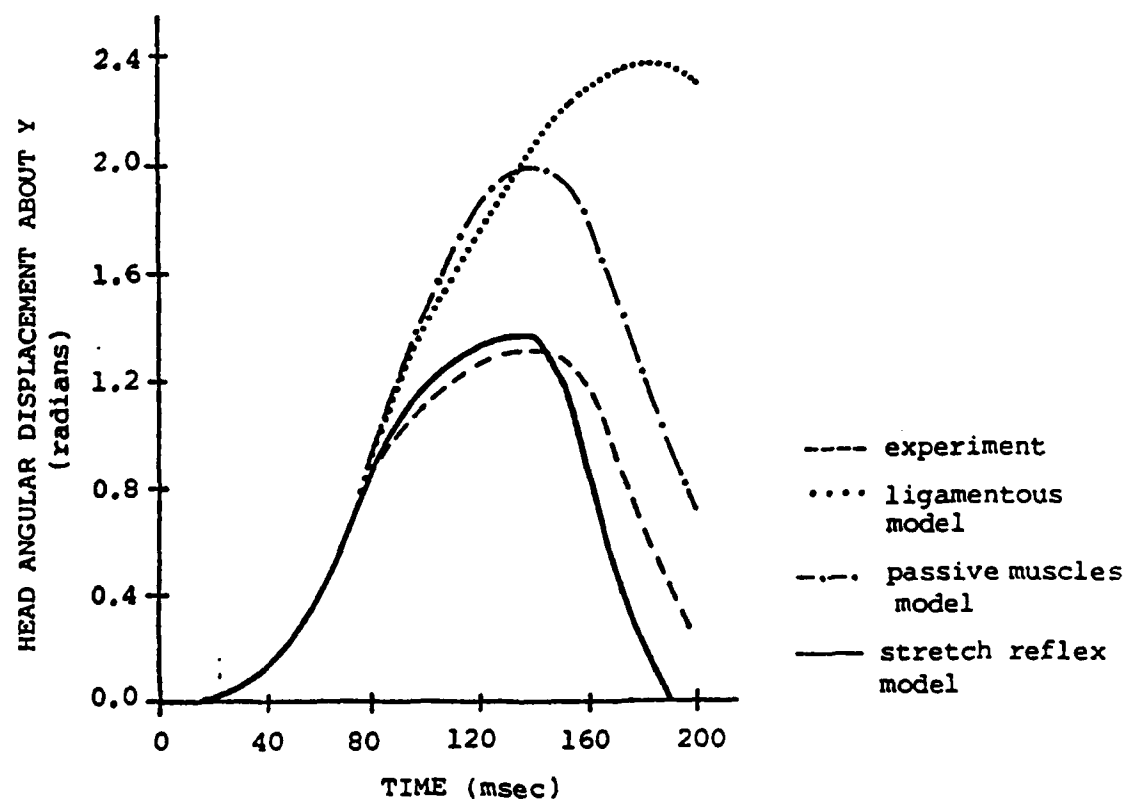


Figure 37. Head angular displacement with respect to T1 during $-G_x$ impact acceleration.

Head-neck model with musculature

When the muscles were at first included in the model, as passive elements, the resulting kinematic response was virtually identical to the ligamentous neck run. The only difference was that the muscles caused the model to become unstable at about 175 msec due to incorrect modeling of the line of action of the muscles. After incorporation of intermediate sliding nodes the results improved dramatically.

Up to 118 muscle elements were included to represent 22 of the major muscle groups in the neck, some of which have left and right counterparts; the ligaments were modeled by nonlinear springs as described in Williams (1981). The behavior of a cadaver during $-G_x$ impact was simulated by using muscle elements which remained passive throughout the 200 msec simulation. In living subjects the stretch reflex response is evoked at about 50 msec after the start of impact. To model this, the extensor muscles of the neck were allowed to contract at 60 msec during the simulation run. This was done by setting the $S(t)$ function equal to 100 at $t = 60$ msec. This is an external means of modeling the stretch reflex response: a predetermined set of muscles is stimulated to contract by setting $S(t)$ to a non-zero value at 60 msec. In future models an even more realistic approach could be taken by using the strain or strain rate of the muscle as a criterion for deciding which muscles should be stimulated to contract at what time. This would be a first step towards the incorporation of physiological controls.

The computed results using passive muscles and using muscles with stretch reflex response are shown in Figures 36 through 41. The deformed spine plots are compared in Figures 38a/b. It is seen that inclusion of passive muscles prevents the head from undergoing the extremely large rotation and

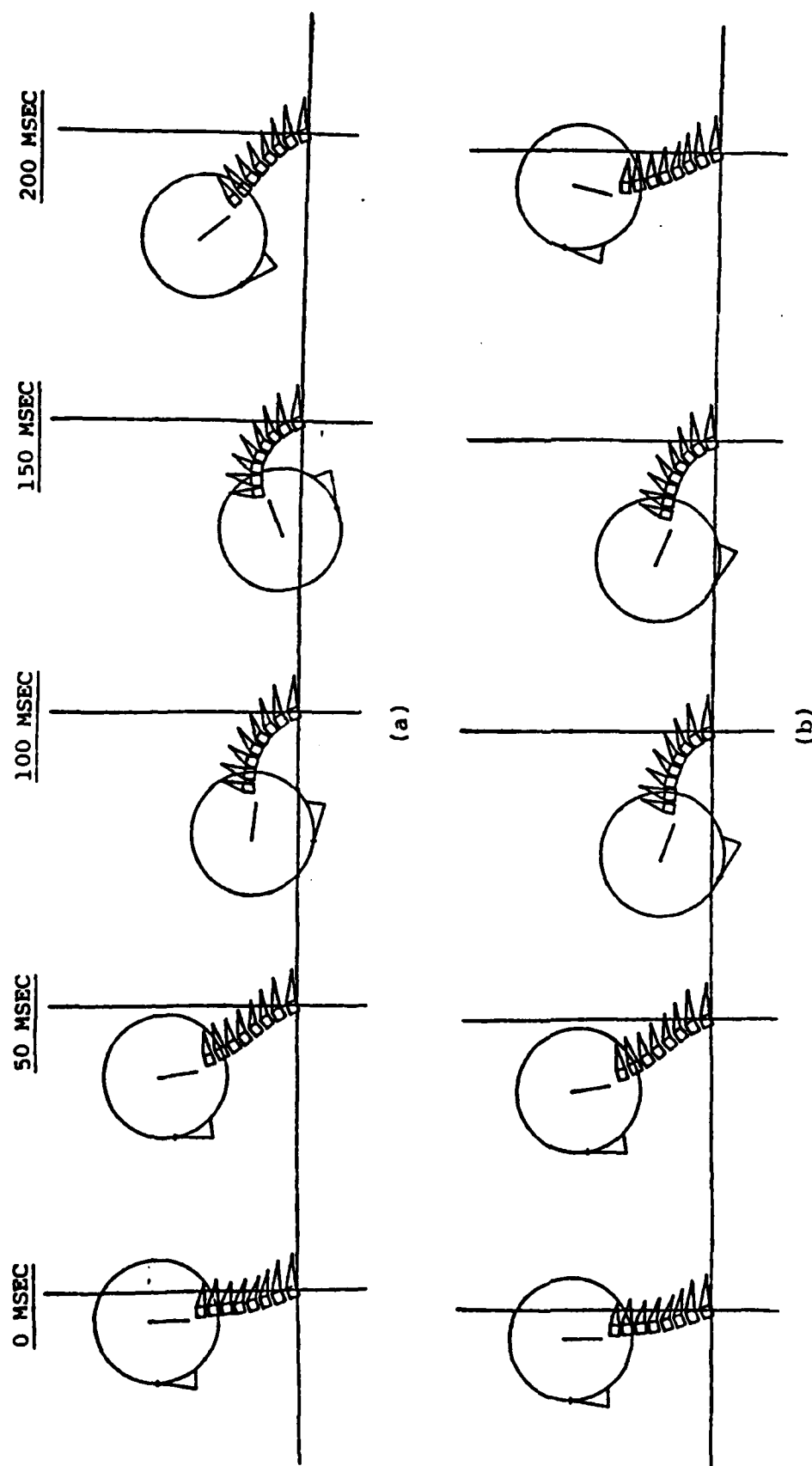


Figure 38. Response of isolated head-neck model to $-G_x$ impact acceleration;
 (a) with passive muscles
 (b) with stretch reflex response

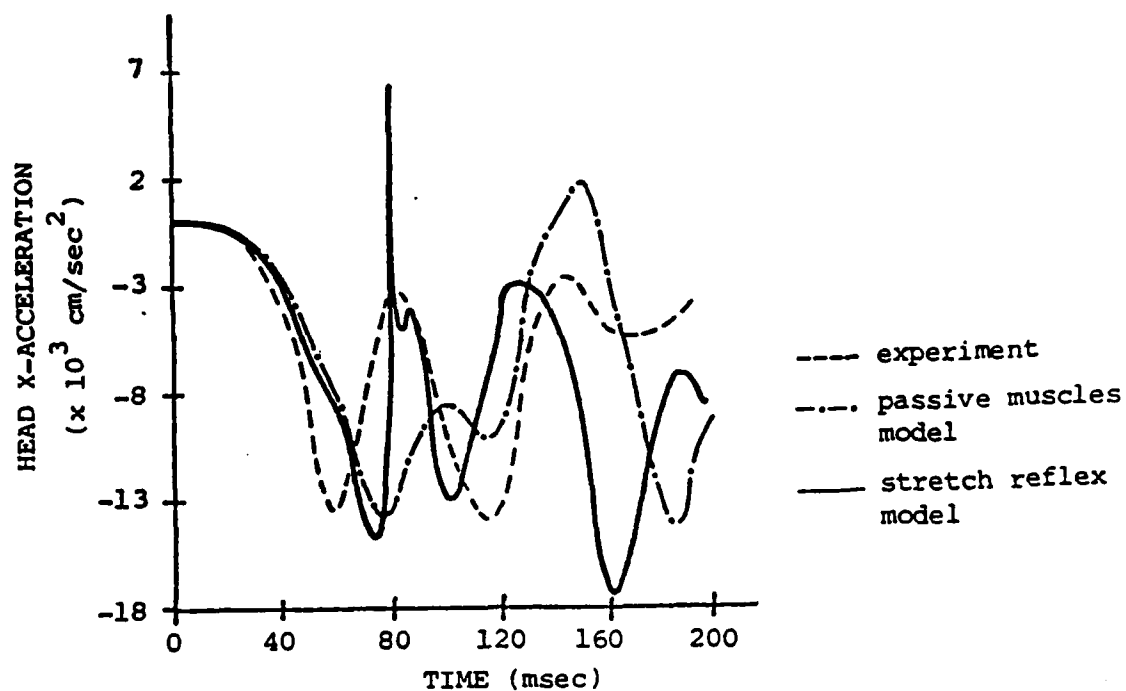


Figure 39. Comparison of head X accelerations during -G impact acceleration using the head-neck model.

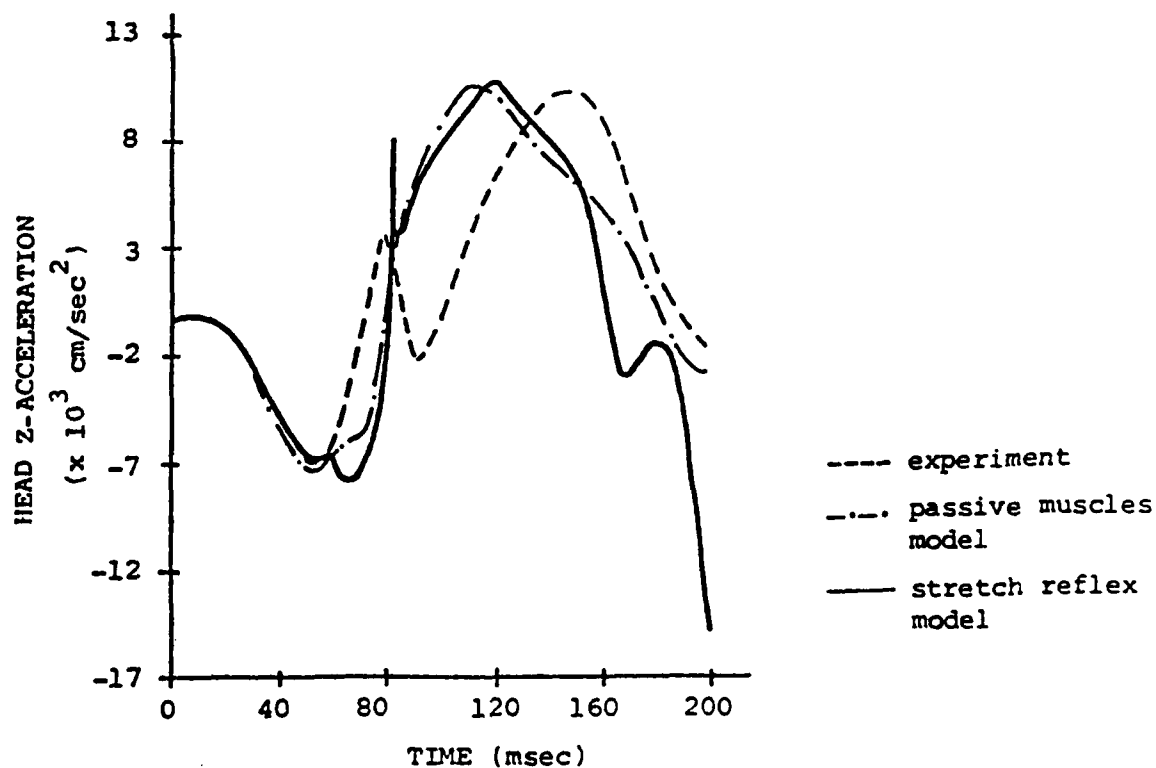


Figure 40. Comparison of head Z accelerations during -G impact acceleration using the head-neck model.

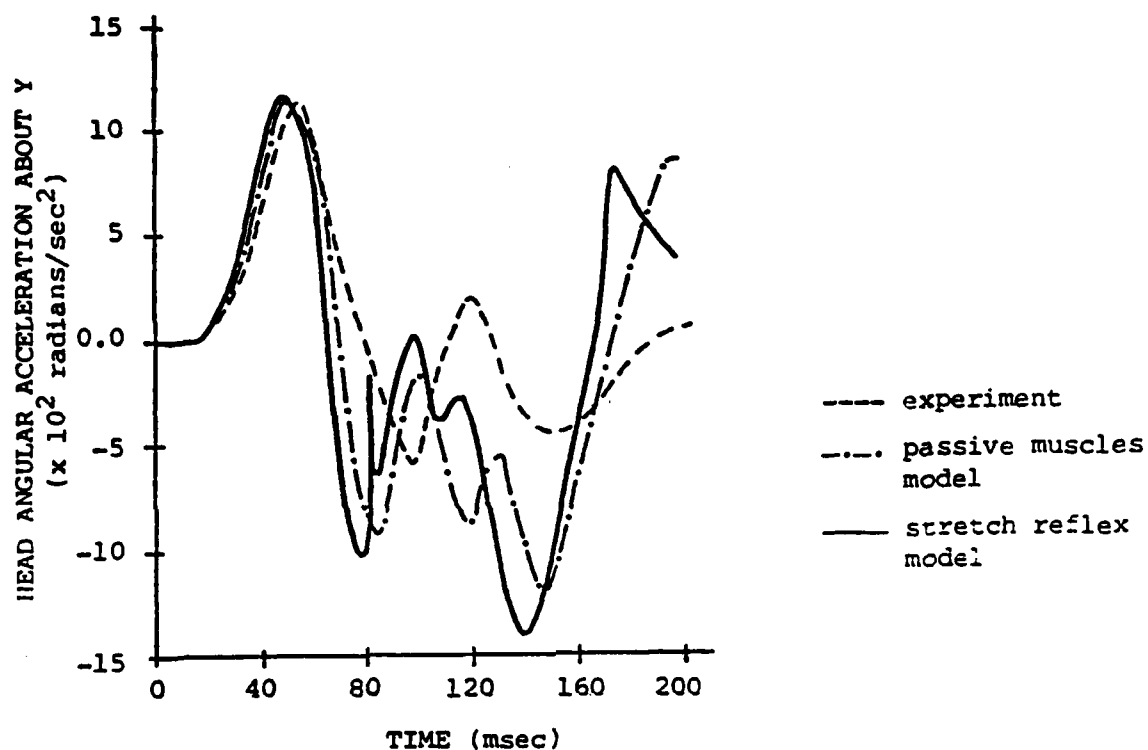


Figure 41. Comparison of head angular acceleration during $-G_x$ impact acceleration using the head-neck model.

displacements of the ligamentous model. With passive musculature the predicted peak Z-displacement of the head is 113% of the experimental peak (Figure 36); the predicted peak angular displacement is 167% of the experimental peak (Figure 37). With the stretch reflex response an almost perfect match is obtained between model and experiment, showing that the muscles exert a powerful influence on head and neck motion, especially angular displacement, even at high impact accelerations of 7.4 G.

Comparisons of experimental and model head accelerations are plotted in Figures 39 through 41. The linear acceleration of the head in the global X direction is portrayed in Figure 39. The experimental curve shows two characteristic peaks, the first of which occurs at 55 msec. Both the passive muscle model and the contracting muscle model exhibit a well-defined peak at 70-80 msec. A large positive spike appears at 80 msec in the model with stretch reflex response. This coincides roughly with the onset of substantial muscular contraction. It is evident that the experimental intermediate peak at 80 msec is also the result of muscular contraction in the experimental subject, because the passive muscle model shows only a small peak at about 100 msec. The second experimental peak at 120 msec is also apparently due to muscular contraction. It takes approximately 100 msec for the muscles to contract completely and the experimental accelerations decline to near zero at about 160-200 msec. The results with both models show large discrepancies after about 150 msec. As will be shown later, these are caused by the unnatural constraints imposed on T1. Figure 40 shows the linear acceleration of the head in the global Z-direction. Again the first peak in the experiment occurs at 55 msec. The passive muscle model gives similar results except for the intermediate experimental peaks at about 80-90 msec. These peaks are again due to muscular contraction as the results with the stretch reflex model

show.

The angular acceleration of the head is a triphasic response lasting from 40 msec to 250 msec in the experiment. Both the model with passive musculature and the model with contracting muscles predict the results quite well until about 140 msec, after which the effects of the unnatural constraints imposed on T1 are again noticed (Figure 41).

These results proved encouraging and of sufficient accuracy to warrant including the lower spine in order to simulate the $-G_x$ tests more realistically and to examine the effects of the restraint system on the head and neck response. Before describing the results with the lower spine included, it should be mentioned that the sensitivity of the model to changes in the material properties was briefly examined. A $-G_x$ simulation was repeated with passive musculature using stiffnesses for all of the elements which were 70% of the values used in the normal models. The head Z-displacement and angular displacement increased to 124% of the previous values; the accelerations were 114% of the previous values. The disc beam element forces were between 56% and 100% of the previous values, with an average of about 70%. There was no consistent pattern in the changes in element forces. It was concluded that the model is indeed sensitive to changes in material properties.

5.3 $-G_x$ Simulations with the Head-Neck Model Combined with a Simplified Thoracolumbar Spine Model

With the incorporation of the thoracolumbar spine via the SSM model, the effects of the unnatural constraints on the acceleration profiles are removed. The restraint system used in the $-G_x$ experiment was modeled by 3 linear springs with a stiffness of 1×10^8 dyne/cm each, in tension only. The

springs were attached to the spine at T1, T10 and L3. The pelvis was constrained from rotating and from translating laterally and vertically. The X-displacement function is prescribed at the pelvis. The T1 rigid body is constrained from lateral translation to maintain symmetry; it is otherwise free from constraints.

Figures 42a/b compare the deformed spine plots for the simulations with passive and contracting muscles with the thoracolumbar spine included. Figures 43 through 45 show the head X-, Z- and angular accelerations, respectively, for simulations with passive muscles and with the stretch reflex response. The results are much improved after 140 msec compared with the isolated head-neck runs, indicating that the constraints on T1 were the cause of the aforementioned problems after 140 msec. In the head X-acceleration plot in Figure 23 the second negative peak of the stretch reflex model is much smaller than it was in the isolated head-neck run and is also much smaller than the experimental peak at 120 msec. While the experimental value does change from individual to individual an effort was made for purposes of comparison, to choose an experimental curve which showed the average experimental response. This decrease in the second peak may be due to an inadequacy in the modeling of the restraint system.

Figure 46 compares the calculated angular displacement of T1 for the model with contracting muscles, to the experimental T1 rotation. This shows that a deficiency exists either in the lower spine model or in the way the restraints were represented. The peak linear acceleration of the sled in the global X-direction was about 10^4 cm/sec² for both simulations, or about 10Gs. Unfortunately, the Ewing and Thomas report (1972) does not provide T1 acceleration data so that this part of the simulation cannot be checked. A rotation at T1 of more than twice the experimental value may be due to

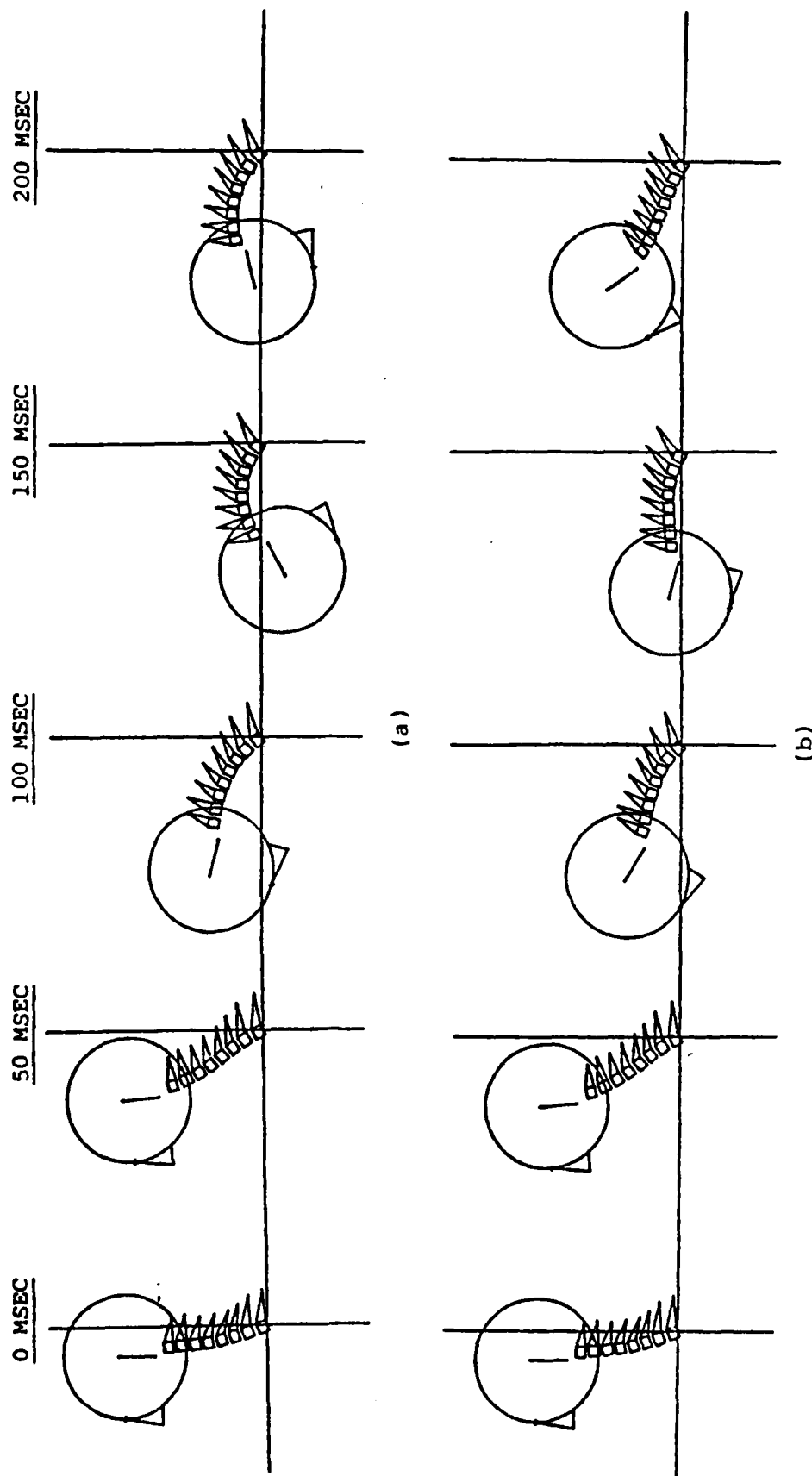


Figure 22. Response of head-neck model combined with thoracolumbar spine model to $-G_x$ impact acceleration. Lower spine is not shown.
 (a) with passive muscles
 (b) with stretch reflex response

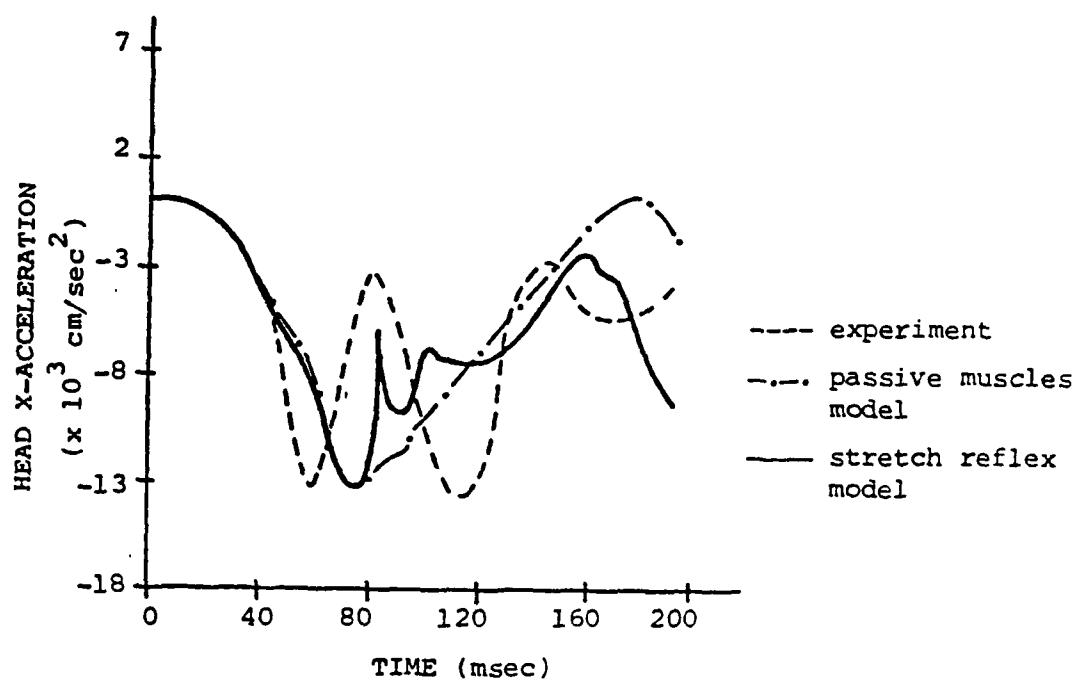


Figure 43. Comparison of head X acceleration during $-G_x$ impact accelerations using the head-neck model combined with the SSM model.

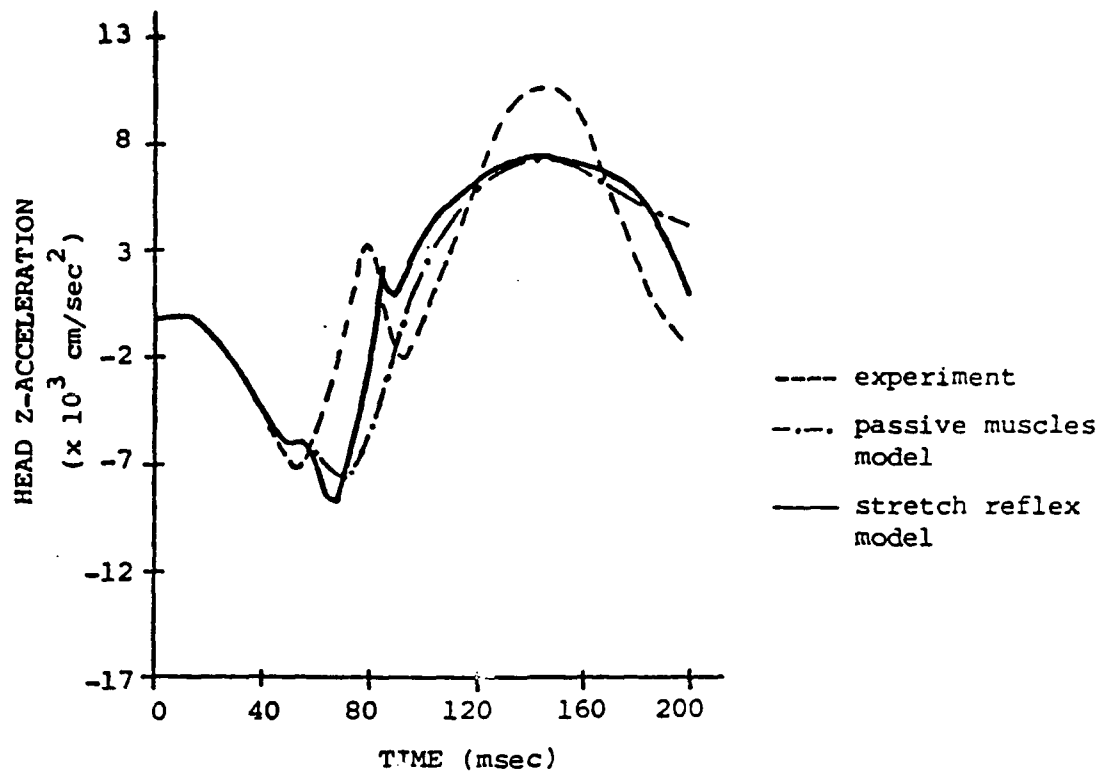


Figure 44. Comparison of head Z-acceleration during $-G_x$ impact acceleration using the head-neck model combined with the SSM model.

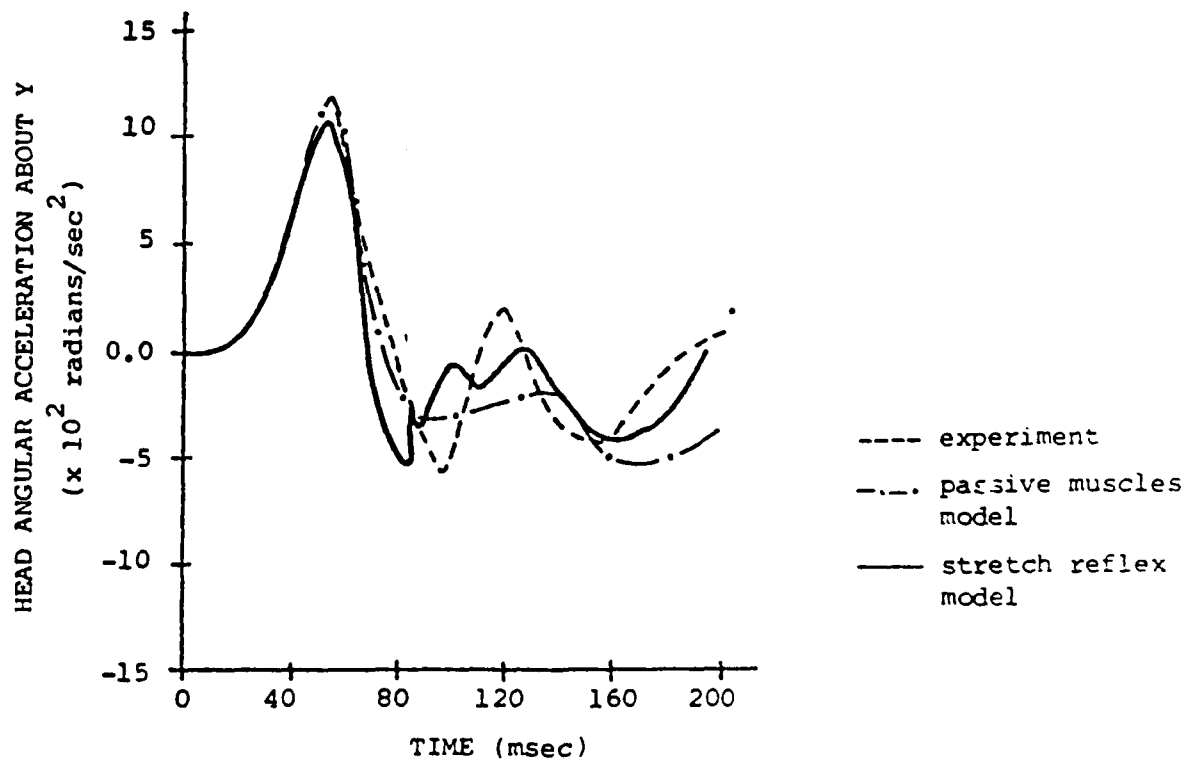


Figure 45. Comparison of head angular accelerations during $-G_x$ impact acceleration using the head-neck model combined with the SSM model.

AD-A161 425

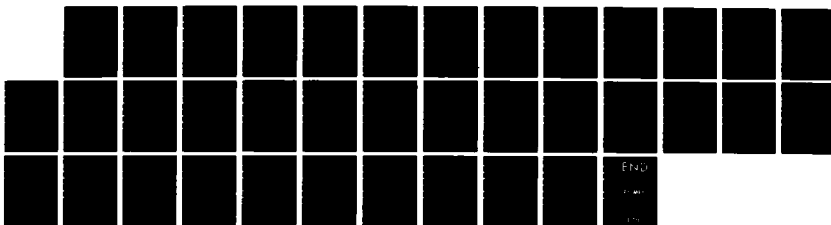
HEAD-SPINE STRUCTURE MODELING: ENHANCEMENTS TO
SECONDARY LOADING PATH MOD. (U) NORTHWESTERN UNIV
EVANSTON IL DEPT OF CIVIL ENGINEERING

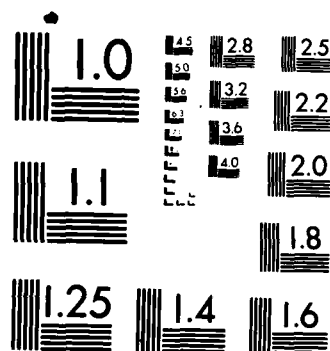
2/2

UNCLASSIFIED

T BELVTSCHKO ET AL JUL 85 AMRL-TR-85-019 F/G 6/19

NL





MICROCOPY RESOLUTION TEST CHART
NATIONAL BUREAU OF STANDARDS-1963-A

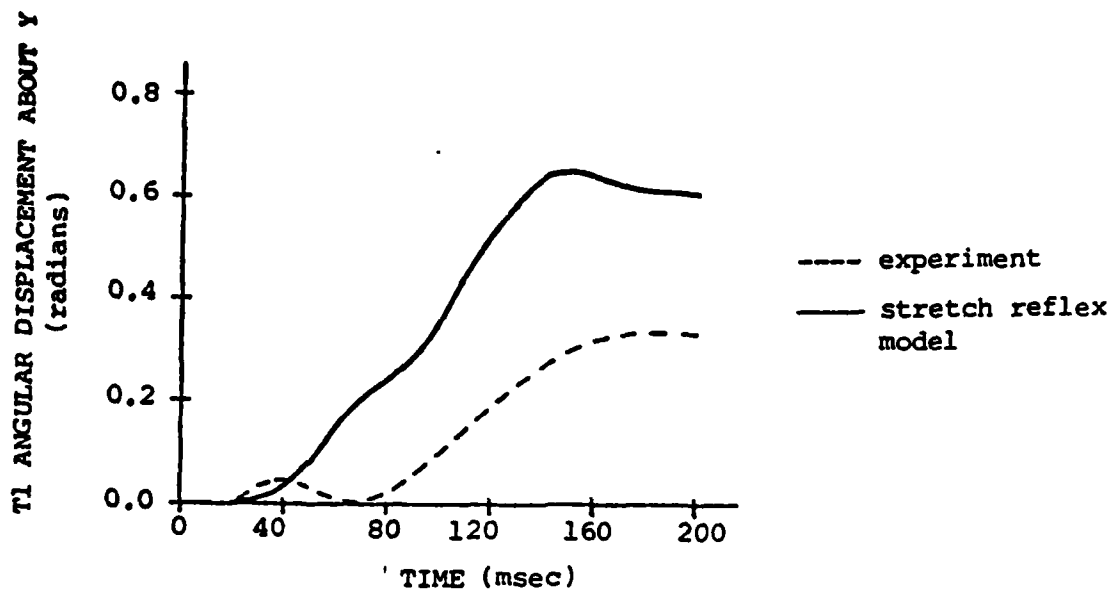


Figure 46. T1 angular displacement, during $-G_x$ impact acceleration.

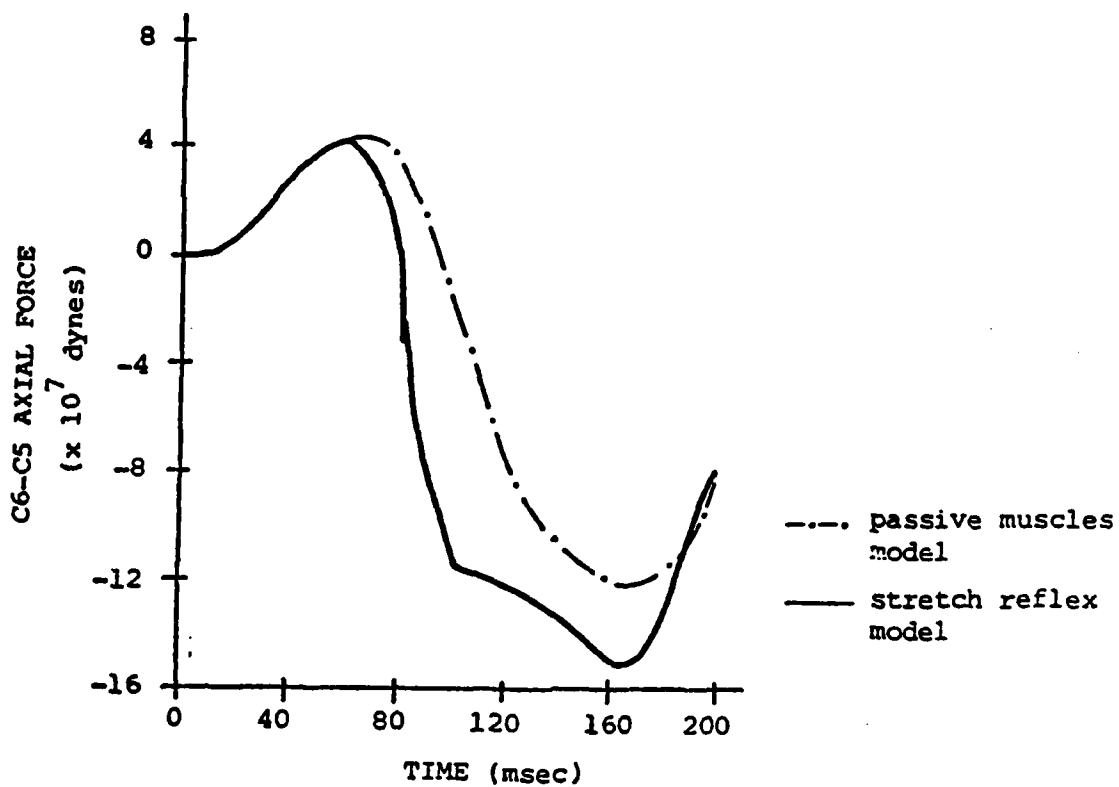


Figure 47. Time history of the axial force in the C6-C5 intervertebral disc during $-G_x$ impact acceleration.

omission of the restraint provided by the seatback.

As a result of the general agreement between the models and the experiment, some force data is discussed in order to examine the effects of muscular activity on the forces in the spine.

Table 2 shows a comparison of weak forces developed in the spine for $-G_x$ simulation with passive and contracting muscles. Figures 47 and 48 show typical axial and shear force time histories for the C6-C5 intervertebral disc. The axial force history is characterized by an initial tensile peak followed by a compressive peak value. Both tensile and compressive peak force values are listed in Table 2. The stretch reflex response increases the peak compressive axial force and the peak shear forces in the spine. The peak axial compressive forces increase by 20% to 50% in the discs and by 600% at the occipital condyles. The peak shear forces increase by 25% to 80% in the discs and by 250% at the occipital condyles. The peak tensile axial forces remain approximately the same.

The peak values for the moments were not obtained. The bending moments developed at 150 msec are tabulated in Table 3. Contraction of the neck muscles would appear to have the effect of decreasing the bending moment developed at the occipital condyles between a simulation with passive and with contracting muscles.

Forces developed in the neck ligaments and stresses developed in muscles are compiled in Tables 4 and 5 respectively. Muscular contraction is seen to decrease the ligament force levels during $-G_x$ impact acceleration. The stress levels reached in the muscles as a result of combined stretching and contraction are considerably higher than those reached in the passive muscle model. Figure 50 compares this difference as a function of time for the semispinalis cervicis muscle.

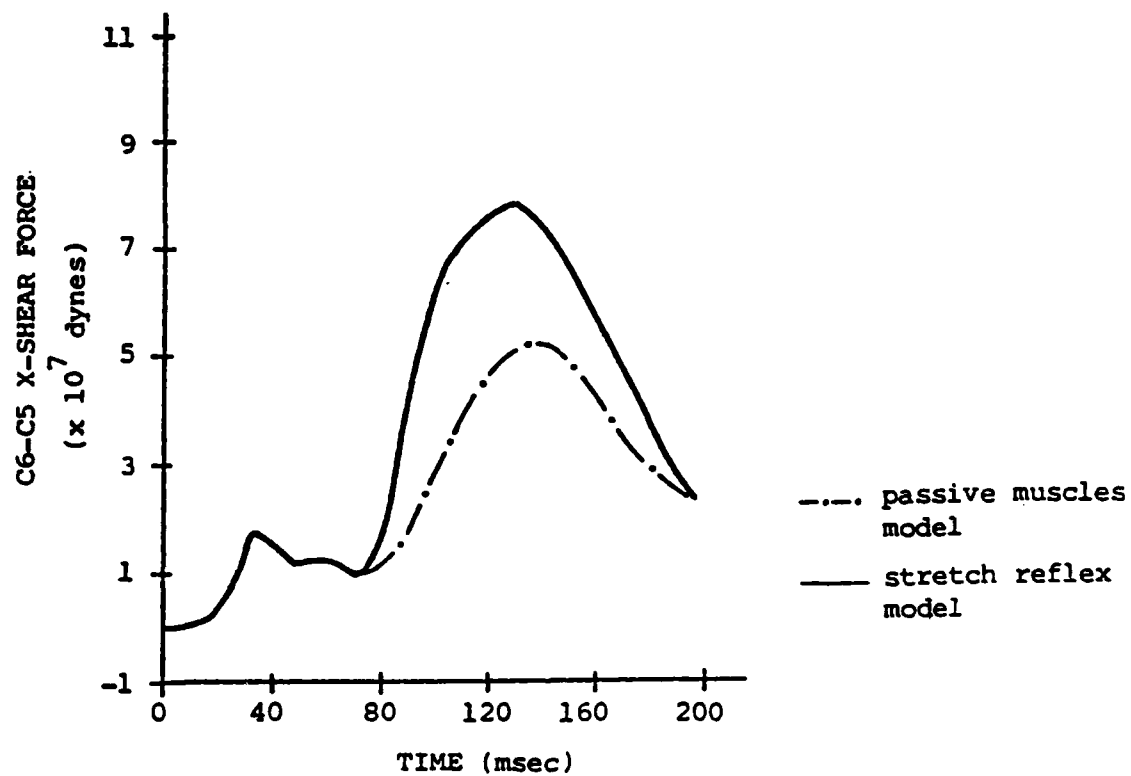


Figure 48. Time history of the shear force in the C6-C5 intervertebral disc during $-G_x$ impact acceleration.

TABLE 2

Peak Forces in Beam Elements During $-G_x$ Impact Acceleration
(All values $\times 10^6$ dynes)

Level	Simulation Run With Passive Muscles			Simulation Run With Stretch Reflex Response		
	Peak Axial Force		Peak Shear Force	Peak Axial Force		Peak Shear Force
	Tension	Compression		Tension	Compression	
T1-C7	21.8	-160	77.8	21.8	-201	118
C7-C6	30.5	-141	50.1	30.5	-173	93.7
C6-C5	43.9	-122	53.2	42.6	-151	77.8
C5-C4	47.5	-102	-45.1	45.7	-140	-68.5
C4-C3	52.8	-83.7	-36.8	49.6	-124	-43.3
C3-C2	54.4	-68.1	-39.0	54.4	-74.0	-29.2
C2-C1*	18.2	-19.0	-35.0	17.2	-8.60	-81.3
C1-H**	22.5	-5.8	-16.1	15.0	-37.2	-56.0

* These are forces in the element representing the joint formed by the odontoid process and C1.

** These are forces in the element representing the joint between the right occipital condyle and the right superior articular facet of C1.

TABLE 3

Bending Moments in Beam Elements
 During $-G_x$ Impact Acceleration
 (At 150 msec)
 (All values $\times 10^6$ dyne-cm)

Level	Simulation Run With Passive Muscles	Simulation Run With Stretch Reflex Response
	Moment at 150 msec	Moment at 150 msec
T1-C7	-186	-187
C7-C6	-158	-151
C6-C5	-161	-133
C5-C4	120	102
C4-C3	103	58
C3-C2	83	22

Note: These moments are not necessarily the peak values. The time histories of the moments were not obtained, so only the values at 150 msec are listed.

TABLE 4

Peak Force Levels in Neck Ligaments
 During $-G_x$ Impact Acceleration
 (All values $\times 10^6$ dynes)

Ligament	Simulation Run with Passive Muscles	Simulation Run with Stretch Reflex Response
	Force	Force
T1-C7 interspinous ligament	110	79
C2-C1 interspinous ligament	7.5	0.08
C1-H interspinous ligament	1.5	0.04
T1-C7 posterior longitudinal ligament	0.8	0.8
C5-C4 posterior longitudinal ligament	1.1	0.9
C2-C1 posterior longitudinal ligament	1.0	0.8
Posterior atlanto-occipital ligament	5.3	3.8
T1-C7 ligamentum flavum	8.2	7.7
C6-C5 ligamentum flavum	9.6	7.6

TABLE 5

Peak Stress Levels in Neck Muscles
 During $-G_x$ Impact Acceleration
 (All values $\times 10^6$ dyne/cm²)

Muscles	Simulation Run With Passive Muscles	Simulation Run With Stretch Reflex Response
	Stress	Stress
Rectus capitis posterior major	0.54	2.40
Spinalis cervicis	1.17	5.40
Spinalis capitis	0.12	3.62
Semispinalis cervicis	0.71	4.73
Semispinalis capitis	0.68	3.75
Multifidus (C5-C6)	0.08	3.89
Interspinalis (C4-C5)	1.17	5.68
Obliquus capitis superior	0.21	3.06
Splenius capitis	0.79	4.25
Splenius cervicis	0.54	4.46
Longissimus cervicis	0.39	4.28
Longissimus capitis	0.37	3.10
Levator scapulae	0.37	4.15
Trapezius	0.49	3.83

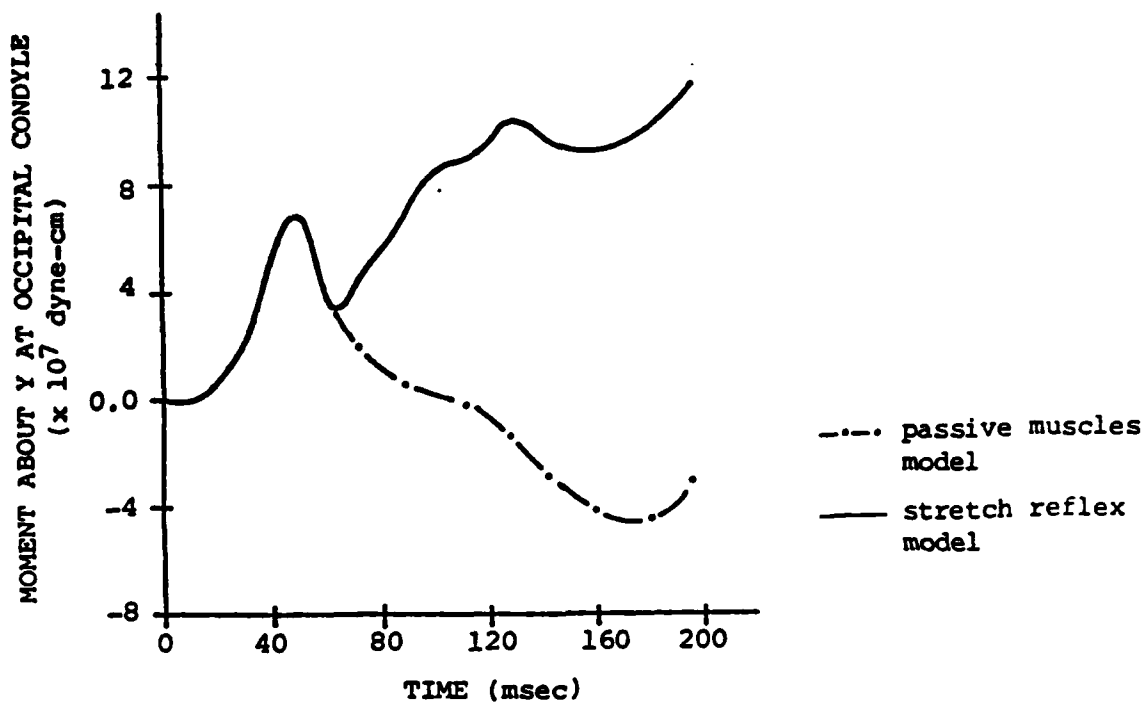


Figure 49. Time history of the moment developed at the right occipital condyle during $-G_x$ impact acceleration.

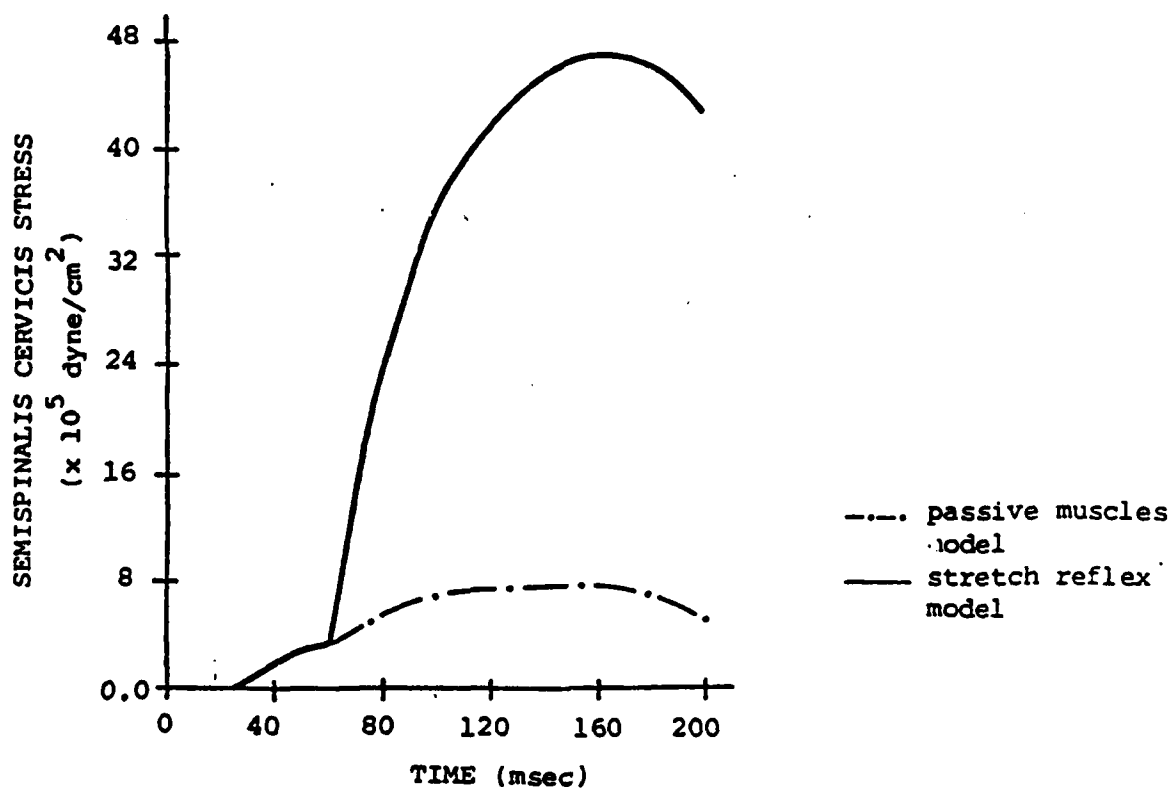


Figure 50. Time history of the stress developed in the semispinalis cervicis muscle during $-G_x$ impact acceleration.

The peak force developed at each facet was obtained for levels T1-C7 and C2-C1. At T1-C7, a tensile force of 2.6×10^7 dynes per facet was reached during both passive and contracting muscle simulations. At C2-C1 a peak tensile force of 1.6×10^7 dynes per facet was obtained during the simulation with passive muscles; whereas a peak compressive force of -4.3×10^7 dynes was obtained with the stretch reflex response.

To relate the motions and forces discussed above to specific injury levels is beyond the scope of this study and would require accurate data for the tissues involved. In general terms, it is noted that the ligaments seem more likely to be injured in a cadaver subject than in a living subject during $-G_x$ testing. The muscles, on the other hand, seem more likely to suffer damage in the living subject. It is also interesting to note that the shear forces in the disc change sign between levels C6-C5 and C5-C4; the moments at 150 msec also change sign at the same level. These events may be related to the high incidence of injury at the C6-C5 level.

In comparing the results of the simulations with the isolated head and neck model to the runs with the thoracolumbar spine included, notable differences in the force levels in the spine were observed. By adding the lower spine model and freeing T1 from constraints, the peak axial and shear forces and the bending moments were reduced by 50%. It is therefore concluded that constraints imposed on T1 in the isolated head and neck model significantly altered the force distribution in the spine.

5.4 +G_y Impact Simulation

To test the lateral behavior of the model, comparisons were made with the +G_y impact test of Ewing et al. (1978). In these experiments, volunteers were subjected to peak sled accelerations in the lateral direction of up to 7.5G. The human lateral response is quite different from the -G_x response. For the same magnitude of sled acceleration, the acceleration of the head was much greater in the +G_y experiments than in -G_x experiments. There was also a relatively high incidence (16 out of 35 runs) of run-related clinical effects in the -G_y experiments. The symptoms involved neck pain, stiffness and soreness, predominantly on the extension side of the neck. While these symptoms were reported to be mild, the experiments on human subjects were limited to 7.5G, because the head comes close to direct impact of the right shoulder at this level of acceleration.

As in the -G_x experiments, the head and neck were unrestrained in all tests. The same method was used to measure accelerations as in the -G_x tests described previously. The lateral restraint system consisted of a lap belt threaded through loops in the shoulder straps. In addition to the shoulder strap and solid restraints, an eight-inch wide nylon net encompassed the chest to alleviate the force on the shoulder. The thrust vector of the sled was directed from the right to the left side of the subject, who was snugly positioned against a wooden board used to decrease upper torso motion.

The accelerations measured at T1 indicated that in the +G_y tests T1 motion can be significant, whereas in the -G_x tests motion at T1 is very small. Ewing et al. (1978) concluded from their experience with these -G_x and +G_y tests that the higher head acceleration in the +G_y tests is due to a higher acceleration at T1 for the same sled acceleration. They suggested that

the difference is due to the manner in which the torso is restrained in the X and Y directions. There is a possibility that the measured acceleration at T1 for the $+G_y$ test includes artifact, because the instrumentation mount at T1 is not rigidly connected to the bone. The accelerometer is mounted under pressure at the T1 level, but because of the intervening soft tissue between the bone and the instrument, relative motion between the mount and the bone is possible. Ewing et al. (1977) do not believe that their T1 measurements are due to motion between the bone and the mount. The results of simulations with the neck model described next corroborate the experimental findings.

5.5 $+G_y$ Simulations with the Head-Neck Model Isolated from Thoracolumbar Spine

As in the $-G_x$ simulations preliminary testing of the model was carried out using only the head-neck system with T1 as the base. The experimental data used for comparison with the model was obtained from a 7G run in which the sled acceleration profile rose from zero to -70 m/sec^2 , followed by a drop to zero at 140 msec. Thus the measured input to the neck was about twice the sled acceleration.

Only one $+G_y$ simulation was carried out with the isolated head-neck model. In this run the base of the model (T1) was constrained from all rotations and from X and Z translations. The experimentally measured T1 acceleration was used as input, by prescribing the Y component of the displacement at T1 as

$$u_y(t) = \begin{cases} 66666.67, & 0 \leq t < 0.04 \text{ sec} \\ -160000 \cdot \left(\frac{t}{6}\right)^3 - 0.07 t^2 + 0.0028t - 3.7333 \times 10^{-5}, & t > 0.04 \text{ sec} \end{cases}$$

The muscles were not yet included in this model and the ligaments and facets were represented by linear spring elements. Figure 51 shows the deformed configuration of the head and neck. The ligamentous neck model behaves completely unrealistically beyond 100 msec. This is due to a posterior displacement of the head which reaches a maximum of -20 cm at 150 msec. The cause of this extreme posterior displacement and subsequent collapse of the neck model was to become clear only after an exhaustive investigation, in which the possible causes were dealt with one at a time.

5.6 +G_y Simulations with the Head-Neck Model Combined with a Simplified Thoracolumbar Spine Model

A decision was made to incorporate the thoracolumbar spine to investigate if the unnatural constraints at T1 or the high acceleration prescribed at T1 could cause the head-neck behavior described. In the course of these studies it was found that proper modeling of the restraint system used in the +G_y experiments is even more crucial than in the -G_x impact simulations. The report of Ewing et al. (1978) provides detailed angular displacement data at the T1 level. By comparing the T1 angular displacement calculated in the model to the experimental data, the restraint system for the thoracolumbar spine model could be adjusted to match the experiments.

Five spring elements were used with linear stiffnesses of 1×10^8 dyne/cm each, in tension only, to represent the belt restraints (Williams, 1981). A single spring was attached at the L3 level as in the -G_x simulations. The

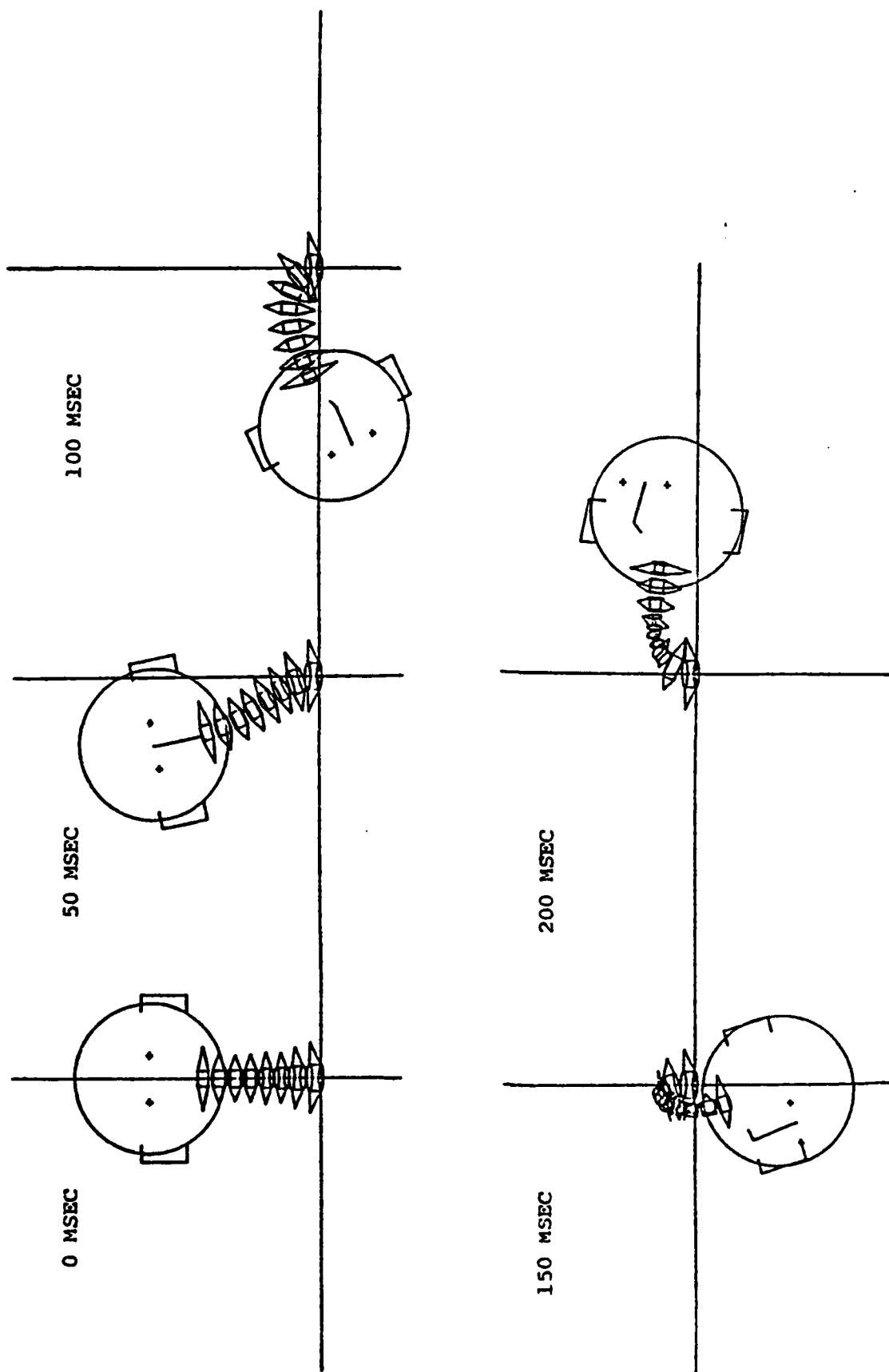


Figure 51. Response of isolated ligamentous head-neck model to +6_y impact acceleration.

other four springs were placed in pairs at the T1 and T10 levels to model the shoulder and chest straps. These springs are connected to T1 and T10 rigid bodies through rigid linkages; two springs are connected to each body at a distance of 10 cm from the center. This in itself is insufficient to model the restraints, because the seatback also needs to be included. This was accomplished by simply constraining all nodes below and including T10 from translation in the X-direction and from rotation about the vertical axis. However, even with these constraints satisfactory results could not be obtained. It was found to be absolutely essential to constrain T1 translation in the X-direction in order to obtain reasonable results.

With the above discussed seatback and seatbelt restraints included, satisfactory accelerations were obtained at the T1 level, but the basic problem of backward motion of the head remain unsolved. Addition of musculature did not offer any improvements either. It was finally discovered that the structural arrangement of springs modeling the facets suffers from snap-through during $+G_y$ simulation, thereby causing the head and neck to collapse in the posterior direction. This problem of snap-through does not occur in $-G_x$ simulations, because during flexion of the head and neck the facets are placed in tension. Moreover, the three-dimensional nature of the head and neck response to lateral acceleration further compounds the problem by twisting the springs out of alignment. However, even in two-dimensional motion, problems may occur if the facets are loaded under large compression forces such as would happen in a $+G_x$ simulation of whiplash, for example. By developing a new element for the facets as described in Williams (1981), the problem of extreme posterior displacement of the head during lateral acceleration was solved.

Two $+G_y$ impact simulations are described next. In both, the facets are

represented by the pentahedral facet elements discussed at length in Williams (1981) and the ligaments are modeled by nonlinear springs. The displacement function which is prescribed at the pelvis is as follows:

$$u_y(t) = \begin{cases} 29166.667 t^3, & 0 < t < 0.04 \text{ sec} \\ -70000 \left[\frac{t^3}{6} - 0.07 t^2 + 0.0028t - 3.7333 \times 10^{-5} \right], & 0.04 < t < 0.14 \text{ sec} \\ 490 [t - 0.06], & t \geq 0.14 \text{ sec} \end{cases}$$

This corresponds to the experimental run at 7G. In the first simulation the muscles of the neck remain passive throughout the 200 msec run; in the second, the lateral flexors of the head and neck on the left side are stimulated to contract at 40 msec after the start of the impact acceleration. A total of 10 different muscle groups are stimulated to contract in the model. While all of these are lateral flexors, some also function as extensors of the head and neck. The deformed configurations of the spine are shown in Figures 52a/b for the passive muscle simulation and the simulation with the stretch reflex response.

Figure 53 compares the T1 Y-accelerations of the model and experiment. Excellent agreement is obtained. The calculated peak acceleration of $1.6 \times 10^4 \text{ cm/sec}^2$ provides corroboration for the T1 acceleration measurement of Ewing et al. (1978).

Figure 54 and 55 show the head X- and Z-displacements, respectively. The stretch reflex response in the model pulls and rotates the head backward to a greater extent than in the experiment. The explanation for this is that some of the lateral flexors are also extensors. In the living subject presumably some sort of synergistic action takes place to eliminate this undesirable movement. The interaction and cooperation among the muscles would have to be

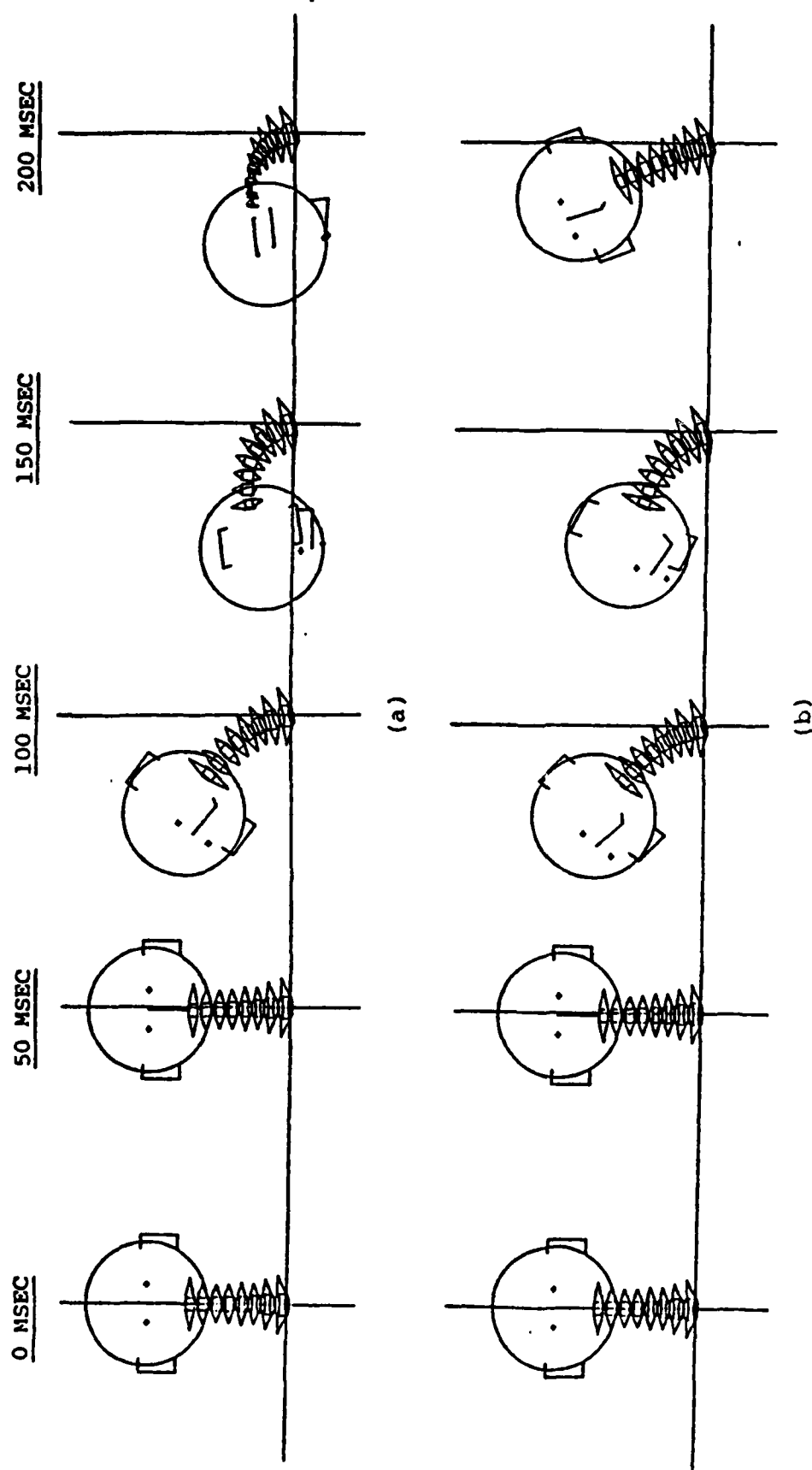


Figure 52. Response of head-neck model combined with thoracolumbar spine model to $+G_y$ impact acceleration. Thoracolumbar spine is not shown.
 (a) with passive muscles
 (b) with stretch reflex response

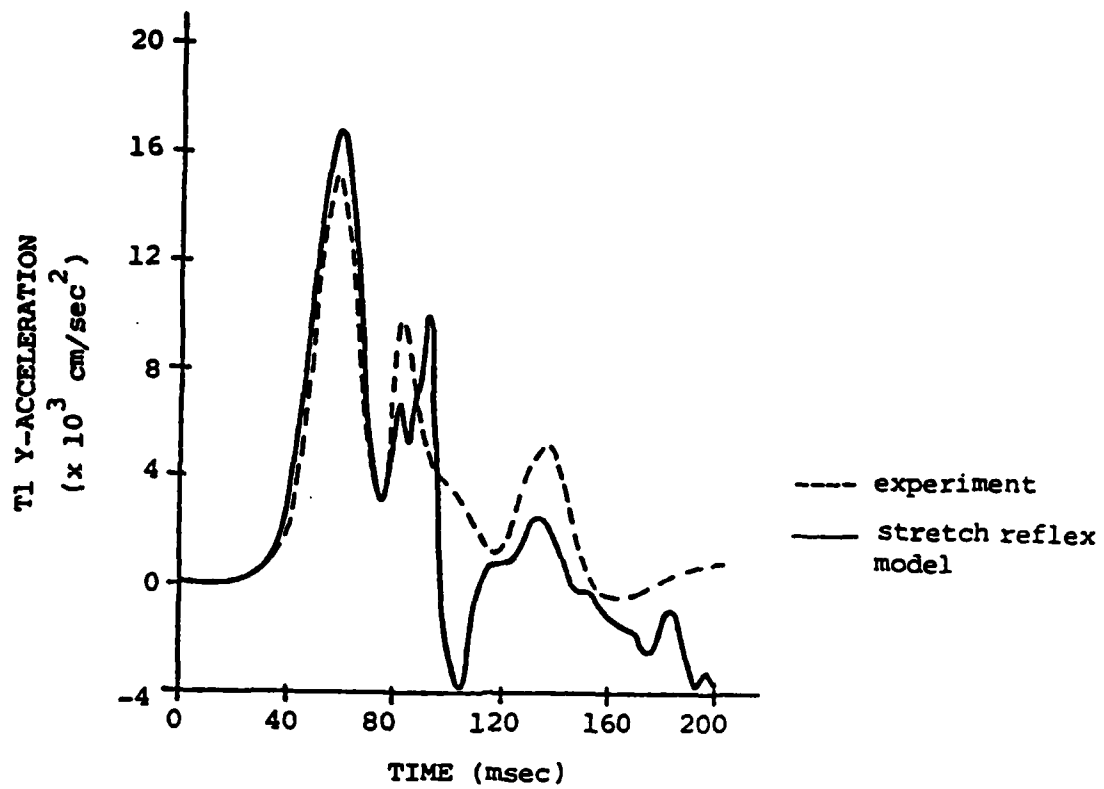


Figure 53. T1 Y-acceleration during +G_y impact acceleration.

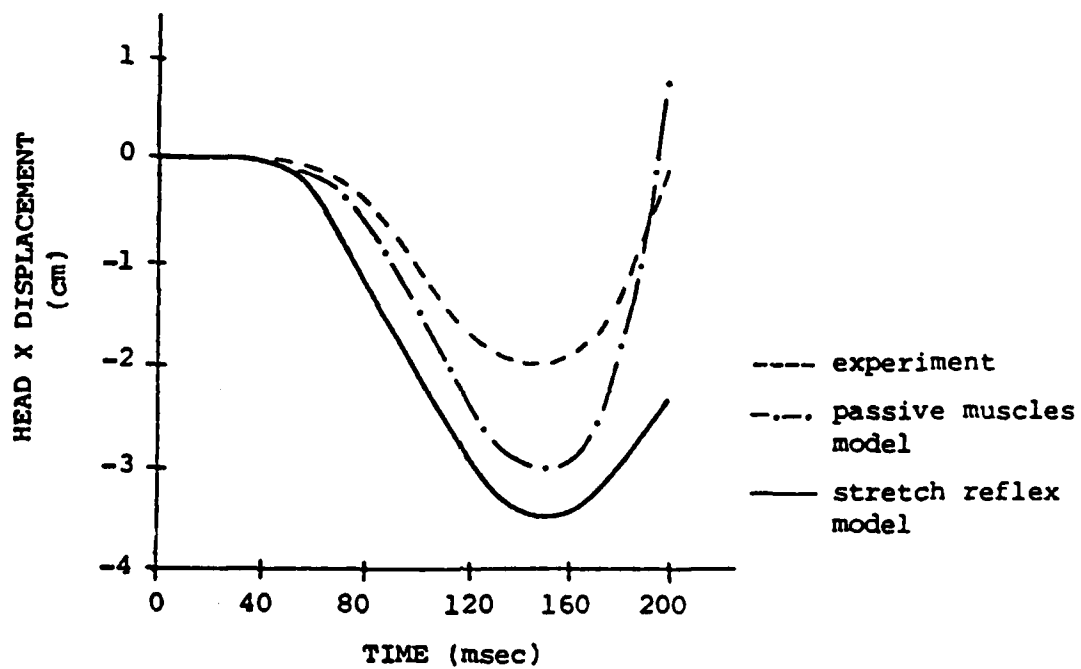


Figure 54. Head X-displacement during +G_y impact acceleration.

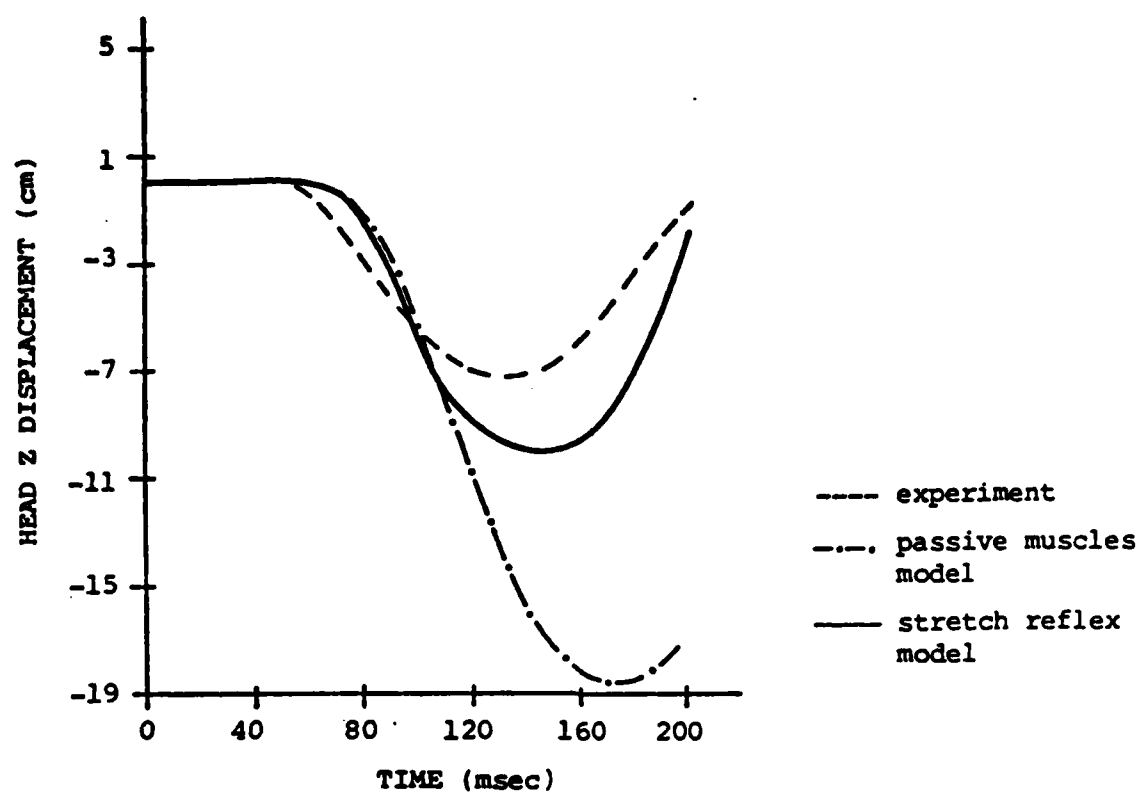


Figure 55. Head Z-displacement during $+G_y$ impact acceleration.

understood to coordinate this activity in the model. As in the $-G_x$ results, the Z-displacement of the head for the passive muscle model is much greater than for the experiment. With the stretch reflex response, the model matches the experiment quite well.

Angular displacements about the \bar{x} , \bar{y} and \bar{z} axes of the head are portrayed in Figures 56 through 58. Good agreement is obtained for the muscle reflex model except for the rotation about the \bar{y} -axis. This is again due to the contracting lateral flexors which are also extensors. The passive muscle model matches the \bar{y} -rotation better. Rotation about the \bar{z} -axis is matched extremely well for the stretch reflex model. In the passive muscle model the head continues to rotate about \bar{z} during lateral bending to the right as shown in the deformed spine plots (Figure 52).

Figures 59 through 61 display the head X-, Y- and Z-accelerations for both models in comparison to the experiment. Figures 62 and 63 compare head angular accelerations about the head \bar{x} and \bar{y} axes, respectively. The agreement is quite good except for the angular acceleration about \bar{y} , which differs from the experiment for the same reasons discussed above for the \bar{y} -rotation.

The forces developed in the spine during these lateral impact simulations are summarized in Table 6 by comparing the passive muscle model with the stretch reflex model. It is of interest to note that the peak tensile forces developed in the discs are greater than the peak compressive forces. This is in direct contrast to the $-G_x$ simulation where the compressive forces are greater than the tensile forces. The action of the muscles during stretch reflex decreases the peak tensile loads in the discs by 20% to 70%. Peak compressive forces are also decreased by an average of 50%. Peak shear forces either remain unchanged or are decreased by up to 40%.

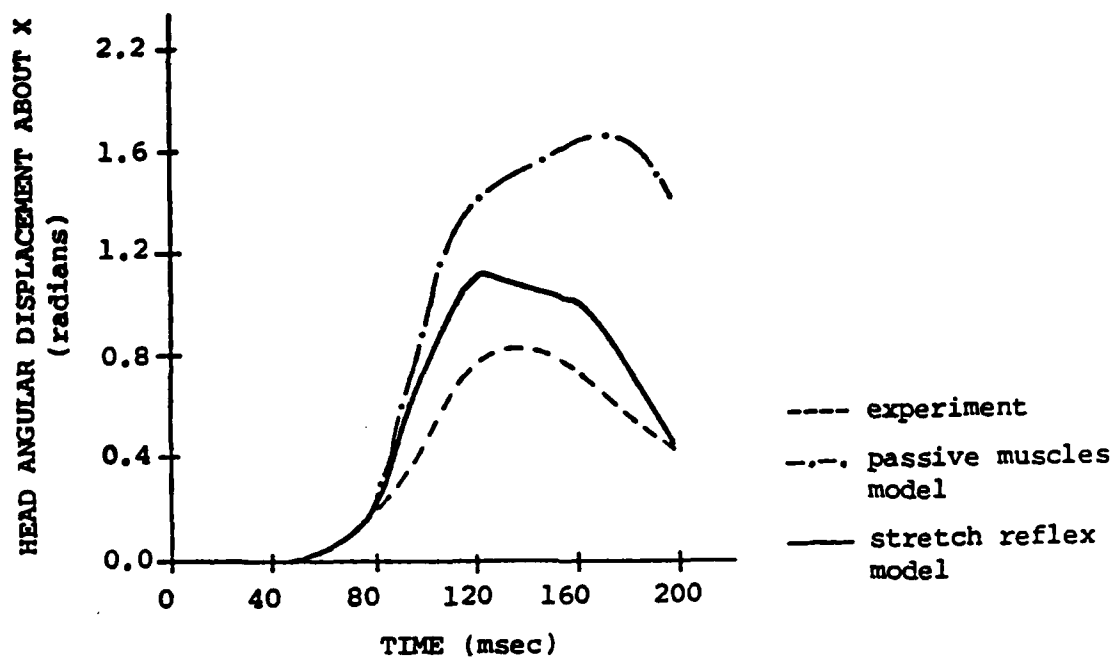


Figure 56. Head angular displacement about \bar{x} during $+G_y$ impact.

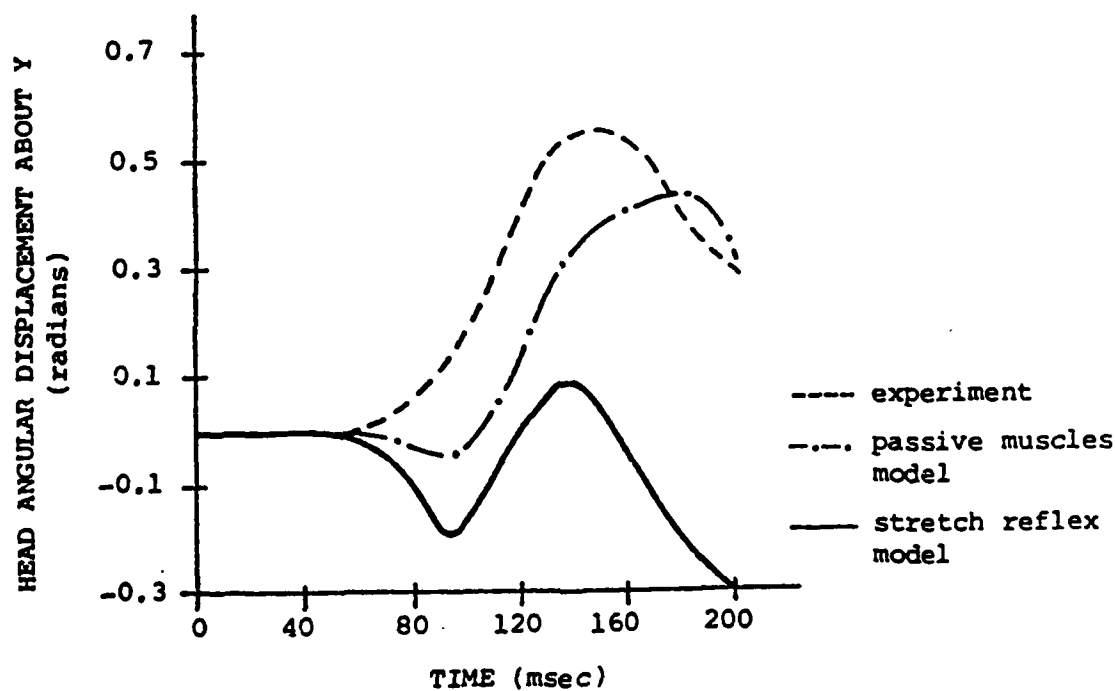


Figure 57. Head angular displacement about \bar{y} during $+G_y$ impact.

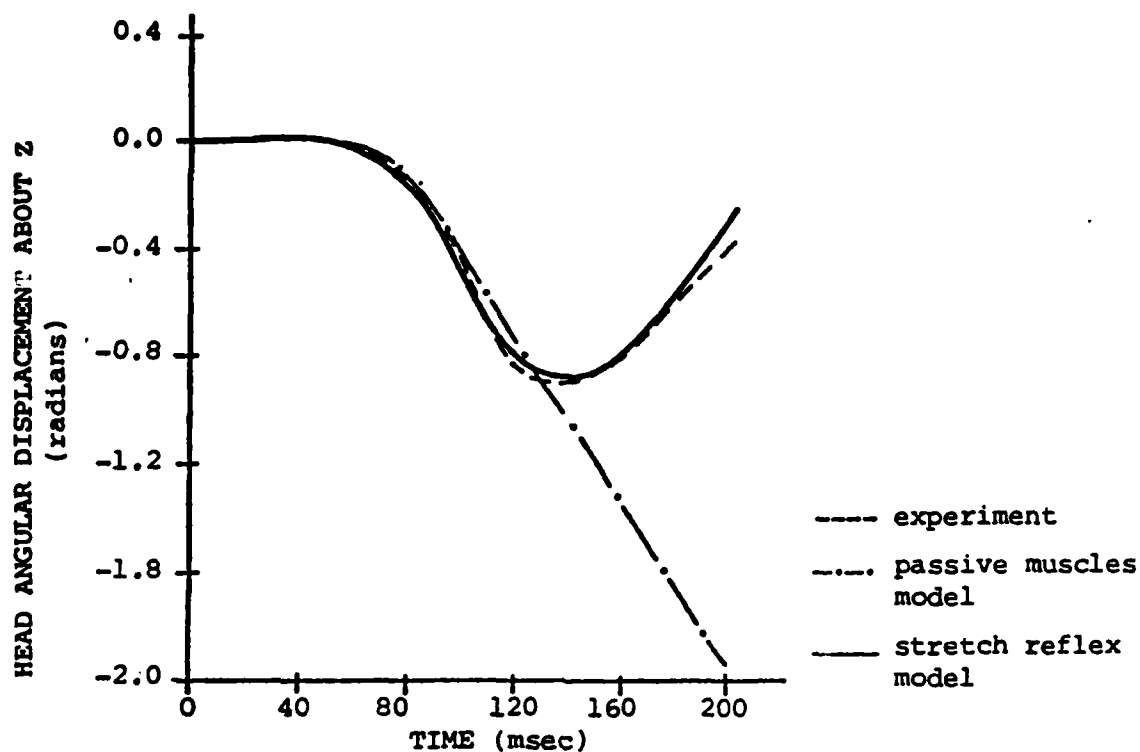


Figure 58. Head angular displacement about Z during +G_y impact.

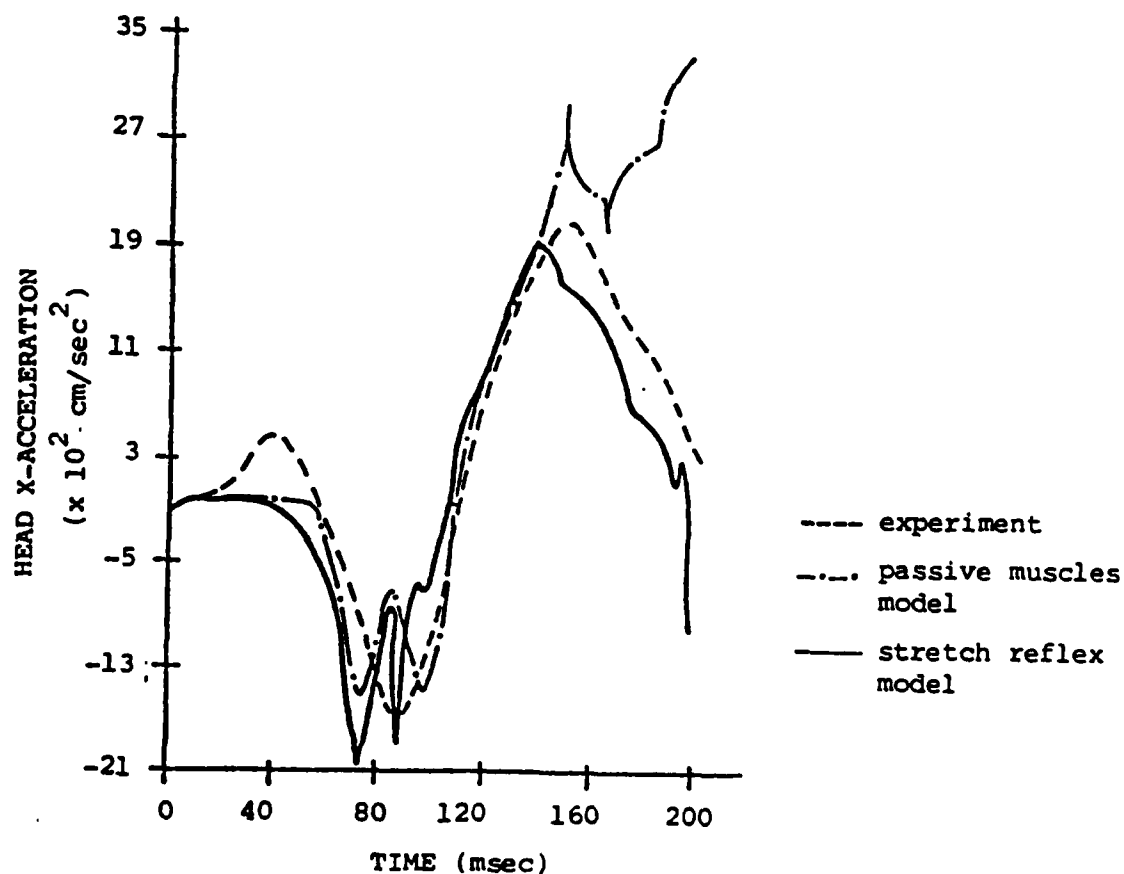


Figure 59. Head X-acceleration during +G_y impact.

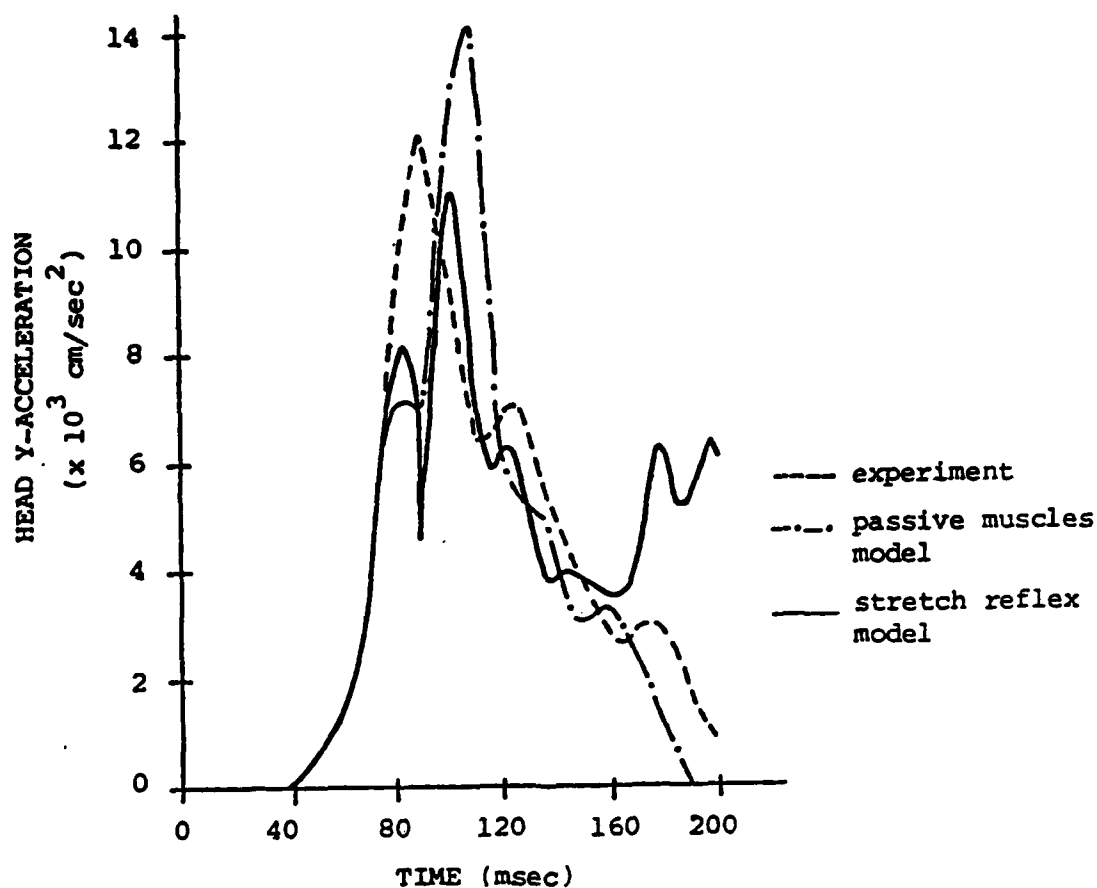


Figure 60. Head Y-acceleration during $+G_y$ impact.

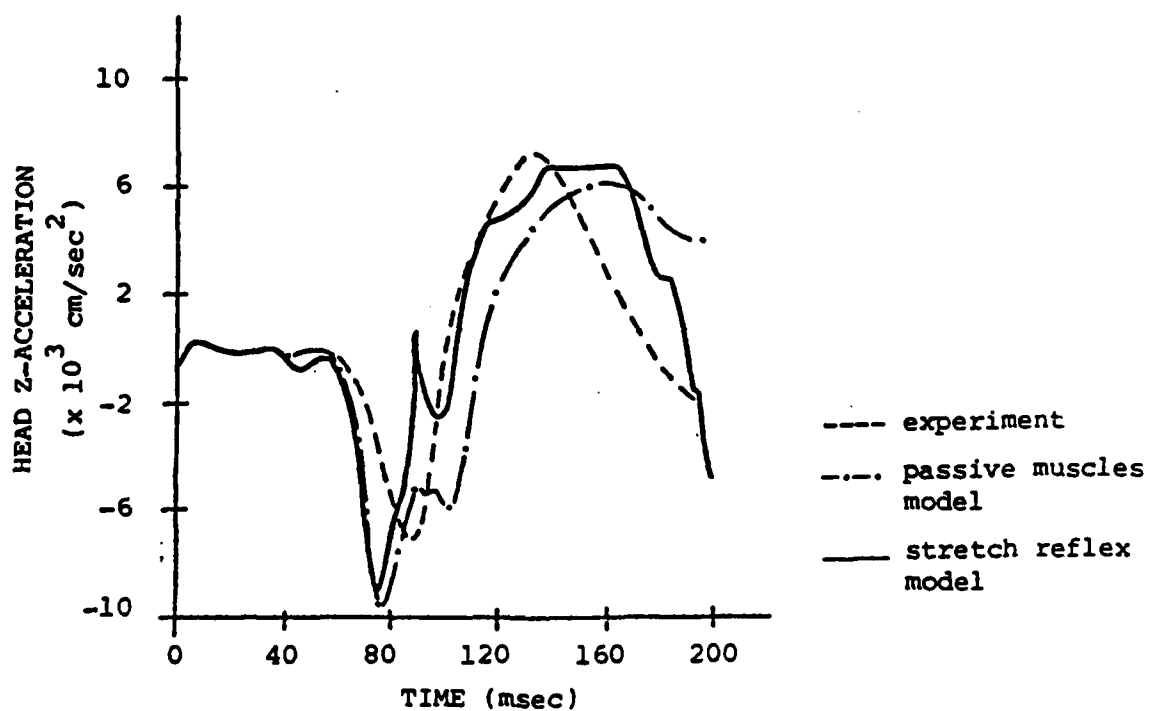


Figure 61. Head Z-acceleration during $+G_y$ impact.

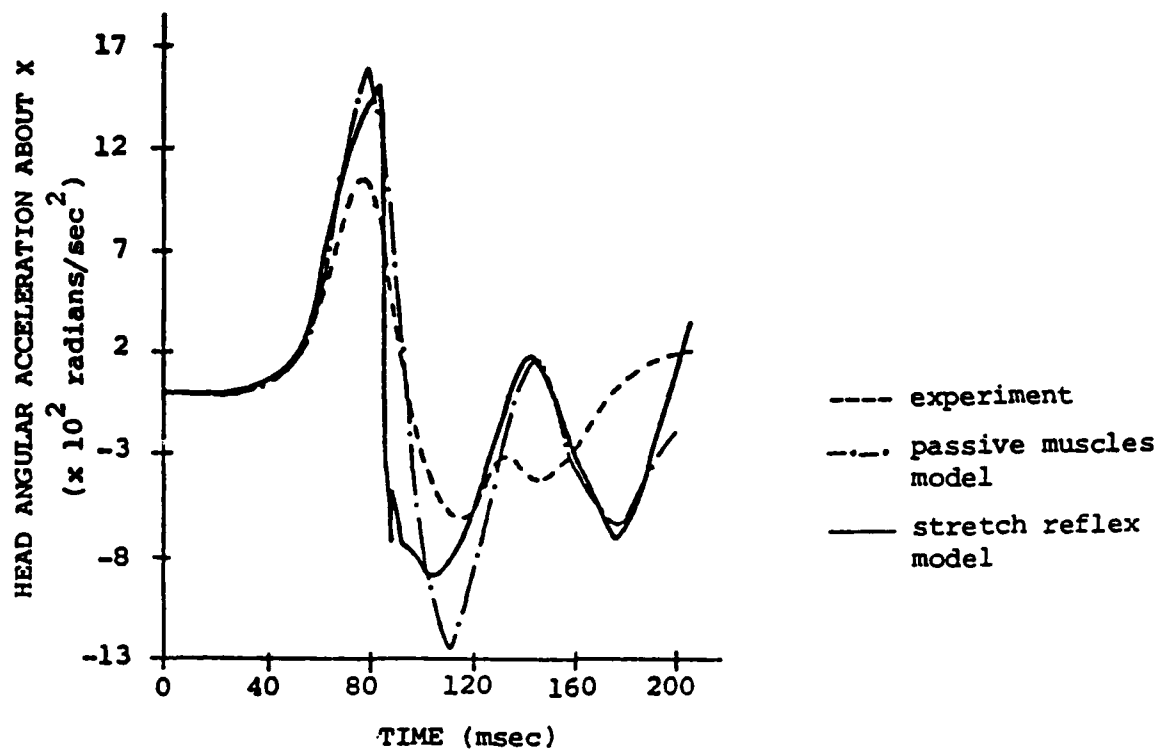


Figure 62. Head angular acceleration about \bar{x} during $+G_y$ impact.

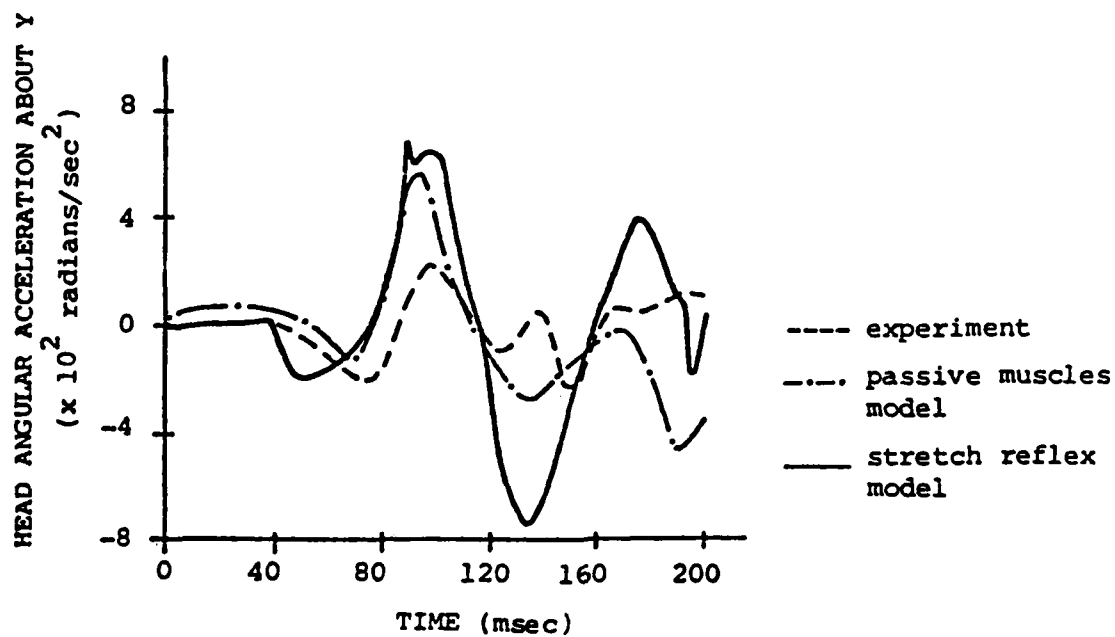


Figure 63. Head angular acceleration about \bar{y} during $+G_y$ impact.

TABLE 6

Peak Forces in Beam Elements During +G_y Impact Acceleration
(All value x 10⁶ dynes)

Level	Simulation Run With Passive Muscles			Simulation Run With Stretch Reflex Response		
	Peak Axial Force		Peak Shear Force	Peak Axial Force		Peak Shear Force
	Tension	Compression		Tension	Compression	
T1-C7	86.9	-37.7	-28.1	67.9	-9.2	-29.8
C7-C6	82.7	-2.30	-13.7	35.6	-16.8	-12.8
C6-C5	78.1	-25.0	-39.6	23.4	-23.3	-26.3
C5-C4	69.9	-25.5	52.2	25.6	-13.6	33.0
C4-C3	77.2	-24.0	52.4	32.4	-12.3	36.8
C3-C2	86.8	-21.3	60.4	34.0	-19.3	38.6
C2-C1*	23.0	-1.34	51.1	15.7	-7.2	57.4
C1-H**	33.7	-44.4	18.0	23.0	-78.2	25.9

* These are forces in the element representing the joint formed by the odontoid process and C1.

** These are forces in the element representing the joint between the right occipital condyle and the right superior articular facet of C1.

Peak bending moments developed in the disc beam elements are listed in Table 7. Unlike the $-G_x$ simulation where only flexion occurs, the $+G_y$ problem is a three-dimensional problem in which moments develop due to lateral flexion, extension-flexion, and torsion of the spine. Muscular contraction decreases the moments by 15% to 40%.

Peak forces in the facet elements are compared in Table 8 for the left and right facets at T1-C7 and C2-C1. Only the magnitudes are calculated for the shear forces acting on the planes for the facet joint. Muscular contraction during lateral impact increases the forces normal to the facets on the compression side (right side) by 150%, while the shear forces remain unchanged. The compressive forces acting at these facets are about ten times as large as the compressive forces in the discs at the same levels. The shear force at the right T1-C7 facet is five times the shear force in the T1-C7 disc. Figures 64 and 65 show the time history of the axial and shear forces in the right T1-C7 facets.

Peak force levels reached in the ligaments and muscles are compiled in Tables 9 and 10, respectively. As in the $-G_x$ simulations, the stretch reflex response of the muscles decreases the forces in the ligaments and dramatically raises the stress levels in the contracting muscles.

5.7 Summary and Conclusions

The results of this investigation have shown that the head-neck model developed here can very satisfactorily represent the dynamic behavior of the head and neck during frontal ($-G_x$) and lateral (G_y) impact. This is the first comprehensive head-neck model to be validated for both frontal and lateral impact situations by comparison with experimental results. Lateral impact is

TABLE 7

Peak Bending Moments in Beam Elements
 During +G_y Impact Acceleration
 (All values x 10⁶ dyne-cm)

Level	Simulation Run With Passive Muscles			Simulation Run With Stretch Reflex Response		
	Peak Moments			Peak Moments		
	M _x	M _y	M _z	M _x	M _y	M _z
T1-C7	-180	-99	-12	-155	-65	11
C6-C5	-149	-107	31	-84	20	-7
C3-C2	96	72	20	56	33	8

TABLE 8

Peak Forces in Facet Elements
 During +G_y Impact Acceleration
 (All values x 10⁶ dynes)

Facet	Simulation Run With Passive Muscles		Simulation Run With Stretch Reflex Response	
	Normal Force*	Shear Force	Normal Force*	Shear Force
T1-C7 Right	-40	184	-85	202
T1-C7 Left	16	4	17	3
C2-C1 Right	-53	64	-94	58
C2-C1 Left	34	30	-39	23

* Force normal to the plane of the articular facet joint.

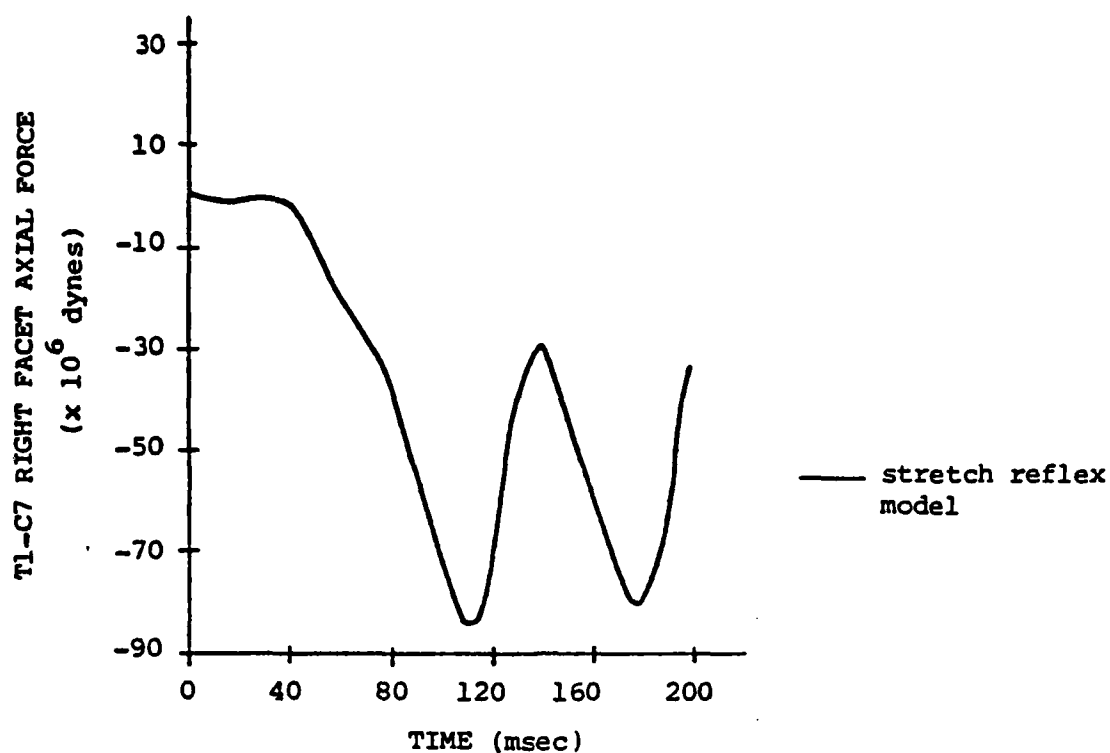


Figure 64. Time history of the axial force in the right T1-C7 articular facets during +G_y impact acceleration.

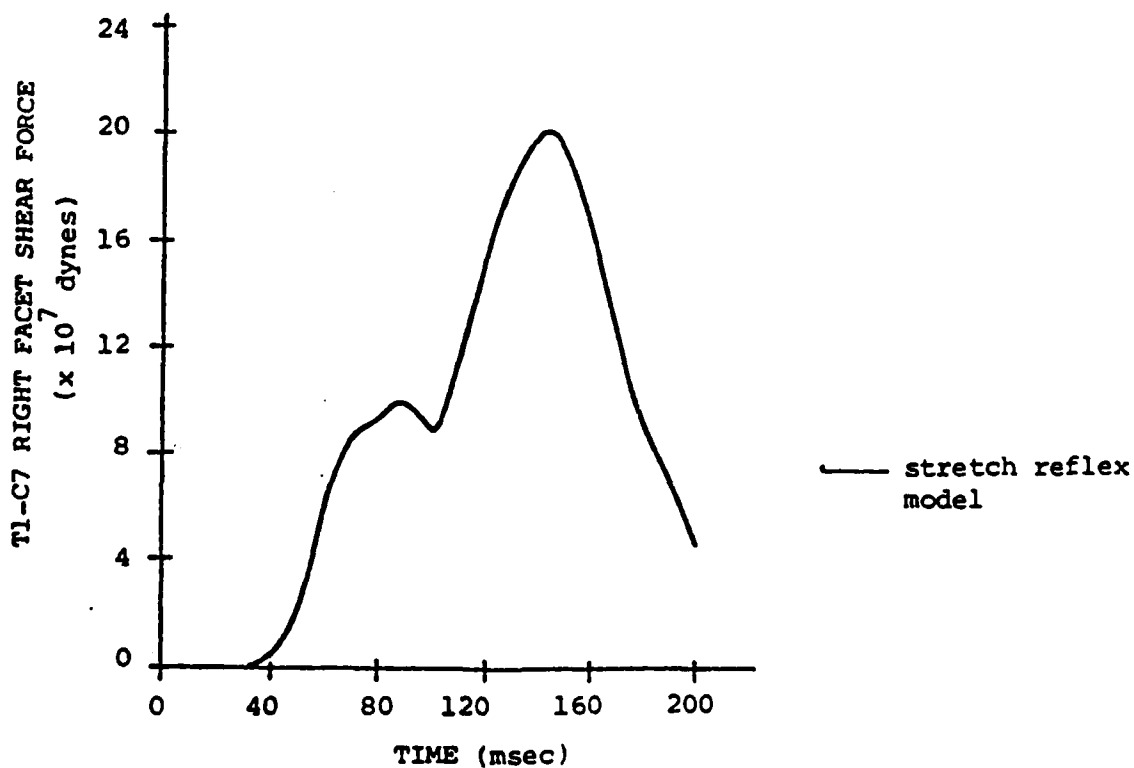


Figure 65. Time history of the shear force in the right T1-C7 articular facets during +G_y impact acceleration.

TABLE 9

Peak Force Levels in Neck Ligaments
 During +G_y Impact Acceleration
 (All values x 10⁶ dynes)

Ligament	Simulation Run With Passive Muscles	Simulation Run With Stretch Reflex Response
	Force	Force
T1-C7 interspinous ligament	8.9	1.5
C2-C1 interspinous ligament	7.4	0.04
C1-H interspinous ligament	1.5	0.03
T1-C7 posterior longitudinal ligament	0.8	0.7
C5-C4 posterior longitudinal ligament	1.1	0.5
C2-C1 posterior longitudinal ligament	1.7	0.7
Posterior atlanto-occipital ligament	3.1	1.8
T1-C7 ligamentum flavum	3.8	3.4
C6-C5 ligamentum flavum	5.2	2.5
Left T1-C7 intertransverse ligament	76	16
Left C6-C5 intertransverse ligament	37	7
Left C2-C1 intertransverse ligament	10	0.1

TABLE 10

Peak Stress Levels in Neck Muscles
 During +G_y Impact Acceleration
 (All values x 10⁶ dynes/cm²)

Left Muscles*	Simulation Run With Passive Muscles	Simulation Run With Stretch Reflex Response
	Stress	Stress
L. rectus capitis posterior major	0.73	0.23
Spinalis cervicis	1.07	0.19
L. semispinalis cervicis	0.70	0.26
L. multifidus (C6-C5)	0.02	3.91
Interspinalis (C5-C4)	1.14	0.47
L. splenius capitis	1.22	4.71
L. splenius cervicis	1.15	5.28
L. longissimus cervicis	1.10	0.56
L. longissimus capitis	0.79	4.23
L. Levator scapulae	1.03	5.22
L. trapezius	0.80	4.34
L. longus capitis	0.62	0.47
L. intertransversarius (C7-C6)	0.0002	3.67
L. intertransversarius (C3-C2)	0.64	4.06
L. sternocleidomastoideus	0.51	4.32
L. scalenus	0.65	5.00

* With the exception of the spinalis cervicis and interspinalis muscles which run down the middle of the back and neck.

a severe validation test for any neck model because of the three-dimensional motion involved. The agreement obtained with the $+G_y$ tests is, therefore, particularly satisfying. Completely three-dimensional validation of this model would require evaluation of $+G_x$ and $+G_z$ impact tests. To be of further use in analyzing the pilot ejection problem, provision must also be made to model the impact of the chin onto the chest, which occurs during this event.

The head-neck model was combined with a simplified representation of the lower spine and torso, to model whole-body impact in which the response of the head and neck is of primary concern. It was shown that fixing the head-neck model to a rigid base at the level of T1 produces a substantially different force distribution in the neck than when the lower spine is also modeled. When the lower spine is combined with the head-neck model, adequate representation of the restraint system, including the seatback, shoulder harness and lapbelt, is essential. A three-parameter viscoelastic muscle element was developed which permits modeling of voluntary muscular contraction as well as the stretch reflex response. Adequate modeling of the line of action of the neck muscles was found to be important and this was accomplished by employing up to ten intermediate sliding nodes per muscle element.

For the first time results are presented using detailed modeling of the neck musculature to show the effects of the stretch reflex response on the dynamics of the head and neck under high $-G$ impact loading. The results of $-G_x$ and $+G_y$ impact simulations imply that the response of the living subject, involving muscular reflex, is significantly different from the response of a cadaver subject, even at high impact accelerations.

It is predicted that during $-G_x$ impact the maximum axial forces in the intervertebral discs are compressive forces. Muscular contraction, brought on by the reflex response, increases the peak compressive and shear forces in the

discs, but apparently decreases the bending moments acting on the discs. On the other hand, during $+G_y$ impact the maximum axial forces in the discs are tensile. Muscular contraction, in this case, lowers both the axial and shear forces in the discs, and increases the forces acting normal to the plane of the facets on the flexion side of the neck. In both $-G_x$ and $+G_y$ simulations a reversal of the sign of the disc shear forces and bending moments occurs between levels C6-C5 and C5-C4.

Muscular contraction significantly lowers the forces in the ligaments while raising the stresses developed in the contracting muscles. It is predicted that in high-G impact tests with cadavers, the ligaments are most likely to fail before the muscles; in living subjects the contracting muscles seem more likely to be injured first.

REFERENCES

- Ashwell D.G. and R.H. Gallagher (1976), "Finite Elements for Thin Shells and Curved Members, John Wiley & Sons, Inc., London.
- Basmajian, J. V. (1967), Muscles Alive-Their Functions Revealed by Electromyography Second Edition. The Williams and Wilkins Company. Baltimore.
- Belytschko, T., L. Schwer and A.B. Schultz (1976), "A Model for Analytic Investigation of Three-Dimensional Head-Spine Dynamics," AMRL-TR-76-10 (ADA-02511), Aerospace Medical Research Laboratory, Wright Patterson Air Force Base, Ohio.
- Braakman, R. and L. Penning, (1968) "The Hyperflexion Sprain of the Cervical Spine," Radiol. Clin. Biol., 37, 309-320.
- Braakman, R. and L. Penning (1971), Injuries of the Cervical Spine, Excerpta Medica, 53-62, Amsterdam, The Netherlands.
- Bruce, E.N. (1979), "Reflex Changes in Diaphragmatic Excitation Elicited by Displacement of the Diaphragm". Am. Rev. of Respir. Dis. 119 (2 Pt 2), 61-63.
- Campbell, E.J.M., Agostoni, E. and Newsom-Davis J. (1970), The Respiratory Muscles: Mechanics and Neural Control, W. B. Saunders Co., Philadelphia and London.
- Close, R. (1972), "Dynamic Properties of Mammalian Skeletal Muscle", Physiol. Rev., 52, 139.
- Cook R.D. (1974), "Concepts and Applications of Finite Element Analysis," John Wiley & Sons, Inc., New York.
- Corda, M., C. von Euler, and G. Lennerstrang (1963), "Propriocept, Innervation of the Diaphragm". J. Physiol. (London) 178, 161.
- Crooks, L.M. (1970), "Long Term Effects of Ejecting from Aircraft," Aerospace Medicine, 41, 803-804.
- Derenne, J. P., P.T. Macklem, and C. Roussos (1978a), "The Respiratory Muscles: Mechanics, Control and Pathophysiology. Part I," Am. Review of Resp. Dis. 188, 119-33.
- Derenne, J. P., P.T. Macklem, and C. Roussos (1978), "The Respiratory Muscles: Mechanics, Control and Pathophysiology. Part II," Am. Review of Respir. Dis 118, 373-390.
- De Troyer, A., M. Sampson, S. Sigrist, and P.T. Macklem (1981), "The Diaphragm: Two Muscles," Science, 213, 237-238.

- Edwards, R.H.T. (1979) "The Diaphragm as a Muscle. Mechanisms Underlying Fatigue," Am. Rev. of Respir. Dis., 119, (2 Pt 2); 81-84.
- Evans, F.G. (1970), "Mechanical Properties and Histological Structure of Human Cortical Bone," ASME Publication 70-WA/BHF-7.
- Evans, F.G. (1975), "Stresses and Strains in Bones," Thomas, Springfield, Illinois.
- Ewing, C.L. and D.J. Thomas (1972), Human Head and Neck Response to Impact Acceleration, Naval Aerospace Medical Research Laboratory, Pensacola, Florida, (NAMRL Monograph 21).
- Ewing, C.L., D.J. Thomas, L. Lustik, W.H. Muzzy III, G.C. Willems, and P. Majewski (1977), "Dynamic Response of the Human Head and Neck to +G_y Impact Acceleration," Proc. 21st Stapp Car Crash Conf., 549-586, SAE Paper No. 770928.
- Ewing C.L., D.J. Thomas, L. Lustik, G.C. Willems, W.H. Muzzy III, E.B. Becker and M.E. Jessop (1978), "Dynamic Response of Human and Primate head and Neck to +G_y impact acceleration," Naval Aerospace Medical Research Laboratory, Pensacola, Fla. (DOT HS-803-058).
- Faulkner, J.A., L.C. Maxwell, G.L. Ruff, G.L. and T.P. White (1979), "The Diaphragm as a Muscle. Contractile properties," Am. Review of Respir. Dis., 119, (2 Pt 2) 89-92.
- Fick, R. (1910), Handbuch der Anatomie und Mechanik der Gelenke, Chapter 17. Jena, G. Fischer, Germany.
- Fielding, J.W., G.V.B. Cochran, J.F. Lansing and M. Hohl (1974), "Tears of the Transverse Ligament of the Atlas," a clinical biomechanical study. J. Bone Joint Surg., 56A, 1683.
- Fryer, D.I. (1961), "Operational Experience with British Ejection Seats," FP.R.C., 1166.
- Garamvolgyi, N. (1971), "Structural Basis of Mechanical Properties," in Contractile Proteins and Muscle, Koloman Lalci, ed., Marcel Dekker, 60, New York.
- Gates, F., D. MacCammond, W. Zingg, and H. Kunov (1980), "In Vivo Stiffness Properties of the Canine Diaphragm Muscle," Med. & Biol. Eng. & Comput., 18, 625-632.
- Glebovski, V. (1961), "Contractile Properties of Respiratory Muscles in Fully Grown Neonate Animals," Sechenov. Physiol., J. U.S.S.R., 47, 470-480, Quoted in Gates et al., 1980
- Goldman, M.D. and J. Mead (1973), "Mechanical Interaction Between the Diaphragm and the Rib Cage," J. Appl. Physiol., 35, 197, 1973.

- Goldman, M.D., A. Grassino, J. Mead and T.A. Sears (1978), "Mechanics of the Human Diaphragm During Voluntary Contraction: Dynamics," J. Appl. Physiol., 44 (6), 840-848.
- Grassino, A., M.D. Goldman, J. Mead, and T.A. Sears (1978), "Mechanics of the Human Diaphragm During Voluntary Contraction: Statics," J. Appl. Physiol., 44 (6), 829-839.
- Haxton, H.A. (1944), "Absolute Muscle Force in Ankle Flexors of Man," J. Physiol., 103, 267.
- Henzel, J.H., G.C. Mohr and H.E. Von Gierke (1968), "Reappraisal of biodynamic Implications of Human Ejections," Aerospace Medicine, 39, 231-240.
- Hill, A.V. (1970), First and Last Experiments in Muscle Mechanics, Cambridge University Press, Cambridge.
- Hirsch, C. and A. Nachemson (1961), "Clinical Observations on the Spine in Ejected Pilots," Acta Orthop. Scan., 31, 135-145.
- Jones, W.L., W.F. Madden and G. Leudeman (1964), "Ejection Seat Accelerations and Injuries," Aerospace Medicine, 35, 559.
- Jung-Cailliot, M.C. and B. Duron (1978), "Number of Neuromuscular Spindles and Electrical Activity of the Respiratory Muscles," in: Respiratory Centers and Afferent Systems, B. Duron, ed. INSERM, 165, Paris, 1976, Quoted in Derenne et al..
- Katake, K. (1961), "Studies on the Strength of Human Skeletal Muscles," J. Kyoto Pref. Med. Univ., 69, 463-483.
- Kazarian, L.E. (1975), "Standardization and Interpretation of Spinal Injury Criteria and Human Impact Acceleration Tolerance," in Aircraft Crashworthiness (Edited by K. Saczalski, G.T. Singley III, W.D. Pikley and R.L. Huston). University of Virginia, Charlottesville, VA.
- Kazarian, L.E. and G.A. Graves (1977), "Compressive Strength Characteristics of the Human Vertebral Centrum," Spine, 2, 1-14.
- Kim, M.J., W.S. Druz, J. Danon, W. Machnach and T.T. Sharp (1976), "Mechanics of the Canine Diaphragm," J. Appl Physiol., 41(3), 369-382.
- King, A.I. and A.P. Vulcan (1971), "Elastic Deformation Characteristics of the Spine," J. Biomechanics, 4, 413-429.
- Kulak, R.F. (1974), "A Study of Intervertebral Discs by Finite Element Method," Ph.D. Thesis, University of Illinois at Chicago Circle.
- Libet, B., B. Feinstein and E.W. Wright Jr. (1959), "Tendon Afferents in Autogenetic Inhibition in man". Electroencephalogram Clin. Neurophysiol., 11, 129, 1959. Quoted in Derenne et al., 1978.

- Macklem, P.T., D. Gross, A. Grassino and C. Roussos(1978), "Partitioning of the Inspiratory Pressure Swings Between Diaphragm and Intercostal/ Accessing Muscles". J. Appl. Physiol., 44, 200.
- Markolf, K.L. (1972), "Deformation of the Thoracolumbar Intervertebral Joints in Response to External Loads," J. Bone Joint Surg., 54A, 511-533.
- Mertz, H.J. and L.M. Patrick (1971), "Strength and Response of the Human Neck," Proc. 15th Stapp Car Crash Conf., SAE Paper No. 710855, 207-255.
- Messerer, O. (1880), "Über Elastizität und Festigkeit der menschlichen Knochen," J.G. Cottaschen Buchhandlung, Stuttgart.
- Mohan, D. and J. Melvin (1980), Trans. Eleventh Int. Conf. Med. Biol. Eng., 44-45, 1976, Quoted in Gates et al..
- Morris, C.B. (1948), "The Measurement of the Strength of Muscle Relative to the Cross-Section," Res. Quart. Am. Assn. Health, Phys. Ed. & Recrn., 19, 295-303.
- Nachemson, A.L. and J.H. Evans (1967), "Some Mechanical Properties of the Third Human Lumbar Interlaminar Ligament (Ligamentum Flavum) J. Biomechanics, 1, 211-220.
- Perey, A. (1957), "Fracture of the Vertebral End-Plate in the Lumbar Spine," Acata Orthop. Scad., Suppl. 25.
- Petit, J.M., J. Milic-Emil and L. Delhez (1960), "Role of the Diaphragm in Breathing in Conscious Normal Man: An Electromyographic Study," J. Appl. Physiol., 15, 1101.
- Plesha, M. and T. Belytschko (1980), "Analysis of Vertebral Stress Distributions and Ejection-Related Injury Mechanisms," AFAMRL-TR-80-67, Aerospace Medical Research Laboratory, Wright-Patterson Air Force Base, Ohio.
- Prasad, P. and A.I. King (1974), "An Experimentally Validated Dynamic Model of the Spine," Trans. ASME, J. Applied Mech., 546-550.
- Pugh, J.W., R.M. Rose and E.L. Radin (1973), "Elastic and Visco-elastic Properties of Trabecular Bone Dependence on Structure," J. Biomechanics, 6, 475-485.
- Ralston, H.J., V.T. Inman, L.A. Strait, and M.D. Shaffroth (1947), "Mechanics of Human Isolated Muscle," Am. J. Physiol., 151, 612.
- Ralston, H.J. and M.J. Polissar (1949), "Dynamic Features of Human Isolated Voluntary Muscle in Isometric and Free Contractions," J. Appl. Physiol., 1, 526.
- Ritchie, J.M. (1954), "The Relation Between Force and Velocity of Shortening in Rat Muscle," Physiol., 123, 633-639.

- Roaf, R. (1960), "A Study of the Mechanics of Spinal Injuries," J. Bone Joint Surg., 42B, 810-823.
- Rockoff, S., E. Sweet and J. Bluestein (1969), "The Relative Contributions of Trabecular and Cortical Bone to the Strength of Human Lumbar Vertebrae," Calc. Tissue Res., 3, 63-175.
- Rolander, S.D. and W.E. Blair (1975), "Deformation and Fracture of the Lumbar Vertebral End Plate," Orthopaedic Clinics of North America, 6, 75-81.
- Rotondo, G. (1975), "Spinal Injury After Ejection in Jet Pilots: Mechanism, Diagnosis, Follow-up and Prevention," Aviat. Space Environ. Med., 46, 842-848.
- Sant'Ambrogio, G. and F. Siabene (1970), "Contractile Properties of the Diaphragm in Some Mammals," Resp. Physiol., 10, 349-357.
- Sonoda, T. (1962), "Studies on the Strength for Compression, Tension and Torsion of the Human Vertebral Column," J. Kyoto Pref. Med. Univ., 71, 659-702.
- Swanson, S.A.V. and M.A.R. Freeman (1966), "Is Bone Hydraulically Strengthened?" Med. Biol. Eng., 4, 433-438.
- Tkaczuk, H. (1968), "Tensile Properties of Human Lumbar Longitudinal Ligaments," Acta Orthop. Scand., Suppl. No. 115.
- Vachon, B.R., H. Kunov and W. Zingg (1975), "Mechanical Properties of Diaphragm Muscle in Dogs," Med. Biol. Eng., 13(2), 252-60.
- Warwick, R. and P.L. Williams (1973), (Ed). Grays Anatomy 35th British Edition Saunders, Philadelphia.
- Williams, J.L. (1981), "A Three Dimensional Head-Neck Model for Impact Acceleration Studies," Ph.D. Dissertation, Northwestern University.
- Williams, J.L. and T. Belytschko (1983), "A Three-Dimensional Model of the Human Cervical Spine for Impact Simulation," J. of Biomechanical Engineering, ASME, 105, 321-332.
- Yokoo, S. (1952), "Compressive Test of the Cancellous Bone," J. Kyoto Pref. Med. Univ., 51, 273-276.
- O.C. Zienkiewicz (1977), The Finite Element Method, McGraw-Hill Book Company, London.

END

FILMED

1-86

DTIC